Viscoelasticity of a Single Folded Protein

A thesis

submitted in partial fulfillment of the requirement

of the degree of

Doctorate of Philosophy

by

Surya Pratap S. Deopa
20152043

IISER PUNE
Department of Physics
Indian Institute of Science Education & Research
Pune - 411008

DEDICATION

To my parents

CERTIFICATE

Certified that the work incorporated in the thesis entitled 'Viscoelasticity of a Single Folded Protein' submitted by Surya Pratap S. Deopa was carried out by the candidate, under my supervision. The work presented here or any part of it has not been included in any other thesis submitted previously for the award of any degree or diploma from any other University or institution.

22/03/2022
Date:

Supervisor

DECLARATION

I declare that this written submission represents my ideas in my own words and where others' ideas have been included, I have adequately cited and referenced the original sources. I also declare that I have adhered to all principles of academic honesty and integrity and have not misrepresented or fabricated or falsified any idea/data/fact/source in my submission. I understand that violation of the above will be cause for disciplinary action by the Institute and can also evoke penal action from the sources which have thus not been properly cited or from whom proper permission has not been taken when needed.

Deopa

Date: 21-03-2023

Surya Pratap S. Deopa
Roll No. 20152043

ACKNOWLEDGEMENT

I would like to thank my supervisor Dr. Shivaprasad Patil for his support and guidance over the years. Under him I was able to develop scientific way of thinking and problem solving. His method of mentoring encouraged open discussions and taught me to think critically over my PhD years in the lab.

I am also grateful to my RAC members, Dr. Vijayakumar Chikkadi and Dr. Arijit Bhattacharyay for their valuable inputs throughout my research journey. I would also like extend my gratitude towards Dr. Apratim Chatterji for helping me with the computational physics. I would also like to thank Dr. Bijay Aggarwalla for helping me with theoretical concepts involved in my research.

I would like to thank my lab members past and present for maintaining an environment conducive for fruitful scientific discussions. I am thankful to Amandeep, Shatruhan, Ajith, Vikhyaat, Jyoti, Viplove, Saurabh and Aadarsh for support and friendship during my PhD. The present members including Suyambhu, Hari, Hrishikesh, Vishal, Sujal, Asif, Shrikrishna, Mayank and Asif have made my life in the lab both fun and productive.

I would like to thank all my friends from school and college for continual support and encouragement especially Bappi, Datti, Randhawa, Negi, Pappu, Dabba and Rajat. I am grateful to Shruti, Deepak, Saptashwa and Devanshu for being supportive and fun friends over the years. I would like extend gratitude for the encouragement from Dr. Soham Pal he delivered every time I called. I am thankful to Meenakshi for the support and advise she offered to help me get through the

highs and lows of PhD life.

I am grateful to my parents for their care and support over these last few years during my PhD journey.

ABSTRACT

The nanomechanical response of a protein, the natural nanomachine responsible for myriad biological processes, provides insight into its function. The conformational flexibility of a folded state, characterised by its viscoelasticity, allows proteins to adopt different conformations to perform their function.

We present a direct and simultaneous measurement of the stiffness and internal friction of the Ig27 domain from the giant muscle protein titin using an interferometer based Atomic Force Microscope (AFM). Despite efforts and technological advances in AFM, since its discovery in 1986, accurate viscoelastic measurements on proteins were not possible. Apart from the probe being $\sim 10^4$ times larger than the protein, its own hydrodynamics can cause friction measurements to be riddled with artifacts.

To circumvent these issues we performed the experiments at off-resonance regime of the cantilever's frequency response. This places stringent constraints on the type of cantilevers that can be used. To perform true off-resonance dynamic atomic force microscopy experiments it becomes necessary to use cantilevers with high stiffness and resonance frequency. This reduces their force sensitivity, ie, the bending in the cantilever due to force. To overcome this challenge interferometer based detection system was implemented to measure the cantilever displacement directly.

Since the force spectroscopy experiments are done with octamers and linkers in-between them, to extract the viscoelasticity of a folded protein, modelling of the cantilever-protein system was done. The proposed model was validated with

the experimental measurements for the different cases one encounters during the experiment. After which, the model was used to extract the viscoelasticity of the folded domains using the new analysis method. We observe that above 95 pN of force, the protein Ig27 transitions from an elastic solid-like native state to a soft viscoelastic intermediate.

Finally, we will discussing a two state model that we are currently developing, for explaining the phase lag observed in the response of the protein in terms of the intrinsic rates and energy landscape parameters. This will help us gain insight into the microscopic origin of viscoelasticity observed in our experiments.

LIST OF FIGURES

1.1 a) Structure of an amino acid. b) Structure of Ig27 protein. It is an all beta sheet protein, which are depicted by the arrows. c) The protein Ubiquitin which has both beta sheets and a alpha helix. The alpha helix is highlighted in blue 29

1.2 Sketch of one dimensional energy landscape showing a barrier at x_1 and a minima at x_0. k_{esc} represents the rate of escape of a particle from the stable state at x_0 31

1.3 Schematic showing effect of force on the energy landscape of protein. The dotted lines represent the energy profile when no force is applied to it. The grey line depicts the tilting of the landscape due to the application of force on the protein. The barrier height ΔG_{ts} with respect to the minima reduces by Fx_{ts}. k_0 and $k(F)$ represent the unfolding rates at zero force and F force respectively 35

1.4 Various models for describing viscoelastic nature of materials 44

1.5 a) Figure showing stress and strain in context of material of length L and cross section A. b) Rheological model for a material described by Kelvin Voigt viscoelasticity. c) Response of a material with Kelvin Voigt viscoelasticity. The strain slowly reaches a steady state strain in response to a step stress d) Response of a viscoelastic material to periodic loading. The strain lag behind the stress. 48

1.6 Conventional dynamic AFM scheme. a) The cantilever with a magnetic coating is driven from the tip using a magnetic field. b) The cantilever is driven from the base using a dither piezo 49

2.1 Schematic showing the optical beam deflection technique. 67

2.2 a) Dimensions of the cantilever l = $150\mu m$, b = $25\mu m$, t = $1\mu m$ and h = $15\mu m$. b) z is the deflection in the cantilever. d is the separation of the tip from the surface. w(x,t) is the displacement of the cantilever at x position along its length and time t 68

2.3 Graph showing calibration procedure. The redline depicts the voltage at the photodiode due to the cantilever deflection. After the contact region, it is seen that the vertical deflection signal changes linearly. A stright line (blue) is fit to obtain the sensitivity 69

2.4 Graph showing the average power spectrum density (blue) of the fluctions of the cantilever. The orange curve represent the point mass model being fit to the PSD to obtain stiffness, quality factor and resonance 70

2.5 Plots of the solution of the damped harmonic model (Point mass model). a) Cantilever with low resonance and quality factor b) Same as a) apart from an added interaction stiffness to the cantilever stiffness. c) Response of a cantilever with high resonance and quality factor. d) Same as c) apart from an interaction stiffness being added to the cantilever stiffness. 80

2.6 a) Parallel arrangement for the tip excited case where an oscillating force is applied on the magnetic tip of the cantilever via an alternating magnetic field. The bending in the cantilever and protein is the same. b) Series arrangement for the base excited case, where the base is excited with an A_0 amplitude. The extension in the protein and the bending in the cantilever is inversely proportional to their respective stiffness whereas the force is same. 82

2.7 a) and c) The difference in tip displacement signal (A) and the cantilever bending signal($A_0 - A$). Interferometer based detection measures tip displacements whereas the deflection detection scheme measures the bending. For stiff cantilevers(0.5 to 1 N/m), the bending is extremely small and difficult to detect. Furthermore, A also represents the amplitude of extension in the molecule over the oscillation, which is directly measured by the interferometer. 84

3.1 The experimental setup used in the experiments. It includes a nanopositioner that is used to align the fibre at the back of the cantilever. The interferometer setup used to split the laser beam one going to a reference diode and the other to the fibre. The lockin amplifier is used to extract the amplitude A and the phase lag θ. The separation between the cantilever tip and substrate is controlled using the computer. A feedback is implemented on the amplitude of cantilever to control the z separation while approach 89

3.2 Schematic showing the signal chain followed in a lockin amplifier. The mixers multiply the input signals with reference and 90^o shifted reference signal. LPFs are low pass filters, which usually have adjustable roll off frequencies. 90

3.3 The fibre that needs to be aligned at the back of the cantilever. This photo shows the cleaved end of the fibre coated with $Ti0_2$, that is visible in its reflection on the gold coated surface. 93

3.4 The left image showing the fibre aligned at the back of the cantilever. The width of the cantilever is 35 μm and the length is 130 μm. The right image shows the nano positioner being utilised to perform the alignment. The arrows in white depict the axis of motion and rotation, for the two plates on which the fibre is attached 94

3.5 a) The stack of piezos on which a sliding plate is kep. For moving the plate in a translational way, piezo having their shear axis along the desired direction are activated with the correct polarity. For rotational motion, the top plate and the bottom two stacks are moved in the opposite direction. For example to make a plate rotate clockwise, the outermost piezo of the top stack with shear axis to the right will be activated and the top piezo of the bottom two stacks will be biased with the reverse polarity as compared to the top piezo. b) Front view of the nanopositioner. c) Side view of the nanopositioner. 95

3.6 a) Figure showing multiple reflections between a gold coated surface and the $Ti0_2$ coated cleaved end of the fibre. The fibre is parallel to the gold surface which is required for a Fabry Perot Etalon. b) The separation between the two mirrors modulated using the tube piezo. c) The red line signifying the power incident on the photodiode a function of separation between the two mirrors. The blue line is the same pattern, but in the reverse cycle of triangular wave given to the fibre piezo. The intensity in the forward and reverse cycles do not fall on each other due to some hysteris in the movement of the tube piezo. The third line is a cos function of the separation between the two mirror, which can be used as reference for comparing the interference pattern. The square marker on the graph shows the separation of maximum sensitivity on the graph, on which the piezo has to be locked during the experiment. 97

3.7 a) The lower piece of the fluid cell. Its bottom surface has the a metal disc glued to it, which is used for attaching the cell to the magnets on the sample stage. Also contains four holes for the screws to be inserted. b) The top pieces of the sample, also containing holes for the screws to be inserted. c) Rubber O-ring that gets sandwiched between the the pieces of the sample cell. d) Fluid cell after assembly with a gold coated cover coated loaded onto it. 98

3.8 Figure depicting the sample stage, containing the hammer and the scanner piezo 99

3.9 Figure depicting an experiment where the cantilever is fishing for the proteins. The proteins here are sparsely present on the surface. After each approach-retract cycle, the position of the substrate is changed to pick up new protein to unfold with the cantilever. 100

3.10 Figure showing variation of tip amplitude as the cantilever is retracted away from the surface with the protein attached it. The cantilever stiffness for this experiment is 0.8N/m (800pN/nm) and the sensitivity is 300nm/mV 103

4.1 Schematic of the sacromere, depicting titin tethered to the thick filament (myosin) and the Z-Line. 105

4.2 The octomer of I-27 under force. The cartoon shows a situation, wherein one domain is unfolded and the remaining seven are in the folded state. When the folded domains are pulled by increasing z, the force is applied to domains through wlc chain of first unfolded domain. When the force exceeds $\approx$ 95 pN (shaded region in figure 4.2), the domains in the native state (left) are pushed into mechanical intermediate(right). As shown in the β-sheet schematic, the hydrogen bond network between B-A and A'-G is responsible for the mechanical stability of the native state, of which the network between A and B is broken for the intermediate, elongating the protein by $n \times \Delta L$, where $\Delta L = 0.66$ nm. 109

4.3 The measured combined stiffness (blue continuous) and friction coefficient (red continuous) of unfolded chain and the folded domains of Ig27 octamer as the domains sequentially unfold. The amplitude and phase of the tip displacement is used for the calculation. The data shows a sawtooth pattern of unfolding events similar to constant velocity pulling experiments. The green continuous line is a fit to the wlc model. The mean difference in contour length between two consecutive peaks is 29 ± 0.8 nm. A persistence length of 0.4 nm is used. The first four events deviate from wlc in the shaded region where folded domains are comparable in stiffness to the unfolded chain and contribute to the measurement. The dissipation is seen in the corresponding region due to the internal friction in folded domains. The data in the dark shaded region is used for further analysis to obtain the stiffness and internal friction coefficient of the folded state. Cantilever stiffness is 0.6 N/m, The cantilever base is excited with frequency 2.1 kHz and amplitude 1 nm. The plot is representative of more than 50 traces recorded at different frequencies and amplitudes. 110

4.4 a) Cartoon showing seven domains in the native state and one unfolded domain. When all the folded proteins are in the native state, the total stiffness measured fits the WLC model. The folded domains are in series with the unfolded domains, the element with the lower stiffness contributes to the total measured stiffness. b) Under forces exceeding 95pN, the protein goes into the intermediate state and the wlc model stops fitting the total stiffness data and we start measuring dissipation as well. From this we conclude that some of the folded domains have entered the intermediate, but exact number is not known. This region is depicted by the light grey shaded region in figure 4.2 . c) After the initial decrease in stiffness, the total measured stiffness starts to rise again, here all the domains have entered the intermediate state. d) After 4 unfolding events the contour length of the unfolded chain becomes larger, making it more compliant than a short chain at the same force (explanation in the next section). Due to which its stiffness becomes much lower than the intermediate state as well and the total stiffness measurement has contribution coming only from the unfolded chain. This is supported by the WLC fits to the last four unfolding domains 111

4.5 Force and stiffness variation for each contour length. With each unfolding event, the unfolded chain becomes more complaint for the same force (~ 160) pN, thereby dominating the total measured stiffness. The protein is unfolded before the chain has a comparable stiffness to the folded domains so that they start to contribute to the total stiffness measurement. Thus, last four domains unfold without contributing to the stiffness measurement and wlc fits to the entire stretching of the chain. 113

4.6 A spring-dashpot model for the protein-cantilever system. A_o and A are the base and tip amplitude respectively and θ is the phase lag between them. ω is the drive frequency. k_{wlc} and γ_z are the unfolded chain stiffness and surface damping respectively. k_f and γ_f are the stiffness and friction coefficient of the folded domain, where k_f/n and γ_f/n means n of them are in series. 114

4.7 a) The measured total friction coefficient (blue) along with a polynomial fit (red) for the damping due to the surface effects. The lower panel in a) represents friction coefficient of the protein alone, $\bar{\gamma}-\gamma_z$ b) shows that measured stiffness is zero when the protein is not attached, however the damping due to the surface is still measured (blue). . . . 117

4.8 Numerical integration of the stiffness-extension profiles to obtain force-extension profiles. Continuous green curve- wlc fits, Continuous blue curve- experimental data, continuous red curve - force obtained after integration. The green shaded region represents integration done over fitted WLC model. The blue shaded region represents integration over experimental data where it deviates from WLC behavior. . . 120

4.9 a)The plot of total friction coefficient $\bar{\gamma}$ calculated at different tip-substrate separation z using equation 10. Here the γ_z is taken to be zero. The contour length is increased by 29 nm after each event and n is reduced by one. k_f and γ_f are taken as 100 pN/nm and 2×10^{-6} kg/s. The variation in friction coefficient with respect to z is plotted for each event until 160 pN is reached. This is the average force at which domain unfolds. b) Each domain unfolds at slightly different force as the unfolding events are stochastic. We take similar values for all other parameters as in (a), however $\bar{\gamma}$ is now calculated and plotted for each event until unfolding force values are reached for that event. In both plots, it is seen that the peak in the total friction coefficient decreases as domains unfold one by one. The height of the peak also depends on the unfolding force for that event. 122

4.10 a)The integration of stiffness-extension (continuous blue line) provides force-extension plot (continuous red line). The vertical dotted line indicates deviation of stiffness-extension from the wlc model fit (continuous green lines). Its intersection with force-extension gives force at which, stiffness has a contribution from folded domains. b) Bar plots of force where transition occurs and the force required to unfold a domain completely (N: Native and I: Intermediate). The deviation kicks-in when force exceeds 95 ± 16 pN. The force required to unfold the domain completely is 161 ± 25 pN. These values match with force needed to push domains of (I-27)$_8$ into the intermediate and then unfold it completely[6]. The mean force required to unfold a domain completely, is $\sim$ 200 pN in static pulling experiments. It is $\sim$ 160 pN in our experiments due to the energy provided to it through oscillations. c) stiffness k_f and friction coefficient γ_f of a single folded domain at different forces F. The plots provide viscoelastic characterization of single folded intermediate. The data points in the same colour are from the analysis of same unfolding peak. The data is pulled together from many different profiles similar to the one shown in figure 4.2 124

5.1 Schematic showing the energy profile 134
5.2 Flowchart for the simulation algorithm 138
5.3 a),b) and c) depict the trajectories obtain for parameters discussed in the text. $_0$ and α_1 represent the asymmetry parameter and subscript represent the 0 and 1 nm driving amplitude respectively. d) e) and f) are the bar plot showing fraction of time the end to end distance of the polyprotein spends at a particular length during the simulation. 140

CONTENTS

1 Introduction **27**

1.1 Sturcture 28

1.2 Folding 30

1.3 Kramers' Rates 30

1.4 Unfolding proteins with Force 32

1.4.1 Effect of force on folded proteins 33

1.4.2 Effect of force on Unfolded Protein 33

1.5 Bell-Evans-Richie Model 34

1.6 Emerging protein unfolding models 36

1.7 Viscoelasticity of folded Proteins 38

1.7.1 Effective Stiffness from Thermal Fluctuations 39

1.7.2 Internal Friction 40

1.7.3 Atomic Force Microscope for stiffness of folded domain 41

1.7.4 Nanorheology on folded proteins 42

1.8 Rheology 43

1.8.1 Kelvin Voigt model 44

1.8.2 Maxwell model 45

1.8.3 Standard Linear Solid 45

1.8.4 Burgers Model 46

1.8.5 Generalised Maxwell and Kelvin models 46

1.8.6 Oscillatory Rheology 47

1.9 Dynamic AFM for single proteins 49
    1.9.1 Dynamic AFM measurement scheme 49
1.10 Objectives & Motivations 51

2 Cantilever Dynamics 65
2.1 Overview 65
2.2 Deflection Detection Scheme 66
2.3 Point Mass Model 66
2.4 Continuous Beam Model: 70
2.5 Excitation Schemes 73
2.6 On or Near-resonance Operation 74
2.7 Off-resonance operation 75
2.8 Alternate Continuous Beam Model. 77
    2.8.1 Artifact Free Measurements at Off-resonance 79
2.9 Series/Parallel Arrangements: 81
    2.9.1 Parallel (Tip excitation): 82
    2.9.2 Series (Base Excitation) 83
2.10 Need for Displacement Detection Scheme 84

3 Instrumentation 87
3.1 Overview 88
3.2 Phase Sensitive Detection 90
3.3 Semi Mirror 92
3.4 Nano Positioner 93
3.5 Fibre Alignment 95
3.6 Fluid Cell 98
3.7 Approach & Amplitude Feedback 98
3.8 Grid 99
3.9 Methods 100
    3.9.1 Sample Preparation 100
    3.9.2 Cantilevers 101

3.9.3 Experiment 101

4 Measurement 105

4.1 I27 as a Suitable Candidate for Measurement of Viscoelasticity 105
4.2 Total Stiffness and Friction 106
4.3 Compliance of an Unfolded Protein 112
4.4 Model 113
4.5 Data Analysis 118
 4.5.1 Analysis to obtain k_{wlc} 118
 4.5.2 Obtaining k_f & γ_f 119
4.6 Features in the Friction Profiles 121
4.7 Viscoelasticity of a single folded domain 123
4.8 Discussion 125

5 Simulations 133

5.1 Introduction 133
5.2 Two State Model 134
 5.2.1 Dynamic Monte-Carlo Simulation 137
 5.2.2 Preliminary Trajectories 139

6 Conclusion & Future Directions 143

CHAPTER

ONE

INTRODUCTION

The inner workings of living organisms have intrigued researchers from diverse fields. Processes that enable us as multi cellular organisms to function are incredibly complex. The field of biophysics that aims at explaining these phenomena with physical laws has emerged in the second half of the last century.

Zooming beyond the diffraction limit, one reaches the world of nanometers. Here, one encounters marcromolecules such as Deoxyribonucleic Acid (DNA), Ribonucleic Acid (RNA) and proteins that are the constituents over which, life is build. For instance, the remarkable way in which the chaperones help in constructing proteins from RNA, are akin to a production line churning out finished goods, but only at the nanoscale. Out of all these macromolecules, proteins are especially interesting due to the immense diversity in the functions they perform [1].

Antibodies are proteins that are produced by the immune system to fight against foreign substances - antigens. These proteins bind to antigens -bacteria, viruses, fungi, toxins- inactivating them and rendering them harmless. Immunoglobulins examples of antibodies, with a Y shaped structure, each top end having a binding site for the antigens[1].

There are a huge number of chemical reactions happening inside the body. The remarkable specificity of these reactions, aided by enzymes identifying the gene code

[1, 2].

Within a living organism, there are thousands of processes happening in unison. To co-ordinate these biological processes messenger proteins come into the picture. These are hormones that transmit signals between cells, tissues and organs. The growth hormone is one such protein that is responsible for the regulation of growth and metabolism [1].

Proteins also act as a structural component providing rigidity and stiffness to the cells. Actin is one such protein, among other tasks, it is present in the thin fibrils of the muscles and micro filaments in the cytoplasm[1, 3].

Although the insides of a cell are crowded, small molecules like glucose diffuse to their required destinations within the cell. However, larger organelle like mitochondria, have to be actively transported to their destinations. To fulfil this task motor proteins are employed. Kinesin is one such motor protein that carries cargo – from one point to another walking unidirectionally on a micro-tubule [1].

Before going into the details of mechanical properties of proteins in the context of this work, we will be discussing general topics, such as its structure, protein folding and unfolding in the following sections.

1.1 STURCTURE

Proteins are heteropolymers comprised of a large number of amino acids. These amino acids are small molecules that consist of an amine group, a carboxylic group, a hydrogen and a variable side chain connected to an alpha carbon (figure 1.1(a)). The amino acids are covalently linked to one another via the peptide bond that is formed when a hydrogen atom from the amine group and a hydroxl from the carboxylic group of the other amino acid gets released, forming a water molecule and linking the nitrogen and carbon from the two different amino acids together to form a peptide bond [4].

Once these amino acids are linked they are referred to as residues. Each residue has a unique property that is determined by its side chain. There are around 20 amino acids with a wide range of hydrophobicity, polar nature and aromacity. The arrangement of residues is known as sequence of the protein and determines its 3D structure [4]. It is also responsible for forming its primary and secondary structure. After the protein is constructed as a semiflexible chain in a particular sequence, it folds into its native conformation which is its minimum energy state.

The next level of structure present in proteins are the β-sheets, that are formed by parallel or anti parallel β-strands, α-helix, turns and coils [1]. The Nobel prize in 1951 was awarded to Linus Pauling for the his contribution to the discovery of these structures[5, 6]. Multiple α-helice, β-sheets or other secondary structures coming together to give the protein its geometric shape forms the tertiary structure. To name a few, it can be all β-sheets, α-sheets, α/β structure among many other combinations. The interaction between multiple polypeptide chains forms the quarternary structure[1].

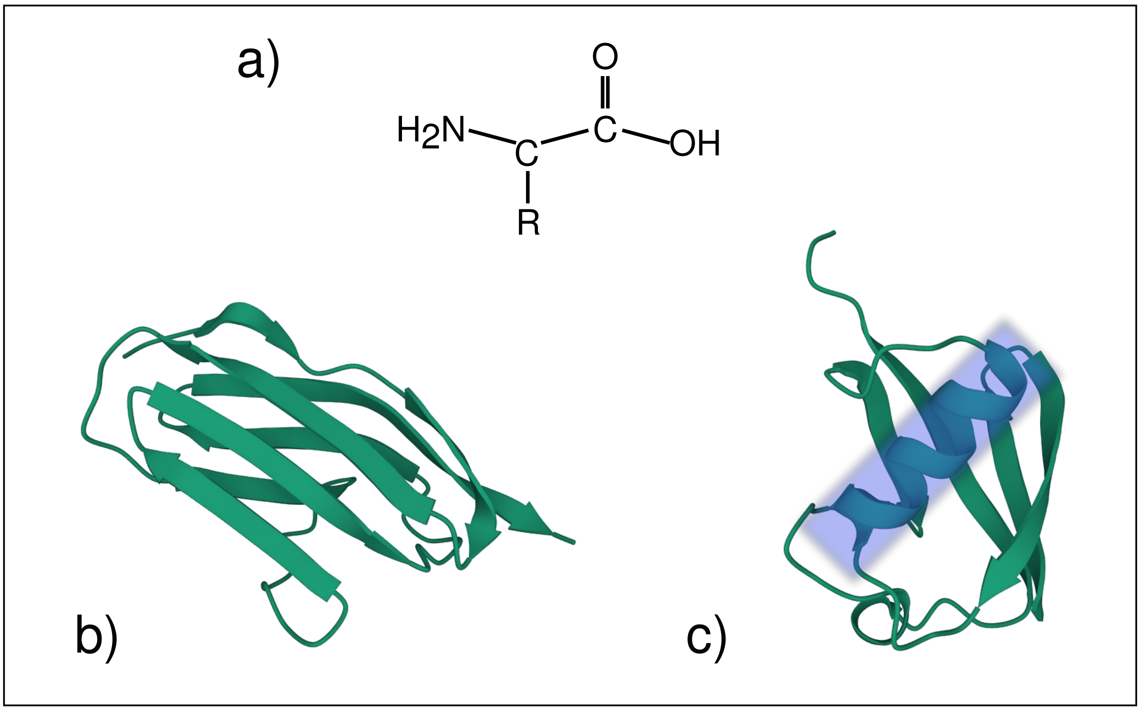

Figure 1.1: a) Structure of an amino acid. b) Structure of Ig27 protein. It is an all beta sheet protein, which are depicted by the arrows. c) The protein Ubiquitin which has both beta sheets and a alpha helix. The alpha helix is highlighted in blue

1.2 FOLDING

The protein folding problem is decades old [7] and contemporary experimental techniques [8] and increase in computational capabilities [9, 10] have led to great advancements in the field.

The folded state of a protein is the most stable state under right solvent conditions and is at the minimum of the thermodynamic Gibbs free energy G. For a change in state of a protein under constant temperature and pressure, the change in Gibbs free energy ΔG can be expressed in terms of change in enthalpy ΔH and entropy $T\Delta S$ as $\Delta G = \Delta H - T\Delta S$. The folded state is separated by a transition state TS from the unfolded state that is a barrier of higher energy between the two. The difference in free energy of the unfolded and folded state gives the free energy difference ΔG and determines the thermodynamic stability of the protein [4].

However, proteins have complex energy surfaces and fold via multiple intermediate states[11]. The energy landscape theory describes the folding of a protein down the energy funnel visiting multiple intermediates as it reaches its most stable state as opposed to random diffusion in the configuration space [12, 13]. These intermediates get populated due to the barriers in the folding pathway, giving the energy surface, ruggedness. As the protein traverses down the funnel it loses it entropy, this adds negatively to the free energy difference, however loss in entropy is compensated by the gain in enthalpy as contacts between residues are formed [14]. These are noncovalent interactions that mainly include hydrophobic interactions, hydrogen bonds, salt bridges and ion pairs [15, 16].

1.3 KRAMERS' RATES

Kramers derived the rate at which a reaction would occur if the reactants and products are separated by an energy barrier [17]. It involved solving the Fokker Planck equation in a one dimensional potential $U(x)$. The potential with a minima at $x = x_0$ and a maxima at $x = x_b$, represents reactant and transition state along the coordinate respectively (figure 1.2). The rate at which the reaction occurs, ie, the probability per unit time for the particle to escape the barrier k_{esc}, was derived in two limits - energy diffusion limit and the overdamped limit [18]. The latter limit is more relevant in the context of this thesis since, since biomolecules in the liquid environment follow over overdamped dynamics. In these conditions the escape rate is given by

$$k_{esc} = \frac{\omega_0 \omega_1}{2\pi\gamma} \exp\left(-\Delta U / k_b T\right) \tag{1.1}$$

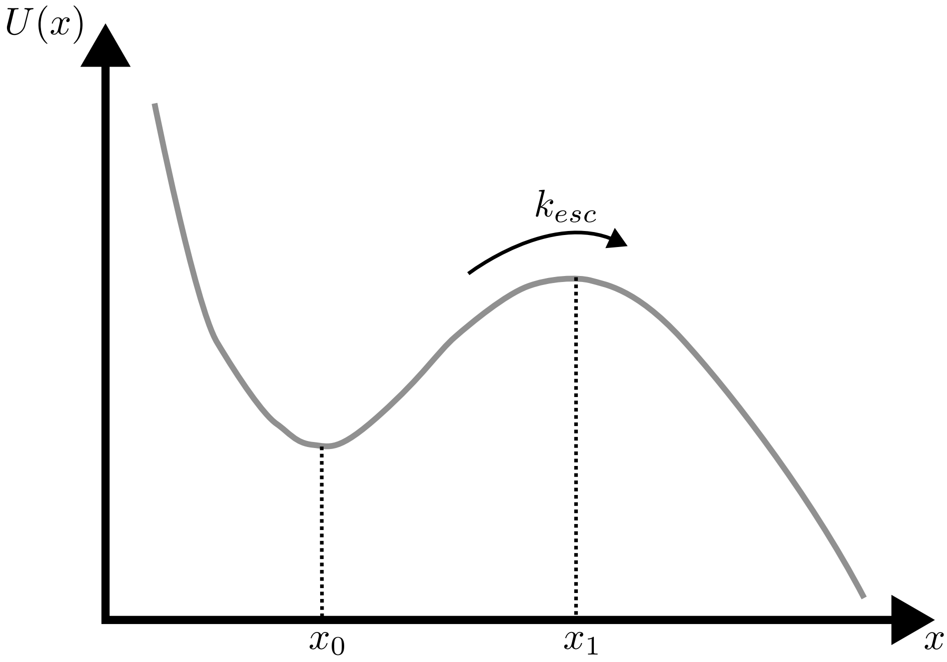

Figure 1.2: Sketch of one dimensional energy landscape showing a barrier at x_1 and a minima at x_0. k_{esc} represents the rate of escape of a particle from the stable state at x_0

Where γ is the friction coefficicent, T is the temperature, ω_1 and ω_0 are given by, $U''(x_0)/m$ and $U''(x_1)/m$ respectively, while $\Delta U = U(x_1) - U(x_0)$. Kramers rate theory when applied to protein folding, essentially treats protein undergoing conformational changes as a chemical reaction. When the folding of a protein is described in a two state manner, the energy landscape along a reaction coordinate has minima at the folded and unfolded state and a maxima at the transition state. The reaction rate in this case would give the rate at which the unfolded protein at

x_0 overcomes the barrier at x_1 to reach the folded state. Not only can the kramers' rate be used to describe the folding process, but also the unfolding when a force is applied on it. How the rate changes by applying force is discussed in the next section.

1.4 Unfolding proteins with Force

Applying forces to proteins is a difficult task, especially due to the liquid environment in which the experiments have to be performed. However, over the last few decades it has become routine to unfold proteins by applying forces[19]. There are three most widely used tools for these experiments, each having their own advantages.

The most sensitive in terms of forces are the Optical Tweezers [20], in which a bead is trapped in a harmonic potential created by a laser. A molecule is then attached to the bead, with the other end held constant or attached to another laser trapped bead. Typically, optical tweezers can apply forces as low as 2pN in a controlled manner[21–23]. The magnetic tweezer is another such tool that can apply small forces on single molecules [24, 25]. Magnetic tweezers are extremely stable, due to which one can apply small forces on proteins for hours[26–29].

Apart from the two, the Atomic Force Microscope (AFM) is another such tool capable of applying forces on single molecules. Ever since its invention in 1986 [30], it has been incorporated to experiments in diverse fields. It has been successful in imaging atoms in ultra high vacuum [31], measure atomic scale dissipative processes [32], measure conductance [33] and work functions [34] at the nanoscale and even quantify elasticity of biological cells [35] Further, it can be used to apply and measure forces on single molecules like proteins, DNA, RNA and polymers. [36–39].

The conventional force spectroscopy experiments with AFM on proteins are mainly of two types - constant velocity pulling or force clamp. Constant velocity pulling experiments are carried out by attaching a protein between the tip of the cantilever and the substrate, and retracting the base with constant velocity. The force at which the protein unfolds is recorded. This unfolding force measurement is repeated several times to get a distribution of unfolding forces, which can be used to infer properties of the protein [40]. On the other hand, in force clamp experiment constant force is applied on the protein, which is achieved by a feedback on the cantilever deflection. Here, the time taken for the protein to unfold is measured. These measurements are then used to extract the free energy landscape parameters of the folded protein[41].

1.4.1 Effect of force on folded proteins

For experiments performed with force spectroscopy tools, the reaction coordinate is always the direction of pulling. Usually the ends of the protein are attached to the substrate and the cantilever tip with the help of polymer linkers, making the end to end distance ,N-terminus to C-terminus, of the protein the reaction coordinate [42]. Proteins that have a simple two state free energy profile along the end to end distance, with a single unfolding pathway, the folded state and the unfolded state are separated by a barrier called the transition state TS. Force F when applied on such proteins, modifies their energy landscape by tilting the energy profile making it more probable for the protein to be in unfolded state[42].

1.4.2 Effect of force on Unfolded Protein

Once the protein unfolds, all the native interactions are lost, however, extending the unfolded chain reduces its entropy. This reduction in entropy is caused due to lesser number of conformations available for the unfolded protein to acquire as its end to end distance is increased. Due to this, the unfolded chain exerts force on the cantilever. The force it exerts on the cantilever for a particular end to end distance follows a nonlinear profile. One the most popular model that describes this behaviour is the Worm Like Chain model (WLC), derived by Marko-Siggia [43] and later validated by Bustamante [44]. The salient features of this model are that the polymer has a minimum length scale called persistence length after which the correlations die out. In other words the persistence length is a measure of the longest rigid component of the chain. The force extension profile is given by

$$F = \frac{k_B T}{p}\Big(\frac{1}{4(1 - x/L)^{-3}} - \frac{1}{4} + \frac{x}{Lc}\Big) \tag{1.2}$$

Where L_c is the contour length of the chain, which represents the maximum length the chain can acquire.

1.5 BELL-EVANS-RICHIE MODEL

The most widely used model to describe forced unfolding of proteins, is the Bell-Evans-Richie model[45]. Vast number of forced spectroscopy studies on proteins and bond rupture kinetics have employed this model to extract the free energy landscape parameters like distance to transition state from the energy minima as well the unfolding rate at equilibrium[46]. The model was first derived by Bell [47] to explain the cell to cell adhesion and was later modified by Evans and Richie to explain forced bond rupture kinetics. The model simply predicts that the rate of unfolding of the protein increases exponentially with force. For a protein having a free energy landscape similar to the one shown in figure 1.3, the rate of unfolding at zero force can be written as

$$k_0 = A \exp\left(-\Delta G_{ts}/k_b T\right) \tag{1.3}$$

Where the prefactor $A = (\omega_0 \omega_{ts})/(2\pi\gamma)$ contains the information about the curvature of the landscape at the minima x_0 and the transition state x_{ts} along with the damping experienced by the protein. As mentioned earlier, the force on the protein modifies the energy landscape by tilting it. The new rate of unfolding for a force F acting on the protein is given by

$$k(F) = A \exp \frac{-(\Delta G_{ts} - F x_{ts})}{k_B T} \tag{1.4}$$

$$k(F) = k_0 \exp\left(-F x_{ts}/k_b T\right) \tag{1.5}$$

In this model it is assumed that applying a force on the protein, the prefactor A in the equation 1.3 does not change considerably and therefore is assumed to

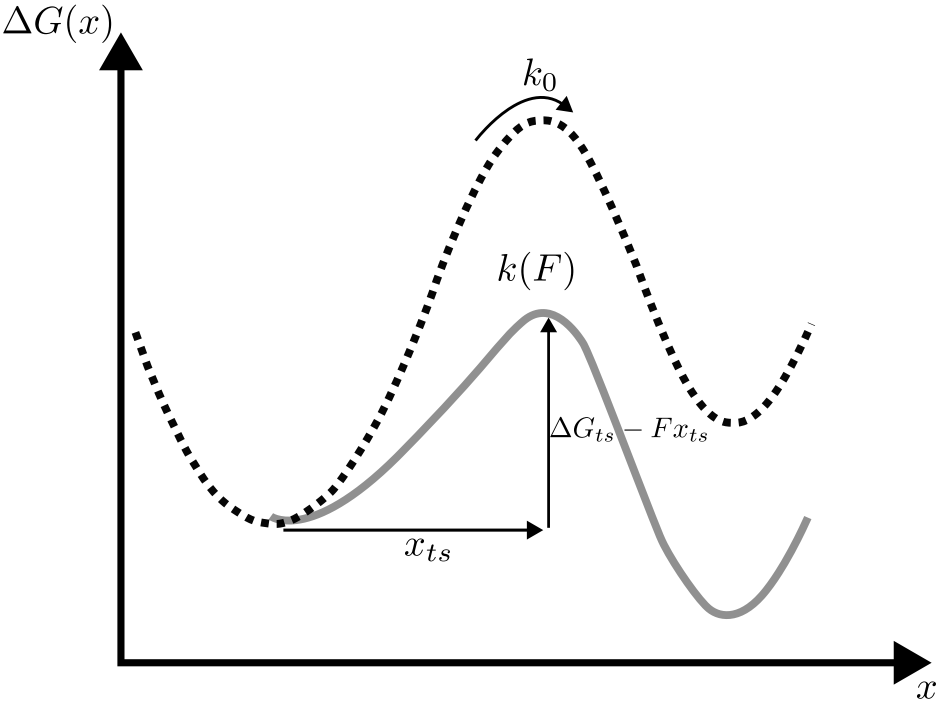

Figure 1.3: Schematic showing effect of force on the energy landscape of protein. The dotted lines represent the energy profile when no force is applied to it. The grey line depicts the tilting of the landscape due to the application of force on the protein. The barrier height ΔG_{ts} with respect to the minima reduces by Fx_{ts}. k_0 and $k(F)$ represent the unfolding rates at zero force and F force respectively

be constant. Furthermore, it is assumed that the location of the transition does not change as the force acts on the energy landscape. This is particularly justified if the landscape is sharp [45]. In constant velocity experiments the force on the protein continuously increases as the cantilever is retracted away from the substrate, therefore the loading rate on the protein is given by

$$r = \frac{dF}{dt} = k_c v \tag{1.6}$$

The unfolding force distribution is then obtained as

$$P(F_u) = \frac{k_0}{r} \exp\left(\frac{F_u x_{ts}}{k_B T}\right) \exp\left(k_0 \frac{k_B T}{r x_{ts}}\left(1 - \frac{F_u x_{ts}}{k_B T}\right)\right) \tag{1.7}$$

The most probable force of unfolding for the distribution is given by

$$F_u^* = \frac{k_B T}{x_{ts}} \ln \frac{r}{k_B T x_{ts}} \tag{1.8}$$

The slope of the linear fit to most probable force of unfolding vs logarithmic variation of loading rate gives the distance to transition state and the intercept gives the unfolding rate k_0 at zero force.

1.6 Emerging protein unfolding models

Bell-evans-richie model [45] predicts the unfolding force to logarithmically scale with the loading rate, however this is seldom the case at high loading rates [48]. Although this model has been widely used, more rigorous models have been developed with fewer approximations. The Dudko-Hummer-Szabo model [49] takes into consideration the shape of the energy landscape. An arbitrary exponent is added to the derivation that determines the shape of the energy landscape and accounts for the non linear behaviour of unfolding force with increasing loading rate. Dudko and Hummer [50] also pointed out that the loading on the protein is not directly from the cantilever but via the tether which is present in between the cantilever and the protein. Therefore, the loading rate on the protein becomes non constant and depends on the combined stiffness of the cantilever and the tether which follows a WLC behaviour. Hence, the loading rate at the time the protein unfolds depends on the extension to which the tether is pulled to. Friddle et. al. came up with a model that takes into account the refolding or rebinding rates of a protein under a threshold force[51]. However, it still discounts the refolding rates if the unfolding happens over the threshold force. The transition state movements with force are also a factor that can contribute to deviation of experiments from the Bells-evan-richie model[52].

Although these models try to explain the non logarithmic behaviour of the unfolding force with loading rate, the energy landscape of the protein is still considered to be single dimensional. The argument given here is that all the other degrees of freedom in the protein other than the end to end distance are always in thermal equilibrium during the pulling process, and therefore can be integrated out to get free energy as function of end to end distance only[53].

In the past few decades alternate approaches to the mechanism of protein unfolding via force have been building up. Some of these include the fluctuating bottleneck model which was initially derived by Zwanzig to explain reactions happening from two different basins [54]. It was then applied to single molecule force spectroscopy technique, to show that biomolecules do exhibit some level of disorder in their native state [55]. The same group, showed that heterogenity in the folded state of a protein can directly be measured by single molecule force spectropcopy[56]. The model states that the proteins exhibit multiple stable minimas around the native state and these states have different unfolding rates. Multidimensionality of the energy landscape can also be established with the unfolding rate showing downward curvature in the k_f vs f graph [57].

Zwanzig showed that the diffusion in a rugged potential gets slowed down exponentially with the level of ruggedness [58]. Changbong et. al. later applied this theory to force spectroscopy experiments and predicted that the ruggedness of the energy landscape can be measured by performing force spectroscopy experiments at different temperatures[59]. Numerous force spectroscopy experiments were done to quantify the ruggedness experimentally, with Nevo et al. performing first such experiments on Bacteriorhodopsin[60].

One big assumption of force spectroscopy experiments is that it assumes the adiabatic approximation, stating that the pulling process is quasistatic with respect to the internal dynamics of the protein, i.e., the protein is always in equilibrium with the surroundings. Bullerjahn et. al., derived relations for a range of loading rates and called it rapid force spectroscopy[61]. In another study, it was shown that for a protein to show anti-hammond behaviour, the transition state moving away from the folded state on the reaction coordinate as force is applied, cannot be possible on a single dimensional energy landscape [53].

Emphasis has been building up to probe the intrinsic dynamics of the folded state. Models are being developed to extract information about the energy landscape, other than the unfolding rates and distance to the transition state. Although successful, gaining information about the folded states' dynamics from the unfolding data is difficult and relies heavily on the model being utilised. In essence, with these models, the deviations in the usual unfolding data is accounted for by the intrinsic dynamics of the folded state. To directly measure the dynamics, one needs to measure the response of the protein without unfolding it.

1.7 VISCOELASTICITY OF FOLDED PROTEINS

Proteins are dynamic entities that play a pivotal role in biological processes responsible for life[62–64]. In order to be dynamic, proteins need to be flexible [65] [66]. For instance, Myoglobin which reversibly stores O_2, assumes two conformations. One in which O_2 is trapped and in another it is unbound. The effective force constants of these two states, as measured using neutron scattering experiments, differ[65, 67]. Bacteriodhopsin, a transmembrane protein, which uses light to produce movement of protons across cell membranes, possesses relatively more rigid core buried in the membrane and flexible extracellular and cytoplasmic loops[65, 66]. In general, the ability to change shape is an important attribute of proteins in order to deliver specific functions. Although, flexibility plays a central role in it, little is known about mechanical properties of a single folded protein.

As mentioned earlier, proteins also exhibit molecular level heterogeneity revealed by single molecule experiments[55]. It is argued that such disorder not only plays a central role in delivering function, but also allows proteins to participate in different biochemical reactions to deliver different functions by effectively tuning their shapes through a phenomenon referred to as allostery. One of the important goals of nanotechnology research is to quantify folded protein's mechanical response and establish its connection with the constituent bonds. Besides understanding protein function, this knowledge can be useful for design and fabrication of efficient nanomachines [68, 69]. Furthermore, due to the heterogeneity in the folded state, it is important that nanomechanical response is measured at the level of single proteins.

From a mechanical perspective, the stiffness provides crucial cues about the extent to which proteins can be deformed under physiological forces, but says little about the time scales of its dynamics. The thermal fluctuations of proteins, measured using neutron scattering and X-rays, suggest ruggedness of energy landscape overriding the deep minima. A direct consequence of such ruggedness is internal friction of the folded state. Hence, one needs to measure the viscoelastic response (stiffness and internal friction) of a single protein in its folded state. The stiffness and damping coefficient of viscoelastic materials determine the extent of full deformation under a given load and the time scales needed to reach it[69, 70]. This purely mechanical view is supported by biochemical experiments in which, it is shown that difference in folding rates of protein homologues of spectrin can be attributed to ruggedness and hence internal friction[71].

The ruggedness also implies that there is a considerable slow-down in the diffusive dynamics, due to the formation and breakage of native as well as non-native contacts. The rugged energy landscape also supports the idea of heterogeneity in proteins. If a folded protein is driven with extremely small perturbations over a rugged landscape formed out of many conformational substates, one is expected to observe loss of energy if the relaxations are slow. This predicts a finite internal friction for folded proteins. In the next sections we will be discussing about the attempts at characterising stiffness and friction of folded proteins.

1.7.1 Effective Stiffness from Thermal Fluctuations

Proteins need to be active in order to perform functions, this is possible due to the motion their constituent parts make between their conformational substates at physiological temperature. Fluctuations between states gives them their flexibility and are responsible for their function. Beginning with experiments by Doster, Cusack and Petry [72], which showed dynamic transition in Myoglobin, measurement of stiffness using elastic scattering has attracted many researchers [65]. Two reviews by Zaccai [65, 73], succinctly describe the achievements in this field. The quantification of molecular "softness" or rigidity is obtained by analysing localized thermal motions of proteins. The mean square displacements of this motion can be captured from the angular dependence of incoherent scattered elastic part of the intensity. The neutron scattering experiments offer a time and space widow determined by its energy resolution and scattering vector. Typically these are $\sim$ 100 ps and $\sim$ 0.1 nm. In this sense it is probing local fluctuations around a minimum of the substate the protein is in. At higher temperatures the molecule samples other conformational substates and the motion is anharmonic. From plots of mean square displacement versus temperature, it is possible to estimate an effective environmental force constant of the proteins. At room temperature, the force constant estimated by this method for Myogoblin is 0.3 N/m. In case of bacteriorhodopsin, neutron scattering reveals the subtlety in relationship between the flexibility, dynamics and function of the protein. The more dynamic and hence flexible region is the cytoplasmic half of this membrane protein. The effective force constant of extracellular half is three times that of the total protein(0.33 N/m and 0.12 N/m respectively). The more fluctuating cytoplasmic side undergoes a conformational change while a proton is transferred. This is also evident in fluctuations measured through Debye-Waller factor in electron and x-diffraction of the purple membrane crystals which contains bacteriorhodopsin.

1.7.2 Internal Friction

In the kramers rate equation, the friction coefficient is due to the solvent friction. Ansari et. al. performed experiments on myoglobin to see how rates of conformational jumps change by varying the viscosity of the medium [74]. In their experiments the rates showed a deviation from their inverse relation with the viscosity of the medium. They argued, for a protein the friction can come from two mechanisms, one from the solvent molecules retarding the motion of the protein atoms that are at its surface, and the other coming from within the structure of the protein due to the atoms moving with respect to each other. They modified the kramers rate equation to account for the two sources of friction.

$$k = \frac{C}{\eta + \sigma} \exp\left(\frac{E_b}{k_b T}\right) \tag{1.9}$$

Where η represents the viscosity of the medium due to solvent friction following stoke's law and σ represents the viscosity coming due to the friction from the internal friction. An extra parameter σ, the internal viscosity, was added to compensate for the deviation hence providing the first evidence of internal friction in proteins.

Similar experiments have also been performed to investigate the role of internal friction on folding times. It is worthwhile to distinguish the internal friction of folded protein from that of the unfolded chain. There are two parts to the folding process. One is the initial collapse of the denatured protein to form a molten globule. Second is the further folding to helices and beta sheets to form a three dimensional tertiary structure. The Rouse model [75] determines the rate of the initial collapse while internal friction resulting from the core's rugged energy landscape determines the rate of folding to a final structure. This ruggedness provides local kinetic traps to the folding protein. Similar to Ansari's case, the internal friction in these cases is measured in an indirect manner. The rate dependence on solvent viscosity is measured and extrapolated to zero viscosity, to get the friction which is only due to the internal viscosity[76]. The validity of this method has been debated [77–79].

1.7.3 Atomic Force Microscope for stiffness of folded domain

The AFM has been used in many experiments on different types of proteins. Although there are thousands of papers written on this subject, efforts to estimate stiffness of a folded protein are rare.

In a typical experiment, force extension curves are measured. The extension in these plots is that of the polymer tether or the unfolded chain of a domain. The experiment allows one to measure the force needed to unfold a domain. Pulling experiments performed at different speeds and temperatures, allows one to estimate parameters of a one dimensional energy landscape using the Bell-Evans-Ritchie model

[45]. Parameters such as the barrier height (ΔG) separating the folded and unfolded states, as well as the distance to transition state from the free energy minima (x_β) can be quantified. The stiffness of a protein is estimated using $\Delta G = 1/2 \times k \times (x_\beta)^2$. Here, a parabolic shape of the energy barrier is assumed with k as the stiffness of folded minimum [80].

These indirect measurements of folded state's stiffness rely heavily on the models used to estimate energy landscape parameters from the force distributions of unfolding forces. It is shown that the choice of models may result in different estimates of parameters describing the energy barriers [42, 52]. The group of M. Rief has carried out experiments to measure the stiffness of proteins from pulling experiments. They have shown that the temperature softening of Dictyostelium discoideum Filamin (ddFLN4) occurs in the range of 5^0 to 37^0 C[80]. The stiffness was found to vary between 1.7 N/m to 0.25 N/m. With certain approximations, these experiments were first of their kind in providing the estimates of the stiffness of a folded protein.

1.7.4 Nanorheology on folded proteins

In contrast to indirect ways of measuring stiffness through thermal fluctuations, and internal friction by measuring dependence of refolding rates on solvent viscosity, Wang and Zocchi measured viscoelasticity of folded domains by applying sinusoidal stress and measuring the corresponding strain of the folded domains of Gunyalate Kinase [81–83]. The strain amplitude is recorded at different forces as a function of frequency. By modelling the folded domains as a Maxwell's viscoelastic element- a spring and dash-pot in series. Stiffness and damping coefficient are inferred by fitting data to the observed amplitude-response curve obtained by sinusoidally loading the protein molecule sandwiched between a gold nanoparticle and the substrate. Assuming stiffness of 5 pN/nm, damping coefficients was of the order 10^{-5} kg/s [82]. However, the experiments here were not on single molecules but on 10^7 of them at a time.

Even though this rheological method of probing material properties is applied on a bulk scale, with the technological advancements it has been possible to perform such measurements on a single molecule level as well. Before going into the details of the methods used, a brief introduction to rheology is warranted.

1.8 RHEOLOGY

Rheology is the study of material properties in terms of forces and the deformations these forces produce in them. The material properties can broadly be divided into two components - viscous and elastic. Typically, when stress, force per unit area, is applied to a material it will produce deformations or strain in it and when a material is deformed or strain is provided it develops stress within itself. The amount of deformation produced in the material gives an estimate of its elasticity whereas the time required to reach certain level of deformation is determined by its viscous component. Purely elastic materials do not dissipate energy when taken through loading and unloading cycles. Materials that are viscoelastic show hysteresis in the stress strain curve, with the area between the two curves depicting the energy lost in each cycle. These components are represented with springs and dashpot connected in a network that describes the material properties.

The elastic component of a material follows Hooke's law where the stress and strain are related to each other as

$$\sigma = E\epsilon \tag{1.10}$$

Here E is elastic constant known as Young's Modulus similar to the force constant in Hooke's law, ϵ is the strain produced in the material due to the σ stress applied on it. The viscous component has the following relation between stress η and the rate at which strain $\dot{\epsilon}$ is applied

$$\sigma = \eta\dot{\epsilon} \tag{1.11}$$

Here η is the viscosity of the material.

Typically a material has both properties, however one out of the two can dominate over the other. Due to this a vast array of models are used to describe the

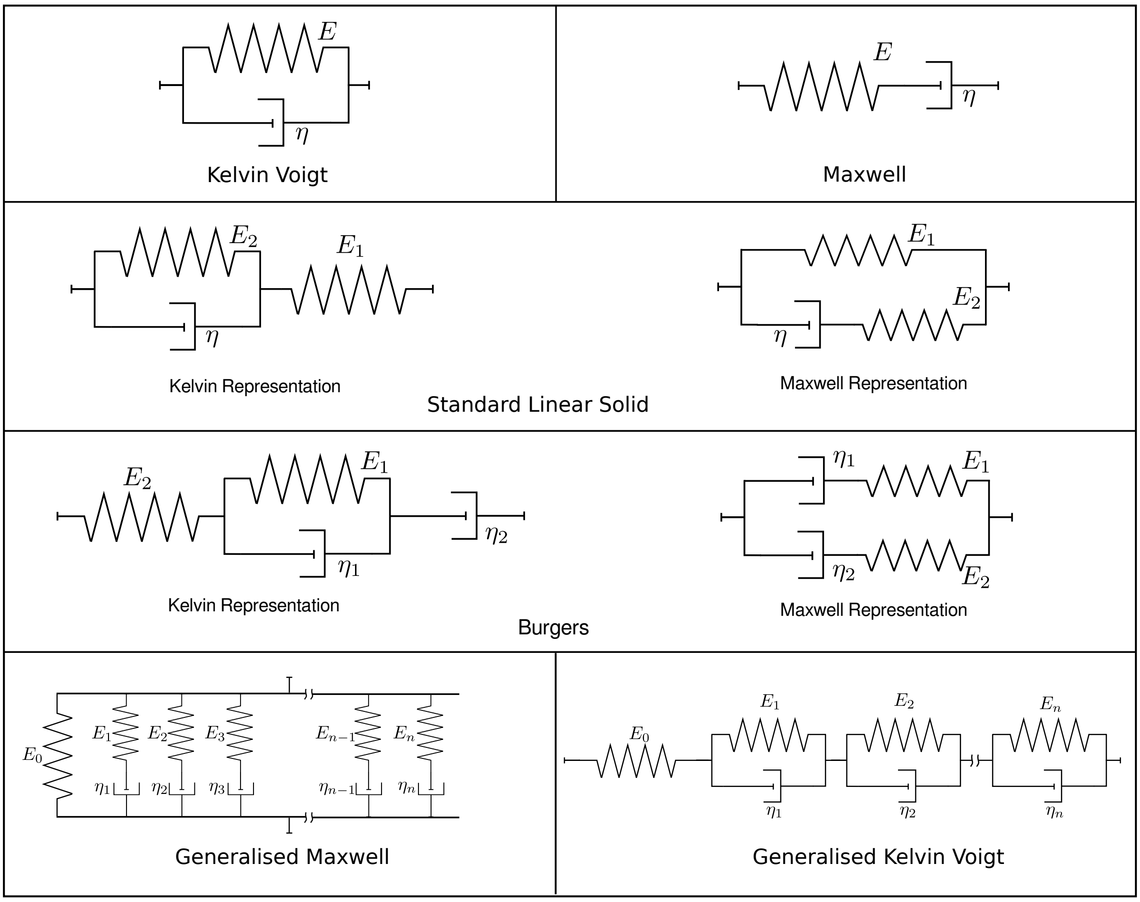
E
η
Kelvin Voigt
E
η
Maxwell
E_2
E_1
η
Kelvin Representation
E_1
E_2
η
Maxwell Representation
Standard Linear Solid
E_2
E_1
η_1
η_2
Kelvin Representation
η_1
E_1
η_2
E_2
Maxwell Representation
Burgers
E_0
E_1
E_2
E_3
E_{n-1}
E_n
η_1
η_2
η_3
η_{n-1}
η_n
Generalised Maxwell
E_0
E_1
E_2
E_n
η_1
η_2
η_n
Generalised Kelvin Voigt

Figure 1.4: Various models for describing viscoelastic nature of materials

properties of the material depending on their response. Here we will go deeper into the most prevalent ones.

1.8.1 Kelvin Voigt model

When the material under investigation behaves more like a solid, ie, under constant stress the strain produced in it tends to a constant value, the Kelvin Voigt model of viscoelasticity is employed[84]. This phenomenon is called creep. It consists of a spring that is attached in parallel to a Newtonian damper. The dynamics of the material are governed by the following differential equation

$$\sigma = \eta\dot{\epsilon} + E\epsilon \tag{1.12}$$

The total stress in the material is the sum of individual stresses across the spring and the dashpot. However, the strain in both the components is same. Applying a constant load to the material the strain produced in it reaches a maximum value as the time tends to very large values. The rate at which the strain is produced also decreases with time so that it reaches a maximum value of $\frac{E}{\sigma}$. When the load is removed the material goes back to it initial state with $\epsilon = 0$, hence this model also used to describe the reversible deformation in materials. The kelvin-voigt model predicts creep in materials accurately.

1.8.2 MAXWELL MODEL

This model describes the materials behaving more like liquids, under constant load the strain produced in them keeps on increases, but the stress developed eventually relaxes as time progresses[84]. The models consists of a spring and a dashpot connected in series. The dynamics of of the material are then governed by the differential equation

$$\sigma + \frac{\eta}{E}\dot{\sigma} = E\epsilon \tag{1.13}$$

In this case, when under a constant load the stress developed across the spring and the dashpot is the same. However, the total strain is the sum of contributions from the elastic and the viscous components, ie, the spring and the dashpot. The strain across the elastic component is developed instantaneously and reverts back to zero as soon as the load is removed whereas for the viscous component the strain continuously grows with time as long as the load is present. The Maxwell model accurately predicts that the stress in materials relax exponentially with time, however it fails in describing creep accurately.

1.8.3 STANDARD LINEAR SOLID

The standard linear solid model, also referred to as the zener model[84], predicts properties of creep and stress relaxation in materials accurately. The model can be represented in two ways

i) *Maxwell Representation:*

$$\sigma + \frac{\eta}{E_2}\dot{\sigma} = E_1\epsilon + \eta\frac{E_1 + E_2}{E_2}\dot{\epsilon} \tag{1.14}$$

ii) *Kelvin Representation*

$$\sigma + \frac{\eta}{E_1 + E_2}\dot{\sigma} = \frac{E_1}{E_1 + E_2}\epsilon + \eta\frac{E_1}{E_1 + E_2}\dot{\epsilon} \tag{1.15}$$

When a constant stress is applied to the material, the elastic component to the strain increases to a non-zero value instantaneously, after which it slowly tends to a steady state strain value referred to as the retarded elastic component of the strain.

1.8.4 Burgers Model

This model consists of a kelvin-voigt component, a spring and dashpot in series or two Maxwell components in parallel as shown in the figure below[84]. The salient features of this model are that it adds a flow property to the standard linear solid, so that the strain increases with time if a constant load is applied. The dynamics of the material are governed by the following differential equations.

i)*Maxwwell Representation*

$$\sigma + \Big(\frac{\eta_1}{E_1} + \frac{\eta_2}{E_2}\Big)\dot{\sigma} + \frac{\eta_1\eta_2}{E_1E_2}\ddot{\sigma} = (\eta_1 + \eta_2)\dot{\epsilon} + \frac{\eta_1\eta_2(E_1 + E_2)}{E_1E_2}\ddot{\epsilon} \tag{1.16}$$

ii)*Kelvin Representation*

$$\sigma + \Big(\frac{\eta_1}{E_1} + \frac{\eta_2}{E_1} + \frac{\eta_2}{E_2}\Big)\dot{\sigma} + \frac{\eta_1\eta_2}{E_1E_2}\ddot{\sigma} = \eta_2\dot{\epsilon} + \frac{\eta_1\eta_2}{E_1}\ddot{\epsilon} \tag{1.17}$$

1.8.5 Generalised Maxwell and Kelvin models

These models consist of arbitrary number of kelvin-voigt components connected in series for generalised kelvin arrangement whereas for generalised maxwell model, the maxwell components are connected in parallel with each other [84]. Each component in the arrangement shown in figure 1.4, represents the fact that relaxation can occur in multiple times. For instance, for a polymer network, constituent entangled strands can be of varied lengths. Shorter strands relax faster as compared to the longer ones. This results in a distribution of relaxation times which can be modelled with these generalised arrangements of multiple springs and dashpots.

1.8.6 OSCILLATORY RHEOLOGY

In general for soft viscoelastic solids, the creep or relaxation test is performed over minutes or days. But with these, it is not possible to accurately measure viscoelastic response at shorter time-scales, similar to the case for proteins. In such situations, a dynamic test is carried out by providing sinusoidal stress to the material and measuring sinusoidal strain.

$$\sigma(t) = \sigma_0 sin(\omega t) \tag{1.18}$$

For purely elastic solids, $\sigma = k\epsilon$. and hence, the resulting sinusoidal strain is

$$\epsilon(t) = \frac{\sigma_0}{k} sin(\omega t) \tag{1.19}$$

We find that the strain amplitude $\epsilon_0 = \sigma_0/k$ and since the response is immediate, both are in phase. For viscous liquid however, the stress is proportional to strain rate, $d\epsilon/dt = \sigma/\eta$, where η is viscosity. We get a sinusoidal strain,

$$\epsilon(t) = \frac{\sigma_0}{\eta\omega} cos(\omega t) \tag{1.20}$$

Thus, the strain produced is sinusoidal with a $\frac{\pi}{2}$ phase lag.

$$\epsilon(t) = \frac{\sigma_0}{\eta\omega} sin(\omega t - \frac{\pi}{2}) \tag{1.21}$$

For viscoelastic solids, which exhibits both elastic and viscous response, the strain lags behind by δ, where $0 < \delta < \frac{\pi}{2}$

$$\epsilon(t) = \frac{\sigma_0}{\eta\omega} sin(\omega t - \delta) = \frac{\sigma_0}{\eta\omega}[sin(\omega t)cos(\delta) - cos(\omega t)sin(\delta))] \tag{1.22}$$

In response to a sinusoidal stress, the material thus produces a sinusoidal strain which is a combination of both elastic and viscous response. To separate such a response one needs to measure the amplitudes of strain and the phase lag with respect to sinusoidal stress. From a nano-mechanics standpoint, internal friction and stiffness can be directly measured by deforming a single protein at a certain strain rate. To characterise the viscoelasticity of a single protein one needs to strain it periodically and measure the in-phase and out-of-phase components of the stress generated or vice versa.

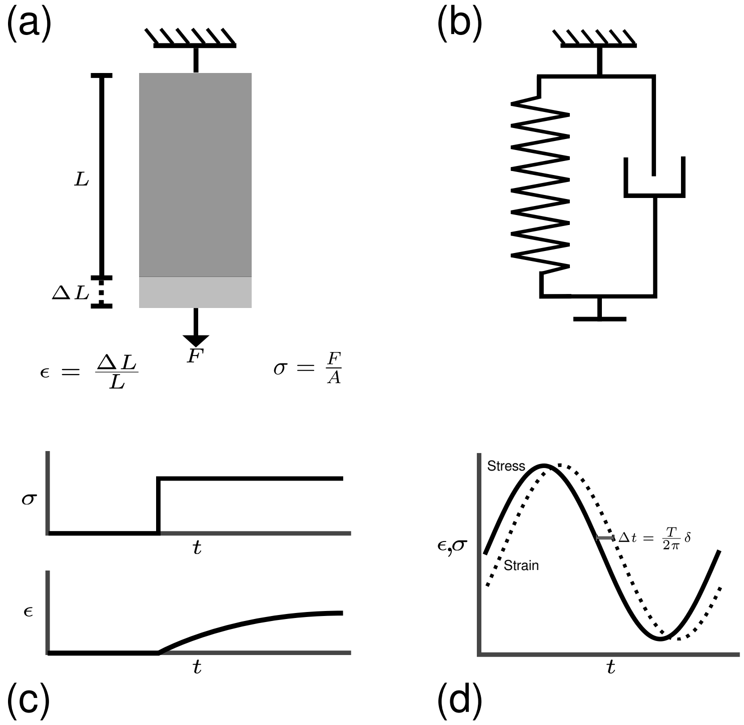
(a)
(b)
L
ΔL
F
$\epsilon = \frac{\Delta L}{L}$
$\sigma = \frac{F}{A}$
σ
t
ϵ
t
(c)
Stress
ϵ,σ
$\Delta t = \frac{T}{2\pi}\delta$
Strain
t
(d)

Figure 1.5: a) Figure showing stress and strain in context of material of length L and cross section A. b) Rheological model for a material described by Kelvin Voigt viscoelasticity. c) Response of a material with Kelvin Voigt viscoelasticity. The strain slowly reaches a steady state strain in response to a step stress d) Response of a viscoelastic material to periodic loading. The strain lag behind the stress.

1.9 Dynamic AFM for single proteins

As discussed earlier, we need to apply sinusoidal stress to a folded protein and measure the resulting strain and its phase lag in order to probe the viscoelasticity. In AFM, the protein under investigation is under the AFM tip and stiffness of the cantilever determines the amount of force on the protein if the tip performs oscillatory motion (figure 1.6). This sinusoidal force produces deformation in the protein and needs to be measured in order to infer its viscoelastic response. An artefact-free tip amplitude and phase with respect to drive is crucial to obtain this. We will discuss the AFM and dynamic AFM in detail in the next chapter, here we review the previous attempts at measuring viscoelasticity using AFM.

1.9.1 Dynamic AFM measurement scheme

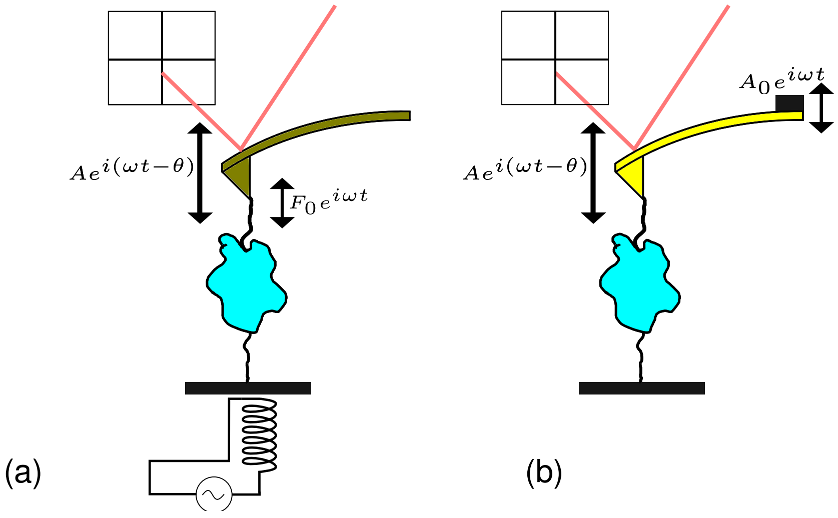

Figure 1.6: Conventional dynamic AFM scheme. a) The cantilever with a magnetic coating is driven from the tip using a magnetic field. b) The cantilever is driven from the base using a dither piezo

In 1987, within a year of AFM's discovery[30], Martin, Williams and Wickramashinge vibrated the cantilever on resonance to measure changes in its amplitude as it approached a substrate[85]. This allowed stable imaging and better resolution.

This was further improved by Albrecht et. al. by introducing frequency tracking to the AFM [86]. Since then, dynamic AFM measurements are performed by measuring amplitude modulations or frequency modulations produced in a resonant cantilever as the tip interacts with the substrate. Historically, the complications of cantilever dynamics on resonance was a major challenge in quantifying nanoscale force measurement using dynamic AFM. Figure 1.6 shows a schematic of dynamic Atomic Force Microscopy to measure nanoscale viscoelasticity of a material beneath the tip.

Quantitative estimates of forces from measured parameters are difficult when the tip is oscillated at amplitudes larger than the range over which one can linearize the potential. Another technical challenge, particularly when the cantilever is vibrated in viscous medium like water, has been the spurious resonance peaks and phase lags between the cantilever's drive and the tip. Accurately determining phase is ever so important in order to quantify dissipative processes in the material held beneath the tip [87]. This issue is now resolved to certain extent by techniques such as photothermal [88] or magnetic driving of the tip itself[89]. The conventional resonant dynamic AFM has been extremely successful in ultra high Vacuum environment as well as at ambient pressures. Owing to the complications of cantilever hydrodynamics in viscous medium, it's use is mainly restricted to these conditions, albeit with a few exceptions.

It was realised that for successful measurement of single molecule viscoelasticity, off-resonance operation with small tip-amplitude is better suited [90]. In 1999, first two experiments on measuring mechanical response of single molecules by dynamic AFM were reported. Liu et al. measured stiffness of single unfolded chromatin constructs adhered to the glass substrate [90]. Lantz et. al pulled α helices using similar method [91]. Both methods resorted to using tip excitation by magnetic force generated by a solenoid as shown in figure 1.6. Surprisingly, both these measurements do not comment on phase lags, crucial for measuring viscoelasticity of a single biomolecule.

In following years, there have been few attempts at measuring response of single molecules using dynamic AFM. Typically, these measurements have used the phase lag between the drive and the cantilever signal to infer internal friction of unfolded chains. Occasionally, the friction coefficient is inferred from fitting a Lorentzian to the thermally driven cantilever peak and measuring changes therein when the molecule is attached to the tip[92].

Sakai et al. measured stiffness of the polystyrene chain by oscillating the substrate [93]. Kageshima et al. measured conformation changes in α-helices by measuring their stiffness[94]. Kawakami et al. claimed measurement of stiffness and internal friction of single PEG chain by driving the tip by magnetic excitation[95]. Dextran's viscoelastic properties are reported by sweeping the cantilever through its resonance using magnetic forcing at different extensions of the molecule. The same group later reported viscoelasticity of dextran by attaching it to a thermally driven cantilever. Transverse dynamic mode AFM, wherein the tip is oscillated laterally was used to measure viscoelasticity of a tethered molecule [96]. Humphris et al. used active quality control to measure viscoelasticity of a single dextran chain [97]. Forbes and Wang attempted to measure stiffness of titin to show intermediate [98] . In-phase and out-of-phase stress strain response was found by Okajima et al. for BCA 1 and BCA 2 respectively by driving the substrate[99]. Bacteriorhodopsin's viscoelasticity was reported by Janovjak et al.[100]. Bippes et al. measured the viscoelasticity of dextran from brownian motion of thermally driven cantilever [101]. Kawakami et al. have reported viscoelasticity of unfolded chain of IgG domains of titin [102].

1.10 OBJECTIVES & MOTIVATIONS

These experiments in the early years reported friction coefficients of unfolded chain to be of the order $\sim 10^{-6} kg/s$. It yielded diffusion coefficient, which were five orders of magnitude smaller than those obtained with optical techniques, such as FRET.

Berkovich et al. [103] provided an explanation for this discrepancy by arguing that the cantilever or the probe to which, the molecule is tethered, relaxes much slower than the molecule itself. Hence, the diffusion coefficient is largely determined by the probe relaxation, which in turn depends on its size. After this study there have not been many studies in the field and the interest in application of dynamic atomic force spectroscopy has fizzled out. Recently, Benedetti et al. [104] have shown that the phase lag in cantilever bending signal with respect to drive was a result of change in stiffness, and claims of measurement of internal friction were an artefact of measurements. Further, solidifying the belief that dynamic measurements from AFM cannot be used to measure dissipative properties of single molecules. In our previous work, we have measured stiffness of the unfolded titin chains and have shown that internal friction of the chain is immeasurably low [87]. Further, we have checked the limits in which point-mass model of the cantilever dynamics is valid for data analysis [105]. It is stressed that to use point-mass model, one needs to satisfy stringent experimental parameters for artefact-free estimates of viscoelasticity.

Despite its importance, the activity in using dynamic AFM to measure single protein's viscoelastic response has not flourished. There are about 25 reports of dynamic AFM for protein's mechanical response as opposed to thousands for static mode. The motivation behind this work is to re-establish dynamic mode AFM as a tool for artefact free measurement of viscoelasticity of single molecules. And in doing so, measure the dynamic response of a folded protein subjected to oscillatory forcing. The objectives of this thesis are as follows

1. Implement off-resonance dynamic measurement scheme to perform artefact free oscillatory rheology of a polyprotein.
2. Measure displacement of the cantilever tip as opposed to bending, which becomes essential when working at off-resonance frequencies.
3. Develop a model to extract the viscoelasticity of the folded protein from the total response of the cantilever which contains contributions from the unfolded protein and surface damping.

In the next chapter we will be going through the theory of cantilever dynamics and discuss in detail the difficulties in performing such experiments and how these were circumvented in this work.

BIBLIOGRAPHY

[1] Engelbert Buxbaum. *Fundamentals of protein structure and function*, volume 31. Springer, 2007.

[2] Haruo Suzuki. *How enzymes work: from structure to function.* Crc Press, 2019.

[3] Daniel A Fletcher and R Dyche Mullins. Cell mechanics and the cytoskeleton. *Nature*, 463(7280):485–492, 2010.

[4] Alexei V Finkelstein and Oleg Ptitsyn. *Protein physics: a course of lectures.* Elsevier, 2016.

[5] Linus Pauling and Robert B Corey. Configuration of polypeptide chains. 1951.

[6] Arthur S Edison. Linus pauling and the planar peptide bond. *Nature structural biology*, 8(3):201–202, 2001.

[7] Cyrus Levinthal. Molecular model-building by computer. *Scientific american*, 214(6):42–53, 1966.

[8] William A Eaton. Modern kinetics and mechanism of protein folding: A retrospective. *The Journal of Physical Chemistry B*, 125(14):3452–3467, 2021.

[9] John Jumper, Richard Evans, Alexander Pritzel, Tim Green, Michael Figurnov, Olaf Ronneberger, Kathryn Tunyasuvunakool, Russ Bates, Augustin Žídek, Anna Potapenko, et al. Highly accurate protein structure prediction with alphafold. *Nature*, 596(7873):583–589, 2021.

[10] Brian Kuhlman and Philip Bradley. Advances in protein structure prediction and design. *Nature Reviews Molecular Cell Biology*, 20(11):681–697, 2019.

[11] Sandhya Bhatia and Jayant B Udgaonkar. Heterogeneity in protein folding and unfolding reactions. *Chemical Reviews*, 122(9):8911–8935, 2022.

[12] José Nelson Onuchic, Zaida Luthey-Schulten, and Peter G Wolynes. Theory of protein folding: the energy landscape perspective. *Annual review of physical chemistry*, 48(1):545–600, 1997.

[13] Michael Schlierf and Matthias Rief. Single-molecule unfolding force distributions reveal a funnel-shaped energy landscape. *Biophysical journal*, 90(4):L33–L35, 2006.

[14] C Nick Pace. Conformational stability of globular proteins. *Trends in biochemical sciences*, 15(1):14–17, 1990.

[15] C Nick Pace, J Martin Scholtz, and Gerald R Grimsley. Forces stabilizing proteins. *FEBS letters*, 588(14):2177–2184, 2014.

[16] C Nick Pace, Bret A Shirley, Marsha McNutt, and Ketan Gajiwala. Forces contributing to the conformational stability of proteins. *The FASEB journal*, 10(1):75–83, 1996.

[17] Hendrik Anthony Kramers. Brownian motion in a field of force and the diffusion model of chemical reactions. *Physica*, 7(4):284–304, 1940.

[18] Peter Hänggi, Peter Talkner, and Michal Borkovec. Reaction-rate theory: fifty years after kramers. *Reviews of modern physics*, 62(2):251, 1990.

[19] Keir C Neuman and Attila Nagy. Single-molecule force spectroscopy: optical tweezers, magnetic tweezers and atomic force microscopy. *Nature methods*, 5(6):491–505, 2008.

[20] Arthur Ashkin, James M Dziedzic, and T Yamane. Optical trapping and manipulation of single cells using infrared laser beams. *Nature*, 330(6150):769–771, 1987.

[21] Xinming Zhang, Lu Ma, and Yongli Zhang. High-resolution optical tweezers for single-molecule manipulation. *The Yale journal of biology and medicine*, 86(3):367, 2013.

[22] Jeffrey R Moffitt, Yann R Chemla, Steven B Smith, and Carlos Bustamante. Recent advances in optical tweezers. *Annu. Rev. Biochem.*, 77:205–228, 2008.

[23] Marco Capitanio and Francesco S Pavone. Interrogating biology with force: single molecule high-resolution measurements with optical tweezers. *Biophysical journal*, 105(6):1293–1303, 2013.

[24] Steven B Smith, Laura Finzi, and Carlos Bustamante. Direct mechanical measurements of the elasticity of single dna molecules by using magnetic beads. *Science*, 258(5085):1122–1126, 1992.

[25] La Chen, Andreas Offenhäusser, and Hans-Joachim Krause. Magnetic tweezers with high permeability electromagnets for fast actuation of magnetic beads. *Review of scientific instruments*, 86(4):044701, 2015.

[26] Guohua Yuan, Shimin Le, Mingxi Yao, Hui Qian, Xin Zhou, Jie Yan, and Hu Chen. Elasticity of the transition state leading to an unexpected mechanical stabilization of titin immunoglobulin domains. *Angewandte Chemie*, 129(20):5582–5585, 2017.

[27] Iwijn De Vlaminck and Cees Dekker. Recent advances in magnetic tweezers. *Annu. Rev. Biophys*, 41(1):453–472, 2012.

[28] Shimin Le, Ruchuan Liu, Chwee Teck Lim, and Jie Yan. Uncovering mechanosensing mechanisms at the single protein level using magnetic tweezers. *Methods*, 94:13–18, 2016.

[29] Devrim Kilinc and Gil U Lee. Advances in magnetic tweezers for single molecule and cell biophysics. *Integrative Biology*, 6(1):27–34, 2014.

[30] Gerd Binnig, Calvin F Quate, and Ch Gerber. Atomic force microscope. *Physical review letters*, 56(9):930, 1986.

[31] Franz J Giessibl. Afm's path to atomic resolution. *Materials Today*, 8(5):32–41, 2005.

[32] Peter M Hoffmann, Steve Jeffery, John B Pethica, H Özgür Özer, and Ahmet Oral. Energy dissipation in atomic force microscopy and atomic loss processes. *Physical Review Letters*, 87(26):265502, 2001.

[33] MP Murrell, ME Welland, SJ O'Shea, TMH Wong, JR Barnes, AW McKinnon, Marc Heyns, and S Verhaverbeke. Spatially resolved electrical measurements of sio2 gate oxides using atomic force microscopy. *Applied physics letters*, 62(7):786–788, 1993.

[34] Manuel Nonnenmacher, MP o'Boyle, and H Kumar Wickramasinghe. Kelvin probe force microscopy. *Applied physics letters*, 58(25):2921–2923, 1991.

[35] Anja Vinckier and Giorgio Semenza. Measuring elasticity of biological materials by atomic force microscopy. *FEBS letters*, 430(1-2):12–16, 1998.

[36] Keita Mitsui, Masahiko Hara, and Atsushi Ikai. Mechanical unfolding of a2-macroglobulin molecules with atomic force microscope. *FEBS letters*, 385(1-2):29–33, 1996.

[37] Jordanka Zlatanova, Stuart M Lindsay, and Sanford H Leuba. Single molecule force spectroscopy in biology using the atomic force microscope. *Progress in biophysics and molecular biology*, 74(1-2):37–61, 2000.

[38] Hauke Clausen-Schaumann, Matthias Rief, Carolin Tolksdorf, and Hermann E Gaub. Mechanical stability of single dna molecules. *Biophysical journal*, 78(4):1997–2007, 2000.

[39] Hauke Clausen-Schaumann, Markus Seitz, Rupert Krautbauer, and Hermann E Gaub. Force spectroscopy with single bio-molecules. *Current opinion in chemical biology*, 4(5):524–530, 2000.

[40] Toni Hoffmann and Lorna Dougan. Single molecule force spectroscopy using polyproteins. *Chemical Society Reviews*, 41(14):4781–4796, 2012.

[41] Ionel Popa, Pallav Kosuri, Jorge Alegre-Cebollada, Sergi Garcia-Manyes, and Julio M Fernandez. Force dependency of biochemical reactions measured by single-molecule force-clamp spectroscopy. *Nature protocols*, 8(7):1261–1276, 2013.

[42] Megan L Hughes and Lorna Dougan. The physics of pulling polyproteins: a review of single molecule force spectroscopy using the afm to study protein unfolding. *Reports on Progress in Physics*, 79(7):076601, 2016.

[43] John F Marko and Eric D Siggia. Stretching dna. *Macromolecules*, 28(26):8759–8770, 1995.

[44] Carlos Bustamante, John F Marko, Eric D Siggia, and S Smith. Entropic elasticity of λ-phage dna. *Science*, 265(5178):1599–1600, 1994.

[45] Evan Evans and Ken Ritchie. Dynamic strength of molecular adhesion bonds. *Biophysical journal*, 72(4):1541–1555, 1997.

[46] Evan Evans. Probing the relation between force—lifetime—and chemistry in single molecular bonds. *Annual review of biophysics and biomolecular structure*, 30(1):105–128, 2001.

[47] George I Bell. Models for the specific adhesion of cells to cells: a theoretical framework for adhesion mediated by reversible bonds between cell surface molecules. *Science*, 200(4342):618–627, 1978.

[48] Felix Rico, Laura Gonzalez, Ignacio Casuso, Manel Puig-Vidal, and Simon

Scheuring. High-speed force spectroscopy unfolds titin at the velocity of molecular dynamics simulations. *science*, 342(6159):741–743, 2013.

[49] Olga K Dudko, Gerhard Hummer, and Attila Szabo. Intrinsic rates and activation free energies from single-molecule pulling experiments. *Physical review letters*, 96(10):108101, 2006.

[50] Olga K Dudko, Gerhard Hummer, and Attila Szabo. Theory, analysis, and interpretation of single-molecule force spectroscopy experiments. *Proceedings of the National Academy of Sciences*, 105(41):15755–15760, 2008.

[51] Raymond W Friddle, Aleksandr Noy, and James J De Yoreo. Interpreting the widespread nonlinear force spectra of intermolecular bonds. *Proceedings of the National Academy of Sciences*, 109(34):13573–13578, 2012.

[52] Changbong Hyeon and D Thirumalai. Measuring the energy landscape roughness and the transition state location of biomolecules using single molecule mechanical unfolding experiments. *Journal of Physics: Condensed Matter*, 19(11):113101, 2007.

[53] Dmitrii E Makarov. Perspective: Mechanochemistry of biological and synthetic molecules. *The Journal of chemical physics*, 144(3):030901, 2016.

[54] Robert Zwanzig. Dynamical disorder: Passage through a fluctuating bottleneck. *The Journal of chemical physics*, 97(5):3587–3589, 1992.

[55] Changbong Hyeon, Michael Hinczewski, and D Thirumalai. Evidence of disorder in biological molecules from single molecule pulling experiments. *Physical review letters*, 112(13):138101, 2014.

[56] Michael Hinczewski, Changbong Hyeon, and Devarajan Thirumalai. Directly measuring single-molecule heterogeneity using force spectroscopy. *Proceedings of the National Academy of Sciences*, 113(27):E3852–E3861, 2016.

[57] Pavel I Zhuravlev, Michael Hinczewski, Shaon Chakrabarti, Susan Marqusee, and Devarajan Thirumalai. Force-dependent switch in protein unfolding pathways and transition-state movements. *Proceedings of the National Academy of Sciences*, 113(6):E715–E724, 2016.

[58] Robert Zwanzig. Diffusion in a rough potential. *Proceedings of the National Academy of Sciences*, 85(7):2029–2030, 1988.

[59] Changbong Hyeon and D Thirumalai. Can energy landscape roughness of proteins and rna be measured by using mechanical unfolding experiments? *Proceedings of the National Academy of Sciences*, 100(18):10249–10253, 2003.

[60] Reinat Nevo, Vlad Brumfeld, Ruti Kapon, Peter Hinterdorfer, and Ziv Reich. Direct measurement of protein energy landscape roughness. *EMBO reports*, 6(5):482–486, 2005.

[61] Jakob T Bullerjahn, Sebastian Sturm, and Klaus Kroy. Theory of rapid force spectroscopy. *Nature communications*, 5(1):1–10, 2014.

[62] B. Alberts, D. Bray, J. Lewis, M. Raff, K. Roberts, and J.D. Watson. *Molecular Biology of the Cell*. Garland, New York, 4th edition, 2002.

[63] Bruce Alberts. The cell as a collection overview of protein machines: Preparing the next generation of molecular biologists. *cell*, 92:291–294, 1998.

[64] David S Goodsell. *The machinery of life*. Copernicus New York, NY, 2009.

[65] Giuseppe Zaccai. How soft is a protein? a protein dynamics force constant measured by neutron scattering. *Science*, 288(5471):1604–1607, 2000.

[66] Mingdong Dong, Sudhir Husale, and Ozgur Sahin. Determination of protein structural flexibility by microsecond force spectroscopy. *Nature nanotechnology*, 4(8):514–517, 2009.

[67] Hans Frauenfelder, Stephen G Sligar, and Peter G Wolynes. The energy landscapes and motions of proteins. *Science*, 254(5038):1598–1603, 1991.

[68] Ricky K Soong, George D Bachand, Hercules P Neves, Anatoli G Olkhovets, Harold G Craighead, and Carlo D Montemagno. Powering an inorganic nanodevice with a biomolecular motor. *Science*, 290(5496):1555–1558, 2000.

[69] Jonathon Howard. *Mechanics of motor proteins and the cytoskeleton.* Sinauer associates Sunderland, MA, 2001.

[70] H.A. Barnes, K.W.H.A.B. John Fletcher Hutton, J.F. Hutton, and K. Walters. *An Introduction to Rheology.* Rheology Series. Elsevier Science, 1989.

[71] Beth G Wensley, Sarah Batey, Fleur AC Bone, Zheng Ming Chan, Nuala R Tumelty, Annette Steward, Lee Gyan Kwa, Alessandro Borgia, and Jane Clarke. Experimental evidence for a frustrated energy landscape in a three-helix-bundle protein family. *Nature*, 463(7281):685–688, 2010.

[72] Wolfgang Doster, Stephen Cusack, and Winfried Petry. Dynamical transition of myoglobin revealed by inelastic neutron scattering. *Nature*, 337(6209):754–756, 1989.

[73] Giuseppe Zaccai. Neutron scattering perspectives for protein dynamics. *Journal of Non-Crystalline Solids*, 357(2):615–621, 2011.

[74] Anjum Ansari, Colleen M Jones, Eric R Henry, James Hofrichter, and William A Eaton. The role of solvent viscosity in the dynamics of protein conformational changes. *Science*, 256(5065):1796–1798, 1992.

[75] Prince E Rouse Jr. A theory of the linear viscoelastic properties of dilute solutions of coiling polymers. *The Journal of Chemical Physics*, 21(7):1272–1280, 1953.

[76] Troy Cellmer, Eric R Henry, James Hofrichter, and William A Eaton. Measuring internal friction of an ultrafast-folding protein. *Proceedings of the National Academy of Sciences*, 105(47):18320–18325, 2008.

[77] Robert B Best and Gerhard Hummer. Coordinate-dependent diffusion in protein folding. *Proceedings of the National Academy of Sciences*, 107(3):1088–1093, 2010.

[78] Suzette A Pabit, Heinrich Roder, and Stephen J Hagen. Internal friction controls the speed of protein folding from a compact configuration. *Biochemistry*, 43(39):12532–12538, 2004.

[79] VM Hridya and Arnab Mukherjee. Probing the viscosity dependence of rate: internal friction or the lack of friction? *The Journal of Physical Chemistry B*, 122(39):9081–9086, 2018.

[80] Michael Schlierf and Matthias Rief. Temperature softening of a protein in single-molecule experiments. *Journal of molecular biology*, 354(2):497–503, 2005.

[81] Yong Wang and Giovanni Zocchi. Elasticity of globular proteins measured from the ac susceptibility. *Physical review letters*, 105(23):238104, 2010.

[82] Yong Wang and Giovanni Zocchi. The folded protein as a viscoelastic solid. *EPL (Europhysics Letters)*, 96(1):18003, 2011.

[83] Yong Wang and Giovanni Zocchi. Viscoelastic transition and yield strain of the folded protein. *PLoS One*, 6(12):e28097, 2011.

[84] Roderic Lakes and Roderic S Lakes. *Viscoelastic materials.* Cambridge university press, 2009.

[85] Yves Martin, Clayton C Williams, and H Kumar Wickramasinghe. Atomic force microscope–force mapping and profiling on a sub 100-å scale. *Journal of applied Physics*, 61(10):4723–4729, 1987.

[86] Thomas R Albrecht, Peter Grütter, David Horne, and Daniel Rugar. Frequency modulation detection using high-q cantilevers for enhanced force microscope sensitivity. *Journal of applied physics*, 69(2):668–673, 1991.

[87] Shatruhan Singh Rajput, Surya Pratap S Deopa, Jyoti Yadav, Vikhyaat Ahlawat, Saurabh Talele, and Shivprasad Patil. The nano-scale viscoelasticity using atomic force microscopy in liquid environment. *Nanotechnology*, 32(8):085103, 2020.

[88] N Umeda, S Ishizaki, and H Uwai. Scanning attractive force microscope using photothermal vibration. *Journal of Vacuum Science & Technology B: Microelectronics and Nanometer Structures Processing, Measurement, and Phenomena*, 9(2):1318–1322, 1991.

[89] Ernst-Ludwig Florin, Manfred Radmacher, Bernhard Fleck, and Hermann E Gaub. Atomic force microscope with magnetic force modulation. *Review of Scientific Instruments*, 65(3):639–643, 1994.

[90] YZ Liu, SH Leuba, and Stuart Lindsay. Relationship between stiffness and force in single molecule pulling experiments. *Langmuir*, 15(24):8547–8548, 1999.

[91] Mark A Lantz, Suzanne P Jarvis, Hiroshi Tokumoto, Tomasz Martynski, Toshinori Kusumi, Chikashi Nakamura, and Jun Miyake. Stretching the α-helix: a direct measure of the hydrogen-bond energy of a single-peptide molecule. *Chemical Physics Letters*, 315(1-2):61–68, 1999.

[92] Masaru Kawakami, Katherine Byrne, Bhavin Khatri, Tom CB Mcleish, Sheena E Radford, and D Alastair Smith. Viscoelastic properties of single polysaccharide molecules determined by analysis of thermally driven oscillations of an atomic force microscope cantilever. *Langmuir*, 20(21):9299–9303, 2004.

[93] Yasuhiro Sakai, Takayuki Ikehara, Toshio Nishi, Ken Nakajima, and Masahiko Hara. Nanorheology measurement on a single polymer chain. *Applied physics letters*, 81(4):724–726, 2002.

[94] Masami Kageshima, Mark A Lantz, Suzanne P Jarvis, Hiroshi Tokumoto, Seiji Takeda, Arkadiusz Ptak, Chikashi Nakamura, and Jun Miyake. Insight into conformational changes of a single α-helix peptide molecule through stiffness measurements. *Chemical Physics Letters*, 343(1-2):77–82, 2001.

[95] Masaru Kawakami, Katherine Byrne, Bhavin S Khatri, Tom CB Mcleish, Sheena E Radford, and D Alastair Smith. Viscoelastic measurements of single molecules on a millisecond time scale by magnetically driven oscillation of an atomic force microscope cantilever. *Langmuir*, 21(10):4765–4772, 2005.

[96] ADL Humphris, M Antognozzi, TJ McMaster, and MJ Miles. Transverse dynamic force spectroscopy: a novel approach to determining the complex stiffness of a single molecule. *Langmuir*, 18(5):1729–1733, 2002.

[97] ADL Humphris, J Tamayo, and MJ Miles. Active quality factor control in liquids for force spectroscopy. *Langmuir*, 16(21):7891–7894, 2000.

[98] Jeffrey G Forbes and Kuan Wang. Simultaneous dynamic stiffness and extension profiles of single titin molecules: nanomechanical evidence for unfolding intermediates. *Journal of Vacuum Science & Technology A: Vacuum, Surfaces, and Films*, 22(4):1439–1443, 2004.

[99] Takaharu Okajima, Hideo Arakawa, Mohammad Taufiq Alam, Hiroshi Sekiguchi, and Atsushi Ikai. Dynamics of a partially stretched protein molecule studied using an atomic force microscope. *Biophysical chemistry*, 107(1):51–61, 2004.

[100] Harald Janovjak, Daniel J Müller, and Andrew DL Humphris. Molecular force modulation spectroscopy revealing the dynamic response of single bacteriorhodopsins. *Biophysical journal*, 88(2):1423–1431, 2005.

[101] Christian A Bippes, Andrew DL Humphris, Martin Stark, Daniel J Müller, and Harald Janovjak. Direct measurement of single-molecule visco-elasticity

in atomic force microscope force-extension experiments. *European Biophysics Journal*, 35(3):287–292, 2006.

[102] Masaru Kawakami, Katherine Byrne, David J Brockwell, Sheena E Radford, and D Alastair Smith. Viscoelastic study of the mechanical unfolding of a protein by afm. *Biophysical journal*, 91(2):L16–L18, 2006.

[103] Ronen Berkovich, Rodolfo I Hermans, Ionel Popa, Guillaume Stirnemann, Sergi Garcia-Manyes, Bruce J Berne, and Julio M Fernandez. Rate limit of protein elastic response is tether dependent. *Proceedings of the National Academy of Sciences*, 109(36):14416–14421, 2012.

[104] Fabrizio Benedetti, Yulia Gazizova, Andrzej J Kulik, Piotr E Marszalek, Dmitry V Klinov, Giovanni Dietler, and Sergey K Sekatskii. Can dissipative properties of single molecules be extracted from a force spectroscopy experiment? *Biophysical journal*, 111(6):1163–1172, 2016.

[105] Shatruhan Singh Rajput, Surya Pratap S Deopa, VJ Ajith, Sukrut C Kamerkar, and Shivprasad Vitthal Patil. Validity of point-mass model in off-resonance dynamic atomic force microscopy. *Nanotechnology*, 2021.

CHAPTER

TWO

CANTILEVER DYNAMICS

2.1 OVERVIEW

The first step in performing an AFM experiment involves calibrating the cantilever to obtain its parameters like quality factor, stiffness and resonance frequency. A physical model is required to obtain such parameters. We will be discussing two of such models - the point mass model and the continuous beam model. The point mass model involves approximating the cantilever by a point object having an effective mass attached to a spring along with damping due to the medium. In the static mode force spectroscopy experiments, the quantity to be determined is the force. This quantification is straightforward, as the stiffness obtained from the calibration, can be directly used to determine the force using the Hooke's law. However, when one starts to oscillate the cantilever to determine dynamic properties of the sample, one needs to perform more rigours modelling of the cantilever dynamics to obtain accurate relations between the experimental observables and the sample properties.

In the following sections we will be going into the details of cantilever dynamics.

2.2 Deflection Detection Scheme

The most widely used detection method of measuring cantilever bending is the optical beam deflection scheme. Due to the simplicity of this method [1, 2], it is widely popular and available in majority of the commercially available AFMs.

In this method the change in laser spot is monitored as the cantilever bends. From the figure 2.1, it is visible that the change in position of the laser spot on the photodiode happens only when the angle of incidence of the laser beam at the back of the cantilever changes. This implies that the beam deflection method is only sensitive to the bending of the cantilever and not its displacement. The sensitivity of this method in measuring cantilever bending is inversely proportional to the length. The more the length of the cantilever, the lesser is the change in its slope due to bending. However, the distance of the cantilever from the photodiode is directly proportional to the sensitivity. When taking a small angle approximation the sensitivity of this detection scheme can be approximately expressed as

$$\frac{\Delta A}{\Delta z} \approx 2\frac{D}{L} \tag{2.1}$$

where L is the length of the cantilever, D is the distance of the photodiode from the tip of the cantilever, ΔA is the change in the position of the laser spot at the photodiode and Δz is the change in the bending of the cantilever.

2.3 Point Mass Model

The cantilever used in the experiments are rectangular beams of width $\sim 25\mu m$ and length of around $130\mu m$ as shown in the figure 2.2(a). The thickness of the cantilever is approximately $1\mu m$. The tip that is present at the end of the cantilever is $15\mu m$ in height. The radius of the apex of the tip is usually $\sim 8nm$ for uncoated cantilevers and $\sim 40nm$ for gold coated ones. In the point mass model one assumes the dynamics of the cantilever to be governed by a damped harmonic oscillator model [3]. This leaves one with a very simple model which is given by

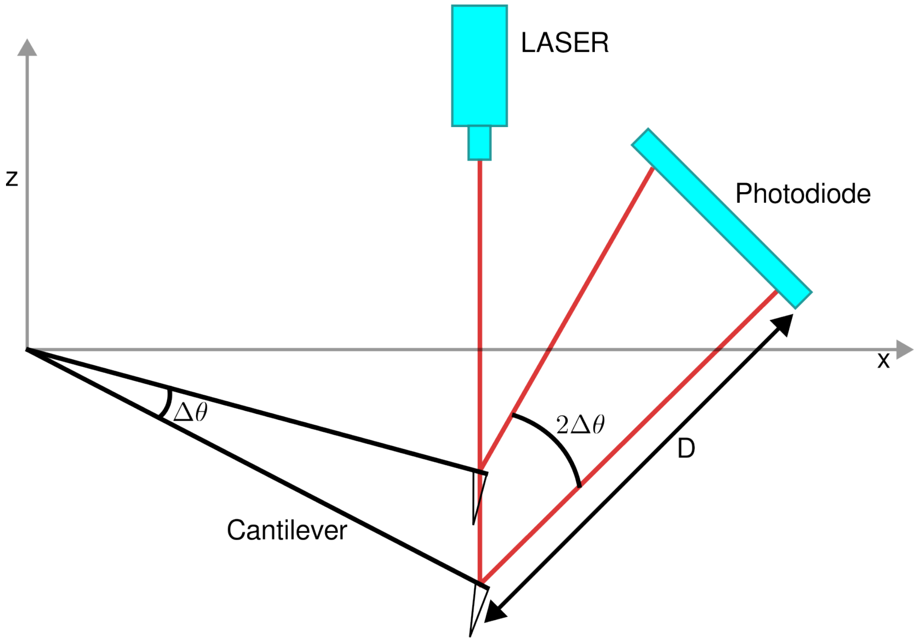

Figure 2.1: Schematic showing the optical beam deflection technique.

$$m\ddot{z} + k_c z + \frac{m\omega_0}{Q}\dot{z} = F_0 \cos \omega t + F_{ts}(d) \tag{2.2}$$

Where m,k_c and Q are the effective mass, stiffness and quality factor of the cantilever respectively. The effective mass m is $1/4$ times the actual mass m_c of the cantilever, this relation will be derived later in the chapter. The relation between the friction co-efficient γ_c and the quality factor is given by $Q = \frac{m\omega_0}{\gamma_c}$. F_0 is the amplitude of the oscillatory driving force. There are two co-ordinates here z and d. The co-ordinate z represents the bending in the cantilever, and d represents the co-ordinate on the which the interaction F_{ts} depends as shown in the figure 2.2(b).

The amplitude of the cantilever as a function of drive with no interaction force is given by

$$|A| = \frac{F_0/m}{\left[\left(\omega_0^2 - \omega^2\right)^2 + \left(\frac{\omega\omega_0}{Q}\right)^2\right]^{1/2}} \tag{2.3}$$

The phase lag of the cantilever tip from the drive is given by

$$\tan\theta = \frac{\omega\omega_0/Q}{\omega_0^2 - \omega^2} \tag{2.4}$$

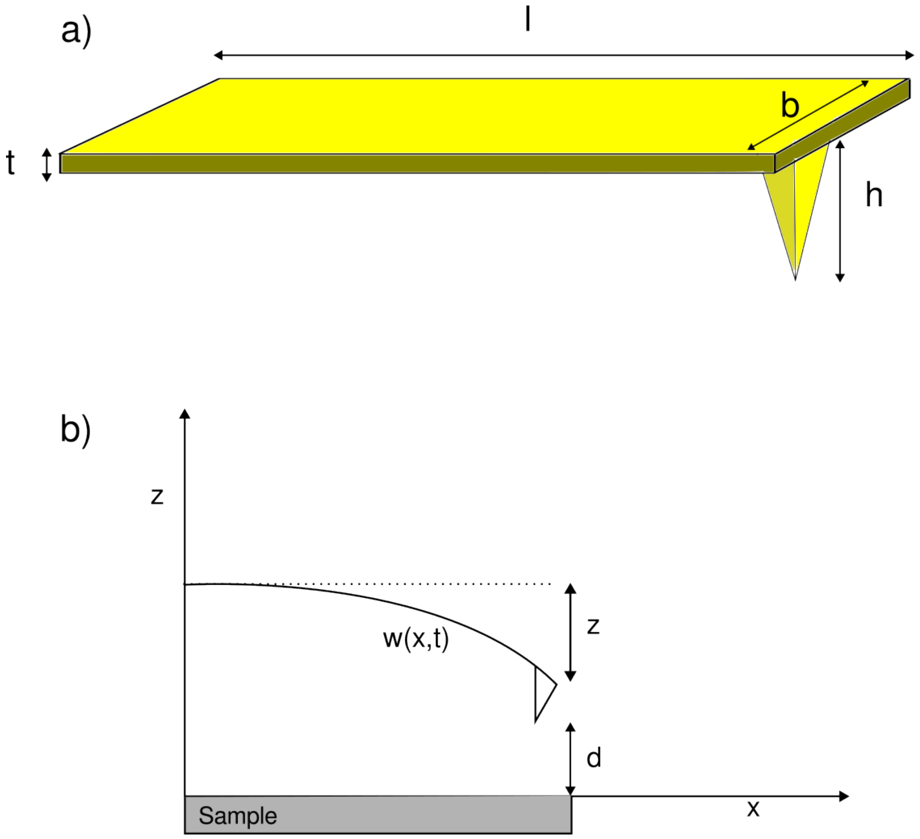

Figure 2.2: a) Dimensions of the cantilever l = $150\mu m$, b = $25\mu m$, t = $1\mu m$ and h = $15\mu m$. b) z is the deflection in the cantilever. d is the separation of the tip from the surface. w(x,t) is the displacement of the cantilever at x position along its length and time t

This relation can be used to calibrate the cantilever stiffness. The interaction term F_{ts} will be incorporated later in the chapter.

Calibration

The calibration of the cantilever is a two step process.

i) To calibrate the cantilever one has to first determine the sensitivity of the apparatus with the cantilever whose stiffness has to be calibrated. The sensitivity here refers the change in voltage output of the photo diode due to the bending of the cantilever as shown in the figure 2.3.

The cantilever is approached and sample pressed onto it till the setpoint voltage is reached. When the cantilever is in deep contact on a hard surface like glass, it can be assumed that the vertical deflection in the lever is equal to the motion of its base. The x-axis in the graph shows the motion of the cantilever base which done by a piezo which is already calibrated. When one fits a straight line to the deep contact region, the relation between cantilever deflection in length coordinates and the change in voltage at the photodiode is found, which is the sensitivity.

Typical values of sensitivity for optical beam detection techniques are $\sim 25nm/V$ or $40mV/nm$.

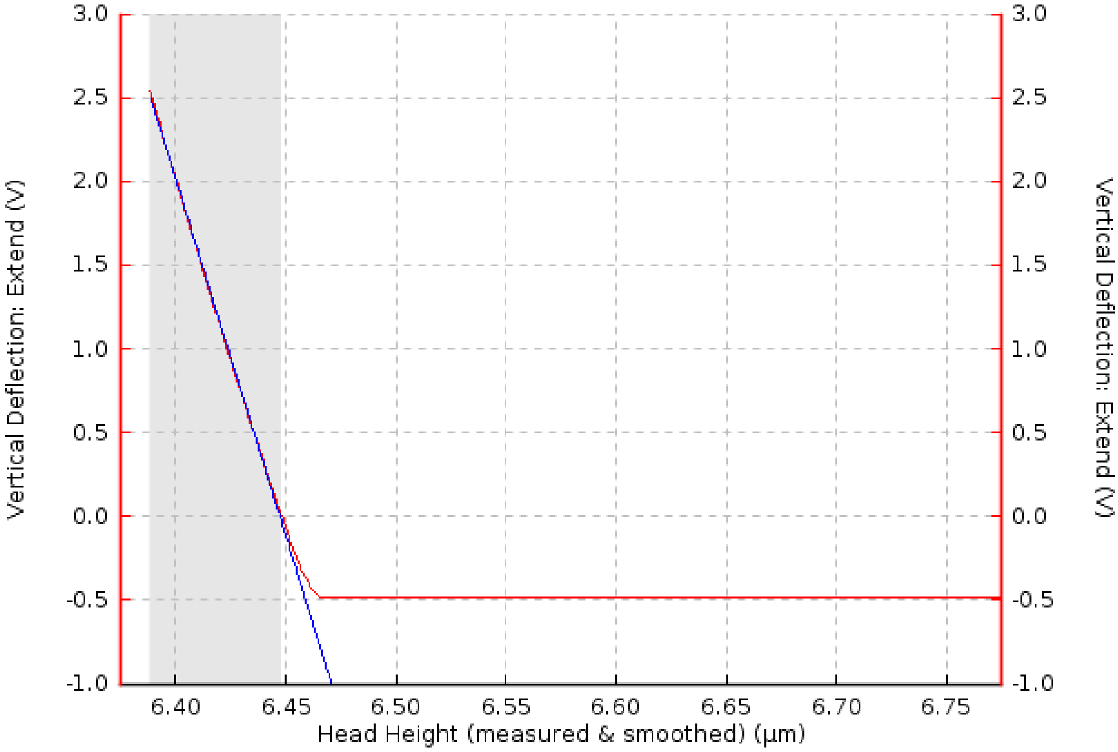

Figure 2.3: Graph showing calibration procedure. The redline depicts the voltage at the photodiode due to the cantilever deflection. After the contact region, it is seen that the vertical deflection signal changes linearly. A stright line (blue) is fit to obtain the sensitivity

ii) The most widely used method for calibrating a cantilever is the thermal tuning method [4]. In this method the thermal fluctuations of the cantilever due to the medium , liquid or air, are utilised in estimating the stiffness of the cantilever.

It makes use of the fact that each degree of freedom with quadratic power in the total energy, when in thermal equilibrium with the medium contains $\frac{1}{2}K_BT$. With K_b and T being the Boltzmann constant and temperature respectively.

The fluctuations at the tip of the cantilever are recorded as a time series and the PSD - power spectral density- as a function of frequency is calculated. The frequency response of the cantilever is then fitted to this PSD, and the area under the curve -the energy- is then equated to $\frac{1}{2}K_BT$. By doing this one can extract cantilever stiffness k_c, resonance frequency ω_0 and the quality factor Q.

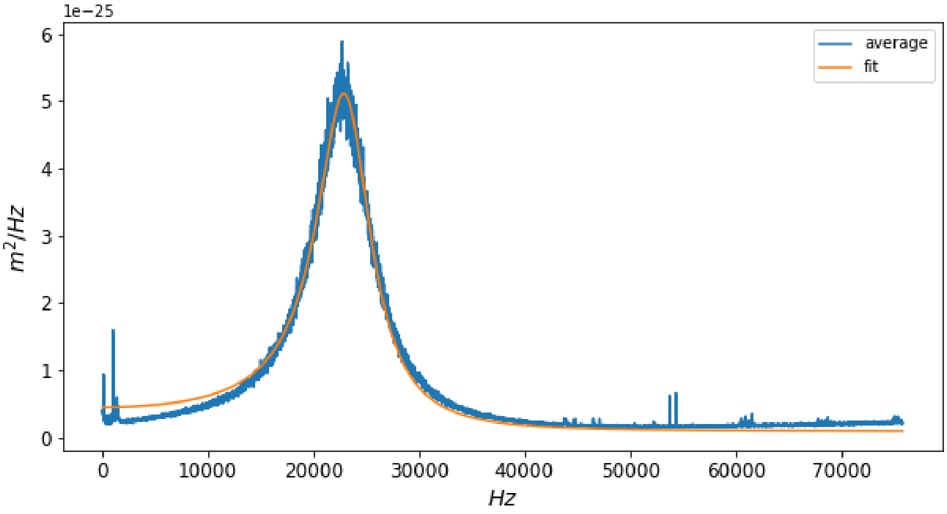

Figure 2.4: Graph showing the average power spectrum density (blue) of the fluctions of the cantilever. The orange curve represent the point mass model being fit to the PSD to obtain stiffness, quality factor and resonance

2.4 Continuous Beam Model:

To get the full description of the dynamics of the cantilever the well known Euler-Bernoulli beam equation is utilised [5]. For a cantilever in a viscous medium with a force acting at the tip the equation gets modified [6]and is given by

$$EI\left[\frac{\partial^4 w(x,t)}{\partial^4 x}+a_1\frac{\partial w(x,t)}{\partial t}\right]+\rho Wh\frac{\partial^2 w(x,t)}{\partial^2 t}=a_0\frac{\partial w(x,t)}{\partial t}+\delta(x-L)[F_{exc}(t)+F_{ts}(d)] \tag{2.5}$$

Here, $w(x,t)$ is the displacement of the cantilever in the y direction, that is perpendicular to the long axis. E, I and ρ are the young's modulus, moment of inertia and density of the cantilever respectively. W, h and L are the width, thickness and length respectively. The coefficients for internal and medium damping are a_0 and a_1 respectively.

The individual terms of in the differential equation represent the following quantities.

$EI\left[\frac{\partial^4 w(x,t)}{\partial^4 x}+a_1\frac{\partial w(x,t)}{\partial t}\right]$	elastic term and internal damping
$\rho Wh\frac{\partial^2 w(x,t)}{\partial^2 t}$	inertial term
$a_0\frac{\partial w(x,t)}{\partial t}$	medium damping
$\delta(x-L)[F_{exc}(t)+F_{ts}(d)]$	forcing term

To implement the condition where the force only acts on the end of the cantilever where the tip is present, the delta function is employed in the differential equation. The tip is neglected in this equation since it has negligible mass compared to the entire cantilever. The internal damping a_0 can also be neglected since it is much lower in magnitude compared to the other terms in the experimental conditions.

In order to solve this fourth order partial differential equation, the spatial and temporal components of the general solution are separated $w(x,t) = X(x)Y(t)$. The boundary conditions satisfied by the spatial part are $X(0) = 0$, $X'(0) = 0$, $X''(L) = 0$ and $X'''(L) = 0$ representing zero displacement and bending at the clamped end ($x = 0$) and zero force and stress at the free end ($x = L$) respectively. With these conditions discrete eigen modes can be obtained and the general solution can be written as a superposition of these modes. Each solution of this differential equation represents the flexural modes of the cantilever.

$$w(x,t) = \sum_{n=1}^{\infty} X_n(x) Y_n(t) \tag{2.6}$$

where $X_n(x)$ is given by

$$X_n(x) = \cos{(x_n \frac{x}{L})} - \cosh{(x_n \frac{x}{L})} - \frac{cos x_n + \cosh x_n}{\sin x_n + \sinh x_n}\Big[\sin{(x_n \frac{x}{L})} - \sinh{(x_n \frac{x}{L})}\Big] \tag{2.7}$$

The x_n are the roots of the equation $1 + \cosh x_n \cosh x_n = 0$ with $x_1 = 1.87$, $x_2 = 4.694$, $x_3 = 7.854$ and $x_4 = 10.996$. The orthogonality condition is given by

$$\int_0^L X_n(x) X_m(x) = L\delta_{n,m} \tag{2.8}$$

with $X_n(0) = 0$ and $X_n(L) = 2(-1)^n$

The temporal part of the solution for each mode $Y_n(t)$ is given by the differential equations

$$\ddot{Y}_n(t) + \frac{\omega_n}{Q_n}\dot{Y}(t) + \omega_n^2 Y_n(t) = \frac{F_n}{m_n} \tag{2.9}$$

where the following quantities are for the nth eigen mode

$$\omega_n^2 = (\frac{x_n}{L})^4 \frac{EI}{\rho W h} \qquad \text{eigen frequency}$$

$$m_n = \rho W h \int_0^L X_n^2(x) dx \qquad \text{effective mass}$$

$$Q_n = \frac{\omega_n}{a_0/\rho W h + a_1 \omega_n^2} \qquad \text{quality factor}$$

$$\begin{aligned} F_n(t) &= \int_0^L \delta(x-L)[F_{exc}(t) + F_{ts}(d)] X_n(x) dx \qquad \text{forcing} \\ &= 2(-1)^n [F_{exc}(t) + F_{ts}(d)] \end{aligned}$$

The total bending at the tip of the cantilever in terms of the spatial and temporal solutions can be written as $w(L,t) = \sum_{n=1}^{\infty} X_n(L) Y_n(t) = \sum_{n=1}^{\infty} z_n(t)$. Which can be written as

$$\ddot{z_n} + \frac{\omega_n}{Q_n}\dot{z_n} + \omega_n^2 z_n = \frac{F_n(t)}{m} \tag{2.10}$$

where $m = 0.25m_c$

It is debated, whether the point mass model captures the entire details of the cantilever dynamics sufficiently. For instance the point mass model cannot explain the higher modes in the cantilever frequency response. However, the fundamental mode contributes the most to the oscillation of the cantilever and the point mass model is an ideal choice in most experimental conditions.

2.5 EXCITATION SCHEMES

In this section we will discussing the two methods in which the cantilever can be driven for dynamic force spectroscopy. The first mode of the frequency response of the cantilever derived in the previous section will be used to describe the dynamics, which in essence is the point mass model. The resonance frequency ω_0 is of the fundamental mode, k_c is the cantilever stiffness, the friction co-efficient γ_c can be obtained from the quality factor. All these parameters are obtained after fitting the model to the thermal response of the cantilever as described previously.

Base Excitation:

In this case the cantilever is excited from the base sinusoidally $Ae^{i\omega t}$. The cantilever is treated as a point mass moving in a viscous medium while being connected to a spring with stiffness k_c and experiencing an interaction force. The friction coefficient of the cantilever due to damping from the surrounding liquid is γ_c. The equation of motion for this point mass can be written as [7].

$$m\frac{d^2z(t)}{dt^2} + \gamma_c\frac{dz(t)}{dt} + k_c(z(t) - Ae^{i\omega t}) - F_i = 0 \tag{2.11}$$

Here, z is the deflection of the cantilever, $m = 0.2425m_c + m_a$ is the effective mass of the moving cantilever with m_c and m_a being the cantilever and hydrodynamic added mass respectively, A_0 is the drive amplitude. The $\bar{k}$ and $\bar{\gamma}$- the stiffness and friction coefficient of the entity beneath the tip respectively are obtained after linearizing conservative and dissipative components of the interaction $F_i = \bar{k}z(t) + \bar{\gamma}\frac{dz(t)}{dt}$.

The above equation can also be written as

$$m\ddot{z} + (k_c + \bar{k})z + (\bar{\gamma} + \gamma_c)\dot{z} = k_c A_0 \exp i\omega t \tag{2.12}$$

Tip Excitation:

In this case the cantilever is excited from the tip sinusoidally with force $F_0 e^{i\omega t}$, while the tip also experiences the interaction force. The equation of motion for this point mass can be written as [7].

$$m\frac{d^2 z(t)}{dt^2} + \gamma_c \frac{dz(t)}{dt} + k_c z(t) - F_0 e^{i\omega t} - F_i = 0 \tag{2.13}$$

This too can be written as a damped harmonic oscillator equation

$$m\ddot{z} + (k_c + \bar{k})z + (\bar{\gamma} + \bar{\gamma}_c)\dot{z} = k_c A_0 \exp i\omega t \tag{2.14}$$

The only difference here is that A_0 here is the amplitude of the tip due to the force F_0 with no interaction present, rather than the base amplitude in the case of base excitation. One can reach the same equations for $\bar{k}$ and $\bar{\gamma}$ as in the previous case.

2.6 ON OR NEAR-RESONANCE OPERATION

For a cantilever that is oscillated near its resonance, the inertial and velocity dependent forces on it are large. Equation 12 and 14 are the equations of motion for a linear damped harmonic oscillator with the well known solutions.

$$|A| = \frac{k_c A_0}{\sqrt{(k_c + \bar{k})^2 \Big(1 - \frac{\omega^2}{\omega_0^2}\Big)^2 + (\gamma\omega)^2}}$$

$$\tan\theta = -\frac{\gamma\omega}{(k_c + \bar{k})\Big(1 - \frac{\omega^2}{\omega_0^2}\Big)}$$

Where ω_0 is given by $\sqrt{\frac{k_c+\bar{k}}{m}}$ and $\gamma = \bar{\gamma} + \gamma_c$.

In principle, the above equations can be inverted to obtain the stiffness and friction coefficient of the interaction. However, technically an experimenter is faced with a daunting task of measuring A, A_0 and phase lag θ accurately and free of artefacts. When experiments are performed on-resonance and the resultant amplitude and phase are used to obtain the stiffness and friction coefficient of the system beneath the tip, it is difficult to predict the phase behaviour seen in the experiments by modelling the cantilever alone[8–10].

Another challenge is to control amplitudes on resonance. The protein under investigation is subjected to large amplitudes and hence large oscillatory stress which may even exceed rupture forces. Secondly, determining phase lags due to viscous response of the protein is difficult since there are many spurious contributions to the phase signal, if the base of the cantilever is oscillated. However, this is not a major concern, if the tip is directly oscillated either by magnetic [11] or photo-thermal [12] means. Due to these concerns, one needs to perform the experiments at a frequency much lower than its resonance. Next we will turn our attention to dynamic AFM measurements in the off-resonance regime.

2.7 OFF-RESONANCE OPERATION

For off-resonance regime, the $1 - \frac{\omega^2}{\omega_0^2}$ term in equation becomes unity, after which we can solve for $\bar{k}$ and $\bar{\gamma}$ to get the stiffness and friction coefficient of the material beneath the tip.

$$\bar{k} = k_c\Big(\frac{A_0}{|A|}\cos\theta - 1\Big) \tag{2.15}$$

$$\bar{\gamma} = \frac{k_c A_0}{|A|\omega}\sin\theta \tag{2.16}$$

The main idea behind off-resonance operation is to drive the cantilever at such a low frequency where the friction and inertial forces on it become negligible. Due to this the response of the cantilever can be approximated by it static response.

$$A_0 - A \approx \frac{F_0}{k_c} \tag{2.17}$$

$$\theta \approx 0 \tag{2.18}$$

Where $A_0 - A$ represents the difference in displacements of the tip and the base, ie, the bending in the cantilever. Experimentally this implies when operating strictly at off-resonance frequency and no molecule is attached to the tip, the phase difference between the cantilever and the drive is close to zero. The base amplitude and the tip amplitude are same.

One can also arrive at the same expression by following a much simpler and intuitive method. For the off-resonance operation, the cantilever and the interaction are in series with each other. The conservative and dissipative components of the interaction are modelled as a spring and a dash-pot respectively. For such an arrangement we can write the force balance equation as

$$k_c(A_0 e^{i\omega t} - |A|e^{i(\omega t-\theta)}) = (\bar{k} + i\bar{\gamma}\omega)|A|e^{i(\omega t-\theta)} \tag{2.19}$$

Here A_0 and A are the base (drive) amplitude and the tip amplitude respectively. k_c is the cantilever stiffness and ω is the drive frequency. $\bar{k}$ and $\bar{\gamma}$ are stiffness and friction coefficient of the material beneath the tip. And θ is the phase lag between the tip and the base.

$$k_c(A_0 - |A|e^{-i\theta}) = (\bar{k} + i\bar{\gamma}\omega)|A|e^{-i\theta}$$

$$k_c(A_0 e^{i\theta} - |A|) = (\bar{k} + i\bar{\gamma}\omega)|A|$$

$$k_c A_0 \cos\theta + ik_c \sin\theta - k_c|A| = \bar{k}|A| + i|A|\bar{\gamma}\omega$$

comparing real and imaginary components gives us

$$\bar{k} = k_c\Big(\frac{A_0}{|A|}\cos\theta - 1\Big) \tag{2.20}$$

$$\bar{\gamma} = \frac{k_c A_0}{|A|\omega}\sin\theta \tag{2.21}$$

Which is the same as equations 15 and 16. With these equations the sample properties can be quantified easily, the tip amplitude A and phase lag θ are measured.

To operate at off-resonance, stiff cantilevers, more than an order of magnitude higher than what are typically used in constant velocity experiments are required.

2.8 ALTERNATE CONTINUOUS BEAM MODEL.

In the previous model continuous beam model, the interaction force has been introduced into the differential equation with the help of a delta function. Recently there has been a model which incorporates the forces as boundary values to the solution of the differential equations [13]. It has been argued that these conditions alter and affect the dynamics in a non-trivial way when protein is tethered to the tip, particularly in a viscous medium. In this section, the model will be briefly discussed, with some emphasis on the altered boundary conditions.

$$\tilde{\rho}\tilde{S}\frac{\partial^2 w(x,t)}{\partial^2 t} + \gamma_c \frac{\partial w(x,t)}{\partial t} + EI\frac{\partial^4 w(x,t)}{\partial^4 x} = 0 \tag{2.22}$$

Here, x is in the direction of the length with it clamped at $x = 0$ and free at $x = L$. $w(x,t)$ is the displacement perpendicular to the length of the cantilever at position x and time t. $\tilde{\rho}\tilde{S} = \rho + m_a$ is the hydrodynamic added mass where ρ is the mass density of the cantilever material, $S(= bh)$ is the area of the cantilever cross-section perpendicular to its length, b and h are width and thickness of the cantilever respectively, γ_c is the cantilever drag coefficient per unit length, E is the Young's modulus and $= I(bh/12)$ is the second area moment.

If one assumes the solution of the differential equation of the form $W(x,t) = w(x)\exp i\omega t$ and substitutes into the differential equation

$$\tilde{\rho}\tilde{S}\omega^2 - i\gamma_c\omega = EIk^4 \tag{2.23}$$

Using this the following relation can be written down

$$kL = \left[\frac{\tilde{\rho}\tilde{S}\omega^2 L - i\gamma_c\omega L}{k_c}\right]^{\frac{1}{4}} = h \tag{2.24}$$

When the cantilever is driven at off-resonance, the parameter $h << 1$. Further, if the interaction stiffness is small compared to the cantilever stiffness. The following parameter can be written down

$$\frac{3(\bar{k} + i\bar{\gamma}\omega)}{k_c} = g \tag{2.25}$$

Here $g << 1$ for the assumption $k_i << k_c$. These two relations will be used later in the derivation.

Unlike the previous derivation, the forcing and interaction terms here are not included in the differential equation. In this model, the boundary conditions for a base excited cantilever with a linear viscoelastic interaction are given by

$$\begin{aligned} w(0) &= A_0 \exp(i\omega t) && \text{displacement of the base} \\ w'(0) &= 0 && \text{slope at the base} \\ w''(L) &= 0 && \text{force one the tip} \\ EIw'''(L) &= (\bar{k} + i\bar{\gamma}\omega)y(L) && \text{torque on the tip} \end{aligned}$$

The boundary conditions for a tip excited cantilever with a linear viscoelastic interaction are given by

$$\begin{aligned} w(0) &= 0 && \text{displacement of the base} \\ w'(0) &= 0 && \text{slope at the base} \\ w''(L) &= 0 && \text{torque one the tip} \\ EIw'''(L) &= (\bar{k} + i\bar{\gamma}\omega)w(L) - F_0 \exp(i\omega t) && \text{force on the tip} \end{aligned}$$

The general solution of the space part of the partial differential equation is given by

$$w(x) = a \sin kx + b \cos kx + c \sinh kx + d \cosh kx \tag{2.26}$$

The four constants in the general solution can be eliminated using the four boundary conditions for each of the base excited and tip excited case. Thereafter, expanding the solution using Taylor series around small values of the parameters h and g one can get relations for stiffness and damping of the sample.

Although, this derivation accounts for the altered boundary conditions as the experiment progresses, the assumption $g << 1$ and $h << 1$ makes it consistent with the values obtained from the point mass model. We have seen that if the experiments are performed in the proper off-resonance condition and the cantilever stiffness is high as compared to the sample stiffness, both models give the same results [7].

2.8.1 Artifact Free Measurements at Off-resonance

In order to have artifact free measurements, it becomes essential to perform experiments in the off-resonance regime. We will now discuss the reasoning behind this argument graphically (figure 2.5). For a cantilever with low quality factors and stiffness, the frequency response would look like figure 2.5(a). If one drives the cantilever near the resonance frequency, the cantilever already has a phase lag and some amplitude. In figure 2.5(b) an interaction has been incorporated into the dynamics such that it only has a stiffness. This causes an increase in the resonance frequency of the cantilever, and the resonance curve shifts to a higher frequency. The amplitude drops to a lower value, due to the increased stiffness of the system. However, the phase lag reduces to a lower value. This variation in phase lag due to change variation in stiffness, can result in the phase lag signal being misinterpreted as variation in damping. When the sample also contains dissipative properties, it becomes further challenging to separate the phase lag due to sample's damping and the change in phase due to variation in stiffness. In principle, if the cantilever strictly follows a damped harmonic model, one can separate these contributions. However, it is seldom the case since oscillating the cantilever near a resonance peak results in various contributions to the dynamics like fluid borne excitation , spurious peaks in frequency spectrum, and effect of sample cell geometry[9, 10]. Therefore, it becomes extremely difficult to predict how the phase will behave during the experiment when the cantilever is oscillated near resonance.

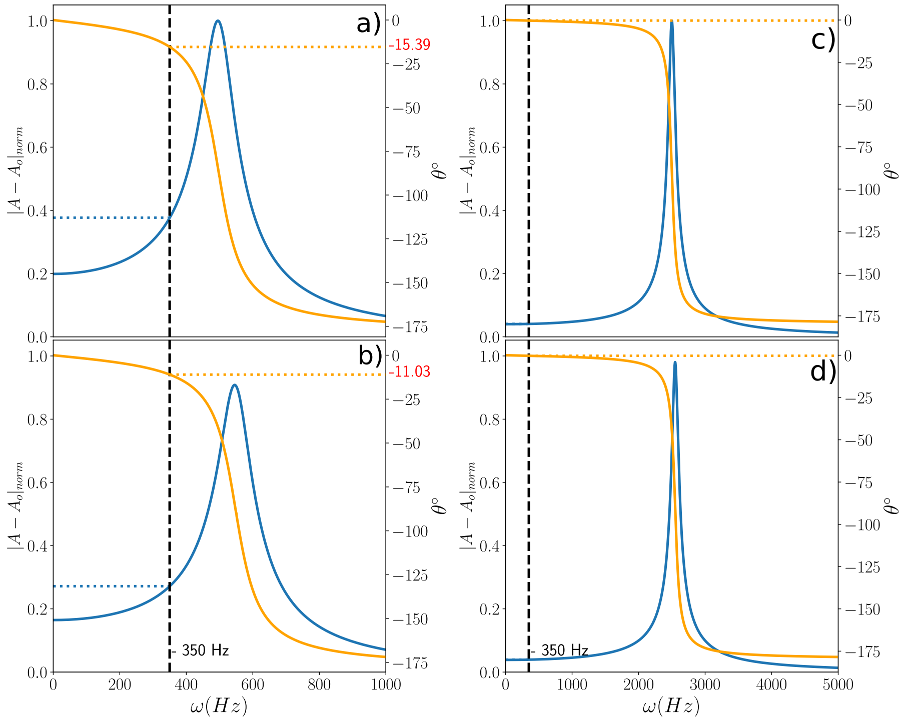

Figure 2.5: Plots of the solution of the damped harmonic model (Point mass model). a) Cantilever with low resonance and quality factor b) Same as a) apart from an added interaction stiffness to the cantilever stiffness. c) Response of a cantilever with high resonance and quality factor. d) Same as c) apart from an interaction stiffness being added to the cantilever stiffness.

One can circumvent these modelling issues if one uses a cantilever with high resonance and stiffness and better quality factor. The resonance curve for such a cantilever is shown in figure 4.5(c). Although, the cantilever is oscillated at the same frequency as the previous case, the drive frequency is way below its resonance. The amplitude gets reduced due the cantilever having higher stiffness, but the phase lag in this case is close to zero. In the figure 4.5(d) an interaction has been introduced into the dynamics, such that it increases the resonance frequency like the previous case. In this case the phase lag does not vary since initially it was already at zero. Now any variation in the phase lag of the tip, will be due to the result of the sample having dissipative properties. In this way it becomes extremely straightforward to quantify sample stiffness and friction in an artefact free manner.

It is essential to note that one cannot perform off-resonance operation with a cantilever whose response is similar to figure 4.5(a), because even at drive frequencies lower than that are shown in figure 4.5(a), there is no flat regime in the phase response, any stiffness change can still bring about a change in phase. Furthermore, lower frequencies also make it difficult to work with in pulling experiments since the quasi-static pulling speed also needs to be reduced to compensate for the slow drive. Low pulling speed hinders stable measurements due to drift issues. It is only when stiff cantilevers with high resonance frequencies are used one can achieve this off-resonance operation. Secondly, equations 20 and 21 work with an implicit assumption that the tip amplitude is small enough so that it probes linear response of the material beneath it. Since this response varies between different types of materials held beneath the tip, one needs to be careful about employing large amplitudes to achieve better signal-to-noise ratio.

2.9 SERIES/PARALLEL ARRANGEMENTS:

When the cantilever is driven at resonance, either from the base or the tip, the amplitude at the tip is large compared to the drive. When a molecule is attached to the tip both will have the extensions over the oscillation period. This makes the two elements be in parallel arrangement. However, when the cantilever is oscillated at the off-resonance regime, the arrangement is decided according to the drive. The two case are elucidated in detail below.

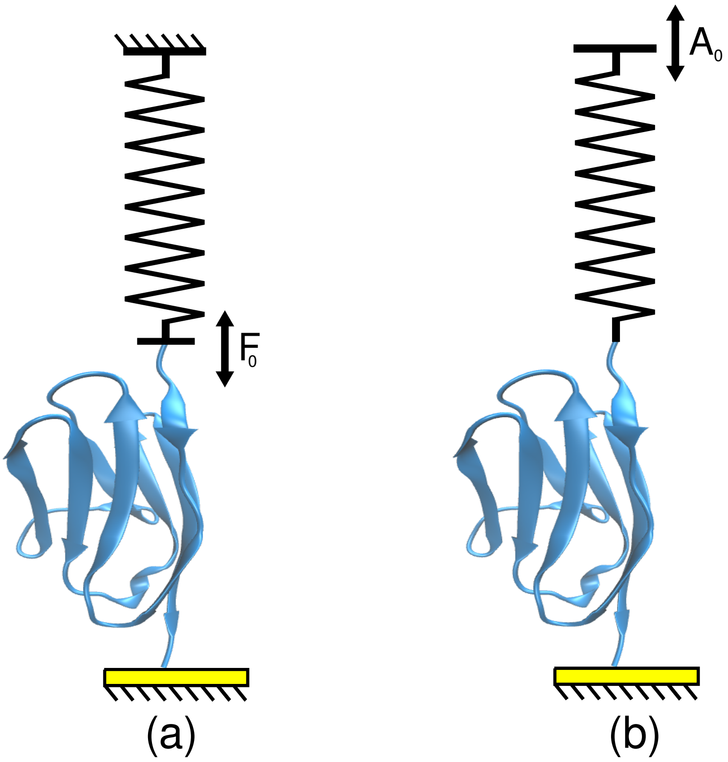

Figure 2.6: a) Parallel arrangement for the tip excited case where an oscillating force is applied on the magnetic tip of the cantilever via an alternating magnetic field. The bending in the cantilever and protein is the same. b) Series arrangement for the base excited case, where the base is excited with an A_0 amplitude. The extension in the protein and the bending in the cantilever is inversely proportional to their respective stiffness whereas the force is same.

2.9.1 PARALLEL (TIP EXCITATION):

In tip excitation one coats the tip of the cantilever with a magnetic material - usually cobalt . Forcing $F_0 \exp(i\omega t)$ is provided to the tip by an alternating magnetic field via a solenoid. With this arrangement the tip applies a force on the sample and the change in phase and the reduction in amplitude is measured. When providing forcing with this technique the tip and sample are in parallel with each other since their deformations are equal. As mentioned earlier, stiff cantilevers are required to obtain a clear off-resonance regime. To have a detectable signal when measuring bending, relatively large amplitudes are required and to get these large amplitudes the forcing needs to be large in turn. Numerous studies have been done to measure friction and stiffness of molecular layers using this excitation scheme, however the stiffness of the layers is comparable to the cantilever and therefore leads to detectable change in amplitudes.

For instance, to get an amplitude of 1 nm, for a cantilever with stiffness 1N/m, F_0 needs to 1000pN. For proteins which usually unfold around the 200pN this can be a very high force. Furthermore, since the cantilever and the molecule are in parallel, their stiffness add to give the combined stiffness. This increase leads to reduction in the amplitude from its initial value when no molecule is attached. Typically for single protein experiments, the maximum stiffness value measured before the protein unfolds is $\sim$ 0.01N/m, this would lead to 1% reduction in amplitude for a cantilever with stiffness 1 N/m. This makes it unsuitable for viscoelasticity measurements on proteins. A way around this is to drive the cantilever from the base.

2.9.2 Series (Base Excitation)

In this excitation scheme the base of the cantilever is excited using a dither piezo. When the excitation frequency is in the off-resonance regime the inertial and damping forces on the cantilever are close to zero. Therefore, the response of the cantilever can be approximated by its static response. Therefore when there is no molecule attached to the tip, the base amplitude and the tip amplitude of the cantilever are same, implying no bending in the cantilever. However, in the presence of a molecule, the bending in the lever is non zero. The drive amplitude, ie, the amplitude with which the base is oscillated, gets divided into the two elements - the molecule and the cantilever. And the ratio of the amplitudes in each element is inversely proportional to the ratio of their stiffness, therefore the molecule and the cantilever are in series arrangement when base excitation is implemented.

2.10 NEED FOR DISPLACEMENT DETECTION SCHEME

The force sensitivity of cantilevers suitable for off-resonance operation is low, due to their high stiffness. If one measures cantilever bending during these experiments, the signal to noise ratio becomes extremely low. This fact is explained in the figure 2.7. The conventional AFMs that use optical beam bending technique to measure cantilever deflections measure the quantity $A_0 - A$, which is the bending.

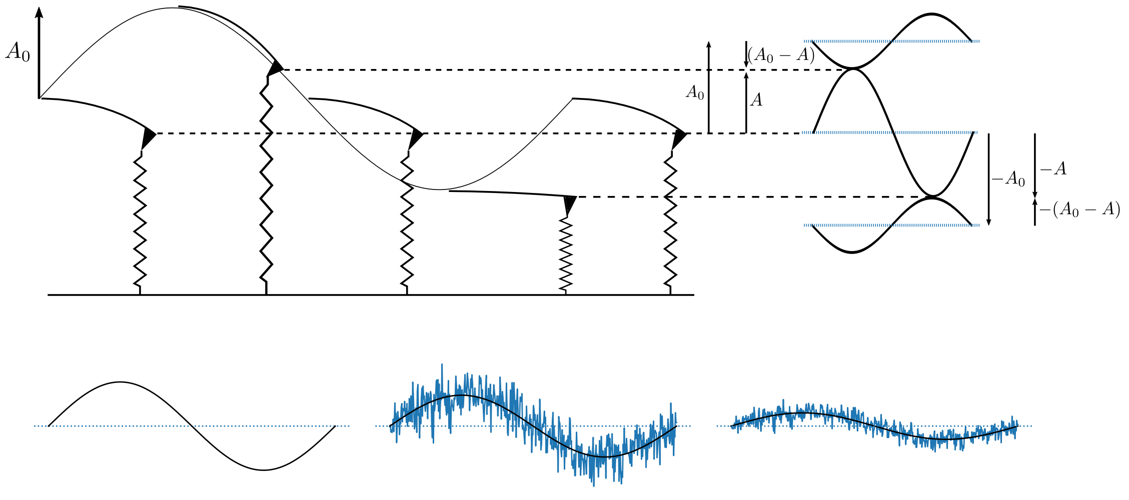

A_0 A:Interferometer based dectection $(A_0 - A)$:Conventional Detection

Figure 2.7: a) and c) The difference in tip displacement signal (A) and the cantilever bending signal($A_0 - A$). Interferometer based detection measures tip displacements whereas the deflection detection scheme measures the bending. For stiff cantilevers(0.5 to 1 N/m), the bending is extremely small and difficult to detect. Furthermore, A also represents the amplitude of extension in the molecule over the oscillation, which is directly measured by the interferometer.

To sum it up, if one needs to perform artifact free measurement of viscoelasticity, off-resonance driving of the cantilever is required. This in turn puts a constraint on the cantilever to have high stiffness and smaller length to achieve high resonance and high quality factors. For experiments on proteins to keep the forcing amplitude low, base excitation needs to implemented in which the sample and cantilever are in series. Due to this the amplitude across the cantilever becomes small due to it having much larger stiffness as compared to the protein. This results in very low signal to noise ratio, which cannot be measured by the conventional detection scheme.

To overcome this, the displacement of the tip needs to be measured directly. To achieve this an interferometer based detection scheme needs to be implemented, which we will be discussing in the next chapter.

Bibliography

[1] Gerhard Meyer and Nabil M Amer. Novel optical approach to atomic force microscopy. *Applied physics letters*, 53(12):1045–1047, 1988.

[2] SLOJVPKM Alexander, Louis Hellemans, Othmar Marti, Jason Schneir, Virgil Elings, Paul K Hansma, Matt Longmire, and John Gurley. An atomic-resolution atomic-force microscope implemented using an optical lever. *Journal of applied physics*, 65(1):164–167, 1989.

[3] Yves Martin, Clayton C Williams, and H Kumar Wickramasinghe. Atomic force microscope–force mapping and profiling on a sub 100-å scale. *Journal of applied Physics*, 61(10):4723–4729, 1987.

[4] H-J Butt and Manfred Jaschke. Calculation of thermal noise in atomic force microscopy. *Nanotechnology*, 6(1):1, 1995.

[5] Edward B Magrab. *Vibrations of elastic systems: With applications to MEMS and NEMS*, volume 184. Springer Science & Business Media, 2012.

[6] Jose R Lozano and Ricardo Garcia. Theory of phase spectroscopy in bimodal atomic force microscopy. *Physical Review B*, 79(1):014110, 2009.

[7] Shatruhan Singh Rajput, Surya Pratap S Deopa, VJ Ajith, Sukrut C Kamerkar, and Shivprasad Patil. Validity of point-mass model in off-resonance dynamic atomic force microscopy. *Nanotechnology*, 32(40):405702, 2021.

[8] SJ O'Shea. Comment on "oscillatory dissipation of a simple confined liquid". *Physical review letters*, 97(17):179601, 2006.

[9] Daniel Kiracofe and Arvind Raman. Quantitative force and dissipation measurements in liquids using piezo-excited atomic force microscopy: a unifying theory. *Nanotechnology*, 22(48):485502, 2011.

[10] Xin Xu and Arvind Raman. Comparative dynamics of magnetically, acoustically, and brownian motion driven microcantilevers in liquids. *Journal of Applied Physics*, 102(3):034303, 2007.

[11] Ernst-Ludwig Florin, Manfred Radmacher, Bernhard Fleck, and Hermann E Gaub. Atomic force microscope with magnetic force modulation. *Review of Scientific Instruments*, 65(3):639–643, 1994.

[12] N Umeda, S Ishizaki, and H Uwai. Scanning attractive force microscope using photothermal vibration. *Journal of Vacuum Science & Technology B: Microelectronics and Nanometer Structures Processing, Measurement, and Phenomena*, 9(2):1318–1322, 1991.

[13] Fabrizio Benedetti, Yulia Gazizova, Andrzej J Kulik, Piotr E Marszalek, Dmitry V Klinov, Giovanni Dietler, and Sergey K Sekatskii. Can dissipative properties of single molecules be extracted from a force spectroscopy experiment? *Biophysical journal*, 111(6):1163–1172, 2016.

CHAPTER

THREE

INSTRUMENTATION

For off-resonance operation one needs to have a clear region in the frequency response of the cantilever, where the inertial and velocity dependent forces on the lever can be neglected. To achieve this the resonance frequency of the cantilever need to high $25 - 50$ kHz with high quality factors as well. These specifications decrease the lever's sensitivity to force. The convention detection scheme, the optical beam deflection scheme measures bending in the cantilever. Since bending is proportional to the difference between the base and the tip displacements, it is extremely small in off-resonance operation. One needs to measure displacements directly.

It is possible to measure tip-displacement directly with an interferometer. The use of an interferometer to detect the tip amplitude was first used for UHV conditions by Rugar et. al.[1]. It enjoyed success in early years but did not develop into a routinely used method for dynamic AFM since it is challenging to position the fibre precisely over the cantilever and align it so that the sensitivity is maximized. As a result most commercially available AFMs do not provide inteferometer-based detection schemes.

With enhanced sensitivity compared to the deflection detection type measurement scheme, it is possible to perform off-resonance operation with stiff cantilevers. Another advantage of this scheme, compared to deflection detection is that it is able to measure extension produced in the molecule directly by monitoring the tip displacement and not the bending in the cantilever. Using interferometer based small amplitude Atomic Force Microscope it has been possible to measure dissipation processes between atoms [2]. It has also measured linear nanomechanical properties of molecular layers of liquids confined between the tip and flat substrate [3, 4].

It should be noted that while using dynamic AFM to measure protein's viscoelastic response, the purpose is not only to allow the use of phase sensitive methods for measurement with better sensitivity. One is interested in measuring stress, strain and their phase relationship with each other in a quantitative manner.

In this chapter we will be going through the details of the instrumentation required to implement displacement detection on an AFM cantilever.

3.1 Overview

There are two aspects of the experiment using performing Dynamic AFM Force Spectroscopy. First, as the separation z between the cantilever base and the substrate is increased, force F builds up on the protein that is attached between the cantilever tip and the surface. Eventually, one of the protein domains unfolds due to the force. This part is similar to the constant velocity pulling experiments done routinely.

The other aspect involves dynamic measurements where base of the cantilever is oscillated with a constant frequency and amplitude. The substrate retraction is halted at each separation z for a certain duration. During this period the dynamic response of the protein under force F (due to the cantilever base and surface separation z) is obtained by recording the amplitude and phase of the cantilever tip.

A fiber with semi-mirror at its end is aligned perpendicular to a cantilever using a five-axis fibre nanopositioner (figure 3.1). The mirror and the back of the cantilever form a Fabry-Perot etalon. Infrared light(1310 nm) from a laser diode is guided into a 2×2 splitter. 50 % laser light goes to the etalon. The resulting interference signal, due to primary beam entering into the etalon and its interference with multiple

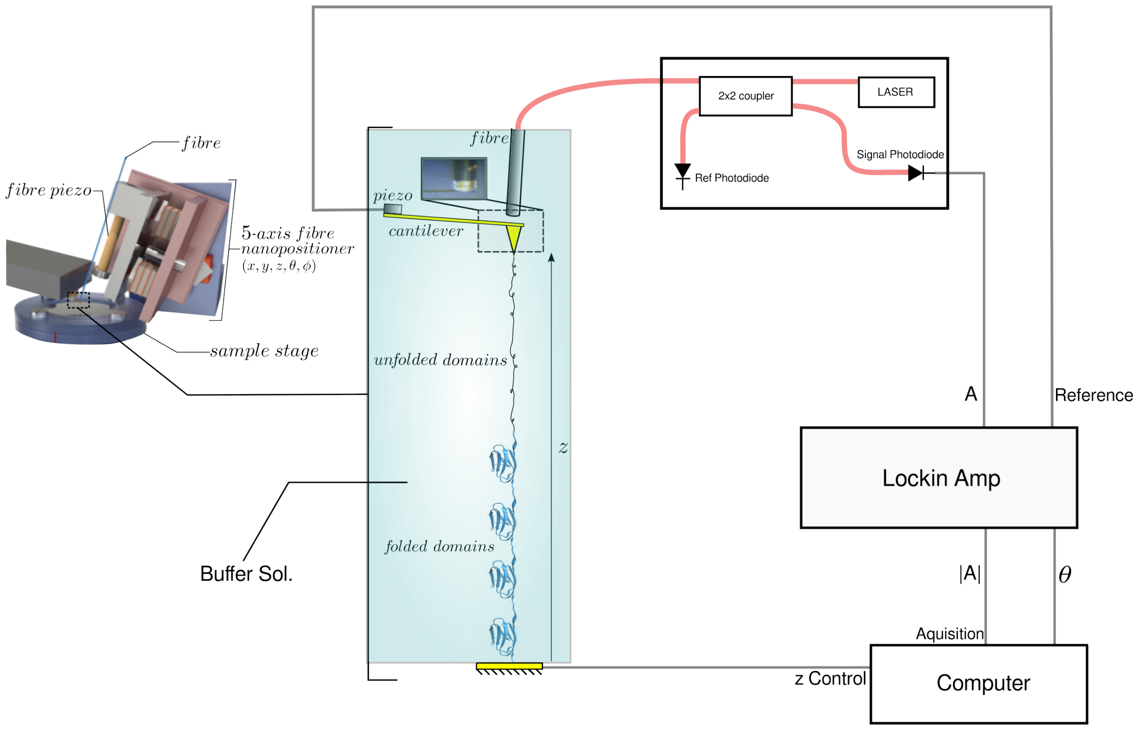
fibre
fibre piezo
5-axis fibre nanopositioner
(x, y, z, θ, φ)
sample stage
fibre
piezo
cantilever
unfolded domains
z
folded domains
Buffer Sol.
2x2 coupler
LASER
Ref Photodiode
Signal Photodiode
A
Reference
Lockin Amp
|A|
θ
Aquisition
z Control
Computer

Figure 3.1: The experimental setup used in the experiments. It includes a nanopositioner that is used to align the fibre at the back of the cantilever. The interferometer setup used to split the laser beam one going to a reference diode and the other to the fibre. The lockin amplifier is used to extract the amplitude A and the phase lag θ. The separation between the cantilever tip and substrate is controlled using the computer. A feedback is implemented on the amplitude of cantilever to control the z separation while approach

reflections between mirror and cantilever's back surface is guided using the same splitter onto a photodiode. The current in the photodiode is extremely sensitive to fibre cantilever distance. We typically obtain sensitivity 300-500 mV/nm and measure cantilever displacement with precision of less than an angstrom.

The experiments are performed much in the same way as constant velocity pulling using static mode. The only difference is the base is oscillated at off-resonance frequencies and the tip and substrate are pulled away from each other quasi-statically. Repeats of 8 domains of Immunoglobulin (IgG) of titin $(\text{I-27})_8$, are sparsely coated on a gold cover-slip immersed in PBS buffer. 100 μl of I-27_8 protein solution with a concentration of 10mg/ml in PBS (pH 7.4) is drop cast onto a gold coated cover-slip mounted in a fluid cell and excess protein is washed away after incubation. The cantilever is lowered into the solution and the fiber is positioned on the back of the cantilever above the tip. The semi-mirror on the fibre end is aligned parallel to the back-surface of cantilever. The cantilever base is oscillated with amplitude A_0 at a frequency ω, which is far below resonance. The amplitude A and phase lag θ of the protein-attached tip is recorded using the interferometer, as the mean separation between the base and substrate(z) is varied. The amplitude, A and phase θ versus mean separation z is used to calculate the stiffness and the friction coefficient.

3.2 Phase Sensitive Detection

One of the most important aspects of the experiment is the ability to measure the response of the cantilever at the drive frequency as the protein is pulled. The lockin amplifier is the perfect candidate for performing such experiments, since it can provide us with both the amplitude and the phase lag necessary for viscoelasticity measurements.

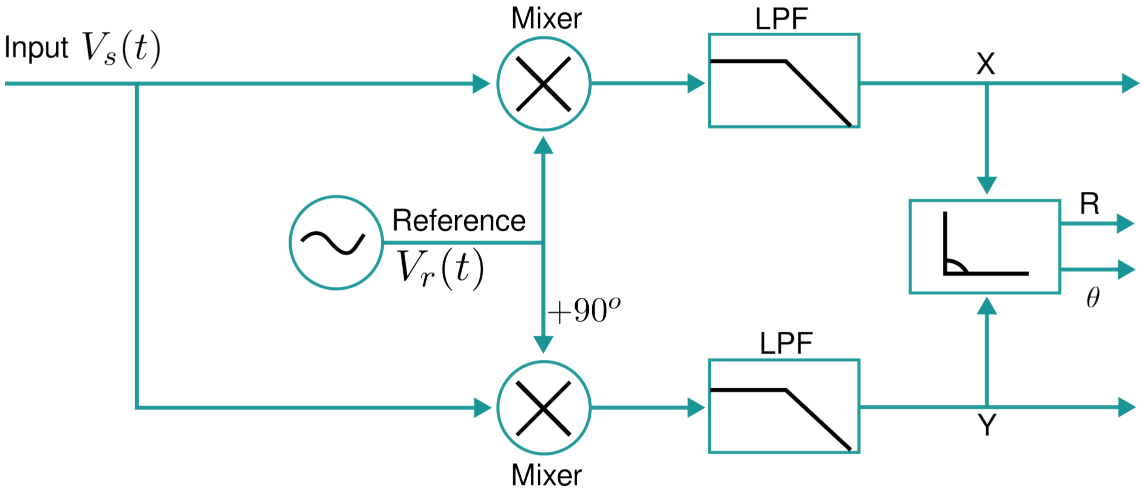

Figure 3.2: Schematic showing the signal chain followed in a lockin amplifier. The mixers multiply the input signals with reference and 90^o shifted reference signal. LPFs are low pass filters, which usually have adjustable roll off frequencies.

The lockin amplifier is used to extract signal of known frequency from a noisy background. Firstly, the signal input signal $V_s(t)$ is multiplied with the reference signal $V_r(t)$.

The input signal and the reference signal can be expressed as

$$V_s(t) = V_s \sin(\omega_s t + \theta_s) \tag{3.1}$$

$$V_r(t) = V_r \sin(\omega_r t + \theta_r) \tag{3.2}$$

The two signals are then multiplied to get the mixed signal, which can be mathematically expressed as

$$Z(t) = V_r V_s \sin(\omega_s t - \theta_r) \sin(\omega_r t + \theta_r) \tag{3.3}$$

$$= \frac{1}{2} V_r V_s \cos((\omega_r - \omega_s)t + \theta_s - \theta_r) - \frac{1}{2} V_r V_s \cos((\omega_r + \omega_s)t + \theta_s + \theta_r) \tag{3.4}$$

The output signal is a superposition of two signals with different frequencies. The signal with high frequency $\omega_r + \omega_s$ is filtered out using a low pass filter after which we are left with the signal only with lower frequency $\omega_r - \omega_s$.

$$Z(t) = \frac{1}{2} V_r V_s \cos((\omega_r - \omega_s)t + \theta_s - \theta_r) \tag{3.5}$$

If $\omega_r = \omega_s$ the filtered signal becomes

$$Z(t) = \frac{1}{2} V_r V_s \cos(\theta_s - \theta_r) \tag{3.6}$$

$$\sim V_s \cos(\theta) \tag{3.7}$$

This is a signal that is proportional to the input signal amplitude and the phase lag $\theta = \theta_s - \theta_r$. If the reference phase lag θ_r is equal to the signal phase lag θ_r the $\cos(\theta_s - \theta_r)$ term becomes 1.

To measure both the amplitude and the phase lag of the input signal with respect to the reference frequency, two mixers are used. One mixer multiplies the reference signal directly giving $Z(t)$ as output and the other multiplies a 90^o shifted reference signal.

For the phase shifted reference signal the output of the mixer can be expressed as

$$Z_2(t) = \frac{1}{2} V_r V_s \cos((\omega_r - \omega_s)t + \theta_s - \theta_r - 90^o) \tag{3.8}$$

If $\omega_r = \omega_s$ the filtered signal becomes

$$Z_2(t) = \frac{1}{2} V_r V_s \cos\left(\theta_s - \theta_r - 90^o\right) \tag{3.9}$$

$$\sim V_s \sin(\theta) \tag{3.10}$$

The two outputs can be called X and Y that corresponding to the outputs that are proportional to the cos and sin respectively.

$$X = V_s \cos\theta \qquad\qquad Y = V_s \sin\theta \tag{3.11}$$

The magnitude of the signal along with its phase lag from the reference signal can be expressed as

$$A = \sqrt{X^2 + Y^2} \tag{3.12}$$

$$\theta = \arctan\frac{Y}{X} \tag{3.13}$$

In our case, the reference signal is the drive provided to the dither piezo. The lockin amplifier is able to extract from a noisy signal the magnitude of the cantilever oscillatory displacement at the reference frequency and also its phase lag with respect to the reference signal.

3.3 SEMI MIRROR

The fibre being used in the instrument is single mode optical fibre. The inner diameter of the fibre which is the core is 9 μm and the outer diameter which is the cladding is $125\mu m$. The cleaved end of the fibre acts as the semi mirror as shown in figure 3.3.

However, with a bare cleaved end the fibre reflectivity is only 3-5%. To achieve higher reflectivity, so that more light can be reflected back into the fibre to achieve more sensitivity, one needs to coat a reflecting surface on the cleaved end of the fibre [5]. This is done by dipping the cleaved end of the fibre into a metallic organic compound of Ti02 and Xylene. The end is then brought into a butane flame, the organic solvent evaporates and a uniform layer of Ti02 is left on the cleaved end [6]. With this method one can achieve a reflectivity of 20-25%.

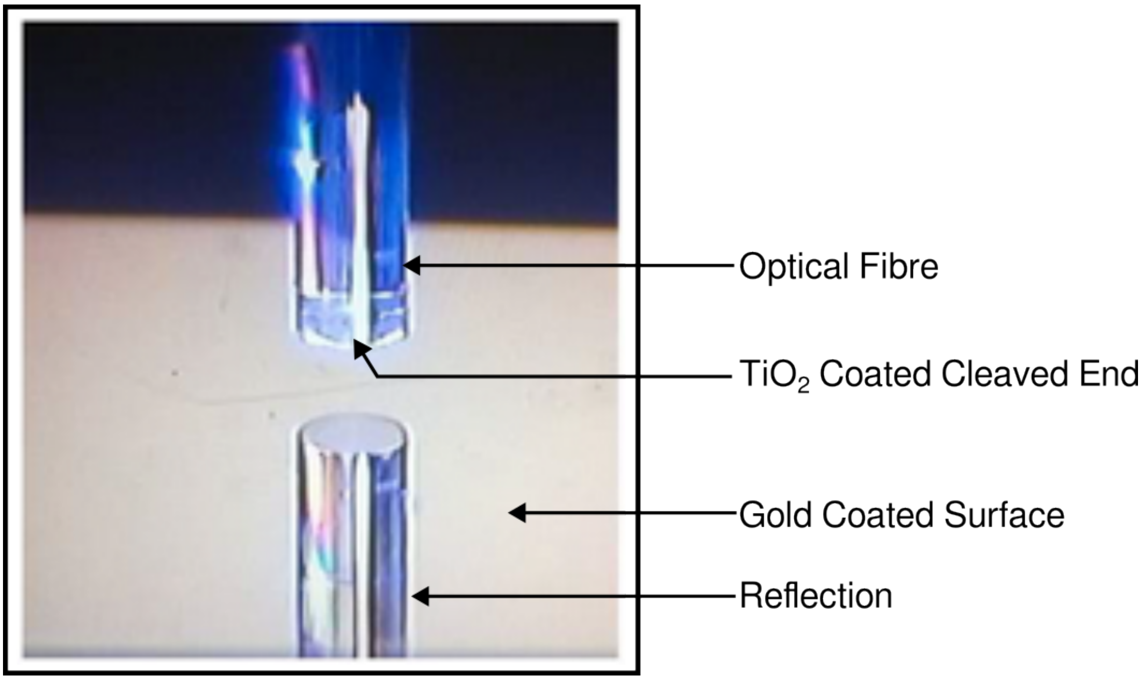

Figure 3.3: The fibre that needs to be aligned at the back of the cantilever. This photo shows the cleaved end of the fibre coated with $Ti0_2$, that is visible in its reflection on the gold coated surface.

3.4 Nano Positioner

The first task at hand is to bring the core of the fibre on top of the cantilever's tip end. This requires control over the (x,y,z) degrees of freedom of the fibre end. Secondly, the mirror at the end of the fibre also needs to be parallel to the end of the cantilever, requiring control over the angular degrees of freedom (θ, ϕ). Since the diameter of the fibre core is $9\mu m$ and the width of the cantilever is $35\mu m$, fine control of position and orientation of the fibre end is required. This is done using the nanopositioner.

It contains two plates, first and second, perpendicular to each other as shown in the figure 3.5. The second plate houses a tube piezo to which the fibre is attached. This plate can slide with respect to the stack of piezos fixed on the first plate. This sliding motion is done using the inertial sliding mechanism. The second plate is also kept on another stack of piezos and can perform similar sliding motion. Each stack

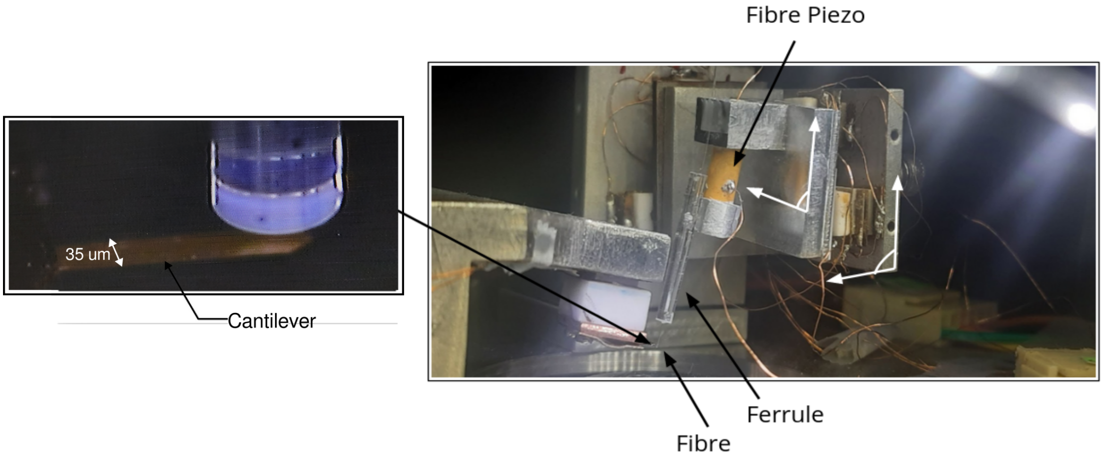

Figure 3.4: The left image showing the fibre aligned at the back of the cantilever. The width of the cantilever is 35 μm and the length is 130 μm. The right image shows the nano positioner being utilised to perform the alignment. The arrows in white depict the axis of motion and rotation, for the two plates on which the fibre is attached

contain three piezo with their shear axis along the three directions as depicted in the figure 3.5 a). If the input to the stack is such that the piezos along the same direction from each stack get activated, it results in a translational motion of the fibre. If piezos on the lower stacks move along one direction and the top stack piezo movies in the opposite direction, it results in a rotational motion of the fibre. Using this technique one can achieve fine control of the fibre end along the (x,y,z) and (θ, ϕ).

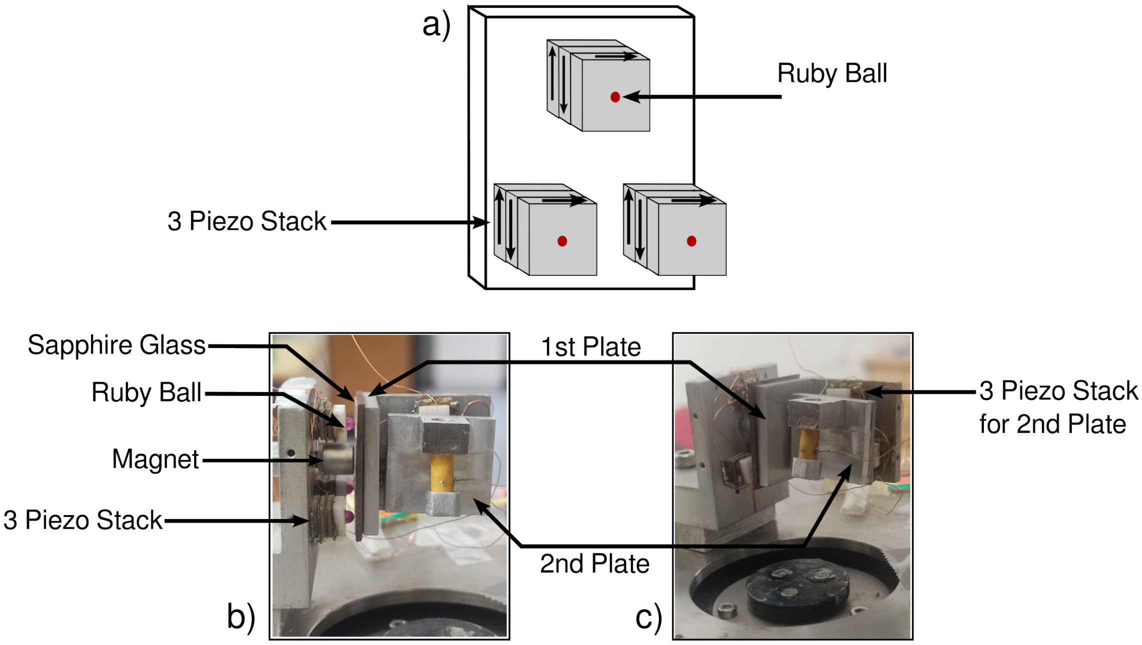

Figure 3.5: a) The stack of piezos on which a sliding plate is kep. For moving the plate in a translational way, piezo having their shear axis along the desired direction are activated with the correct polarity. For rotational motion, the top plate and the bottom two stacks are moved in the opposite direction. For example to make a plate rotate clockwise, the outermost piezo of the top stack with shear axis to the right will be activated and the top piezo of the bottom two stacks will be biased with the reverse polarity as compared to the top piezo. b) Front view of the nanopositioner. c) Side view of the nanopositioner.

3.5 FIBRE ALIGNMENT

Once the fibre end is aligned parallel to the back of the cantilever, optimum separation between the two mirrors is required for maximum sensitivity. The current on the photo diode is proportional to the intensity of light incident on it. If the separation between the two mirrors is such that the light interferes destructively or constructively, light or dark fringes are formed for that separation. At these separations the change in current due to change in separation between the two mirrors is minimum. This implies that the change in power incident on the photodiode has minimal change with respect to the change in separation.

Our task is to measure the change in separation between the two surfaces with maximum sensitivity. For this to be possible, the separation between the two mirrors should be such that it lies on the the point of maximum slope on the power vs separation graph. This is achieved by modulating the separation between the two mirrors. The fibre is attached to a tube piezo which can increase or decrease in length according to the voltage provided to it. Voltage in the form of a triangular wave is given to the fibre, to record the intensity of light for a range of separations. The graph is plotted and the point of maximum slope (quadrature) is determined. The separation is locked at this quadrature point with a feedback on the tube piezo. When the cantilever is driven from the base using a dither piezo, it oscillates the gap between the cantilever and the fibre. As a result, the current intensity on the photodiode also oscillates. This modulation is not compensated for by the tube piezo since the feedback on it is slow for the removal of drifts. The cantilever oscillations just pass through and can be measured. The sensitivity one can achieve with kind of detection scheme is 300-500 nm/mV, which is much higher than that of a conventional AFM. A locking amplifier then can be used to extract this oscillating signal which corresponds to the displacement of the cantilever tip.

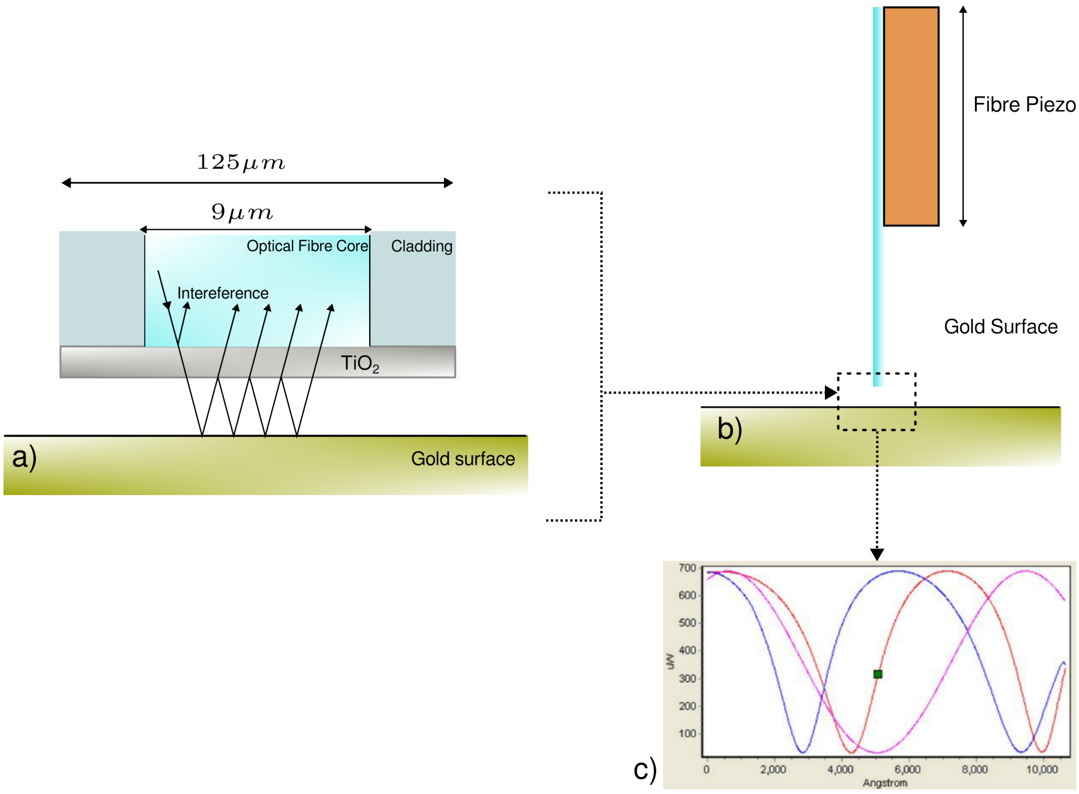
125μm
9μm
Optical Fibre Core
Cladding
Intereference
TiO$_2$
a)
Gold surface
Fibre Piezo
Gold Surface
b)
700
600
500
400
300
200
100
uW
0
2,000
4,000
6,000
8,000
10,000
Angstrom
c)

Figure 3.6: a) Figure showing multiple reflections between a gold coated surface and the Ti0$_2$ coated cleaved end of the fibre. The fibre is parallel to the gold surface which is required for a Fabry Perot Etalon. b) The separation between the two mirrors modulated using the tube piezo. c) The red line signifying the power incident on the photodiode a function of separation between the two mirrors. The blue line is the same pattern, but in the reverse cycle of triangular wave given to the fibre piezo. The intensity in the forward and reverse cycles do not fall on each other due to some hysteris in the movement of the tube piezo. The third line is a cos function of the separation between the two mirror, which can be used as reference for comparing the interference pattern. The square marker on the graph shows the separation of maximum sensitivity on the graph, on which the piezo has to be locked during the experiment.

3.6 Fluid Cell

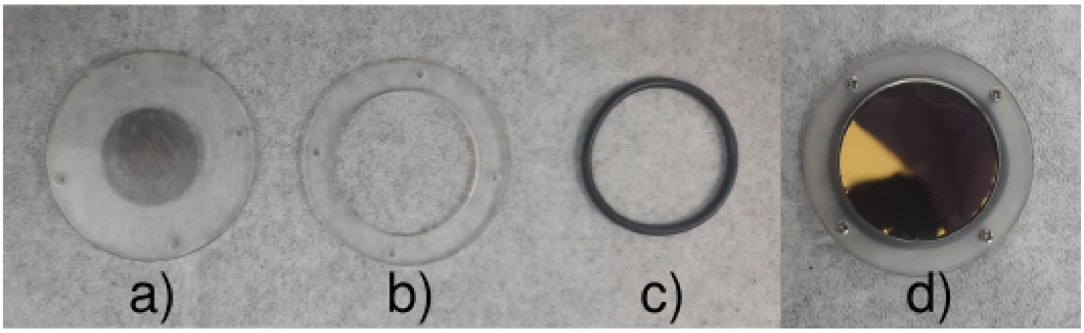

Figure 3.7: a) The lower piece of the fluid cell. Its bottom surface has the a metal disc glued to it, which is used for attaching the cell to the magnets on the sample stage. Also contains four holes for the screws to be inserted. b) The top pieces of the sample, also containing holes for the screws to be inserted. c) Rubber O-ring that gets sandwiched between the the pieces of the sample cell. d) Fluid cell after assembly with a gold coated cover coated loaded onto it.

The gold coated cover slip is placed over the lower piece of the fluid cell (figure 3.7 a), after which the O-ring (figure 3.7 c) is kept on top of it. The upper part of the cell (figure 3.8 b) is then placed on top of the O-ring. The screws are inserted into the holes and tightened. This results in the O-ring getting sandwiched between the two pieces and making a waterproof seal between them. The protein sample can then be dropcasted onto the cover slip.

3.7 Approach & Amplitude Feedback

One aspect of the experiment is to approach the cantilever tip to the surface so that the protein can attach to it. In conventional force spectroscopy, the feedback is on the cantilever bending. In our case, the feedback is on the amplitude of the cantilever tip oscillation much like the tapping mode in AFM imaging. Using the amplitude of the tip as the input to a PI controller one can approach the sample slowly and not press to hard on it. In our setup, the vertical position of the cantilever is fixed, it is the substrate that moves up and down during approach and retract using the sample stage movement setup shown in figure 3.8. The sample stage contains two piezos a hammer piezo and a scanner piezo. The hammer piezo uses inertial sliding mechanism to perform coarse approach and retract movements of the sample stage. The scanner piezo is a quadrant tube piezo, which can be used for fine approach or retract by giving same voltage to all the four quadrants.

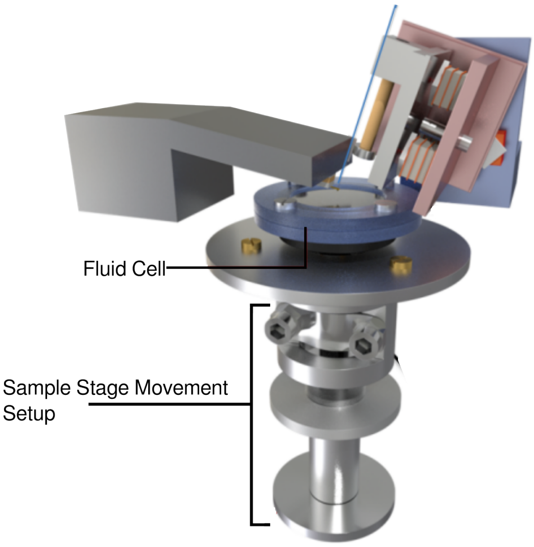

Figure 3.8: Figure depicting the sample stage, containing the hammer and the scanner piezo

As the cantilever approaches the surface, its tip amplitude decreases. A set point amplitude is given to the controller, and the separation between the cantilever and the substrate is decreased by raising the sample stage until the amplitude of the tip is equal to the set point amplitude. The controller is implemented with an analog circuit and the amplitude measured using the lockin amplifier is used as an input.

3.8 GRID

As the cantilever approaches the surface, the possibility of a protein being under the tip and attaching to it is low. Success rate of a single protein attaching to the tip and unfolding as the tip is retracted is around 5%. So one needs to repeat this approach-retract cycle multiple number of times, on different locations of the substrate. It is achieved by using the scanner piezo on which the fluid cell is attached. As mentioned earlier, this scanner piezo is a quadrant piezo having four inputs. With same input to all the quadrants the sample stage moves up or down. However, by giving different voltages to the four quadrant one can move the substrate in x y plane. After each approach retract cycle the substrate position is changed in the x y plane.

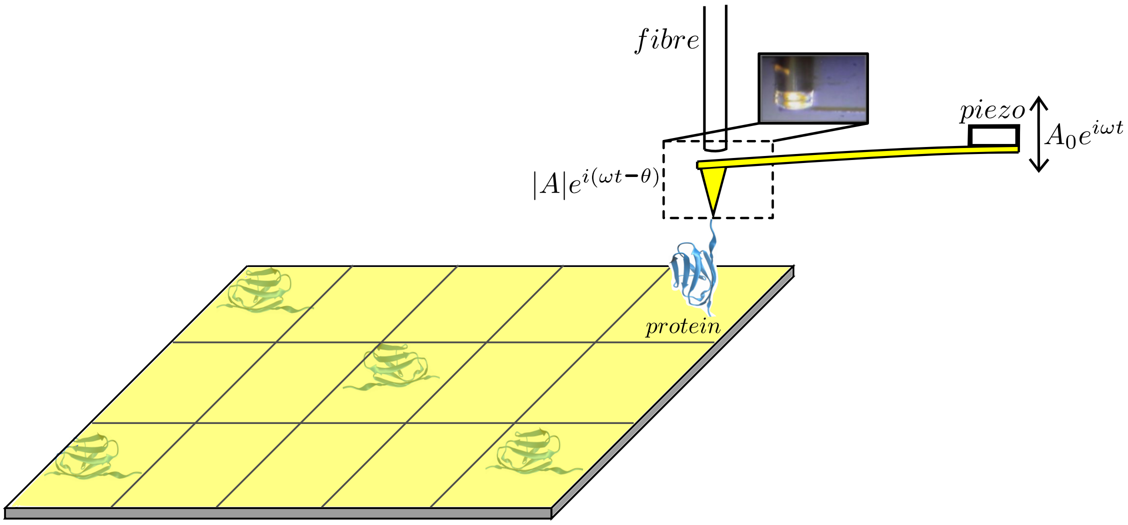

Figure 3.9: Figure depicting an experiment where the cantilever is fishing for the proteins. The proteins here are sparsely present on the surface. After each approach-retract cycle, the position of the substrate is changed to pick up new protein to unfold with the cantilever.

3.9 METHODS

We will conclude by going through the process of performing the experiments with respect to the instrumental details discussed in the previous sections.

3.9.1 SAMPLE PREPARATION

The I27 octamer was cloned in the pET-23a vector and was transformed in BL21(DE3) and it was induced at 0.6 OD with 1 mM IPTG for 6 hours at 37 °C. The pelleted cells were stored at 40 °C. Thereafter, the frozen bacterial pellet was resuspended in PBS pH 7.4 supplemented with protease inhibitor cocktail (Roche) for purification. They were then lysed by sonication in an ice water bath after resuspension. The lysate was spun at 18500 g for 30 min. The resulting supernatant was incubated with His-Pur cobalt resin for 1 h at 4 °C. To get rid of non-specifically bound proteins, the supernatant was poured into the PD-10 column, and the resin was washed with 150 ml of PBS pH 7.4. PBS with 250 mM imidazole was used for eluting the protein. Purified protein fractions were pooled and dialyzed overnight against 1XPBS pH 7.4 buffer to remove imidazole.

A freshly gold coated cover slip using thermal vapour deposition is loaded onto the fluid cell. The protein solution (100 μl, 10mg/ml) is dropcasted on the coverslip and allowed to incubate for 20 minutes. Thereafter, the excess proteins that are not adsorbed on the cover slip are washed away with PBS solution. And filled with 600ul of buffer solution.

3.9.2 CANTILEVERS

Cantilevers used in the experiments are from Mikromasch USA, model HQ:NSC36/Cr-Au-C. The resonance of the cantilever is 65kHz and 24kHz in air and liquid respectively. The cantilevers are gold coated from both sides with length 130μm , width 32μm , thickness 1μm. The stiffness of these cantilevers are 0.6 - 1 N/m.

3.9.3 EXPERIMENT

The cantilever is loaded onto the holder, and the fibre is brought to the back of the cantilever with the help of the nanopositioner. The fibre piezo modulates the separation between the fibre end and cantilever back producing the power vs separation graph shown in figure 3.6(c). Fine changes are made to the angular orientation of the fibre such that it produces maximum sensitivity. The interference pattern is actively monitored during this time to check whether the move along any direction increases or decreases the sensitivity. Once a sensitivity between 300 - 500 nm/mV is reached, the fibre piezo is locked onto the quadrature point (point of maximum slope). After which the cantilever is driven using the dither piezo and the output from the interferometer is put into the lockin amplifier to extract the amplitude and phase of the cantilever tip. The amplitude signal is also required during the approach.

After this the subsrate is approached towards the cantilever in a coarse manner, using the hammer piezo. Eventually, the cantilever and the fibre get immersed in the buffer solution. After this, an auto-approach program is run, in which both the hammer piezo and the scanner piezo work in combination. The scanner piezo first increases to its maximum extension and if the amplitude does not fall the hammer piezo moves the substrate upwards. This process is repeated until the scanner extension results in amplitude drop of the tip, which signifies the cantilever has approached the substrate. Amplitude going below this target amplitude, implies the approach has been overshot and retraction needs to be done. The approach process is only stopped when the target amplitude is reached, and corresponds to the zero voltage input of the scanner piezo. This is required so that we can have maximum z-range while performing the experiments.

After this a setpoint amplitude is set for the grid, an approach is done till the amplitude reaches the setpoint. After which the cantilever is retracted and the amplitude and phase of the tip are recorded. While pulling on the protein the length of the cantilever is not perpendicular to the direction of pulling. The cantilever makes an angle of 10°with the horizontal axis, the component of force that acts perpendicular of the length of the cantilever that bends it accounts for 98% of the total force. Hence the inclination of the cantilever with respect to the horizontal axis can be neglected. The x y position of the substrate is change and the approach retract is restarted until the entire grid is visited by the cantilever.

The main idea behind implementing this detection scheme was to perform off-resonance experiments. We had argued in the previous chapter that the bending signal while doing the experiments would be extremely low. Fig 3.10 shows experimental data, in which the variation in amplitude (blue) can be seen as the protein

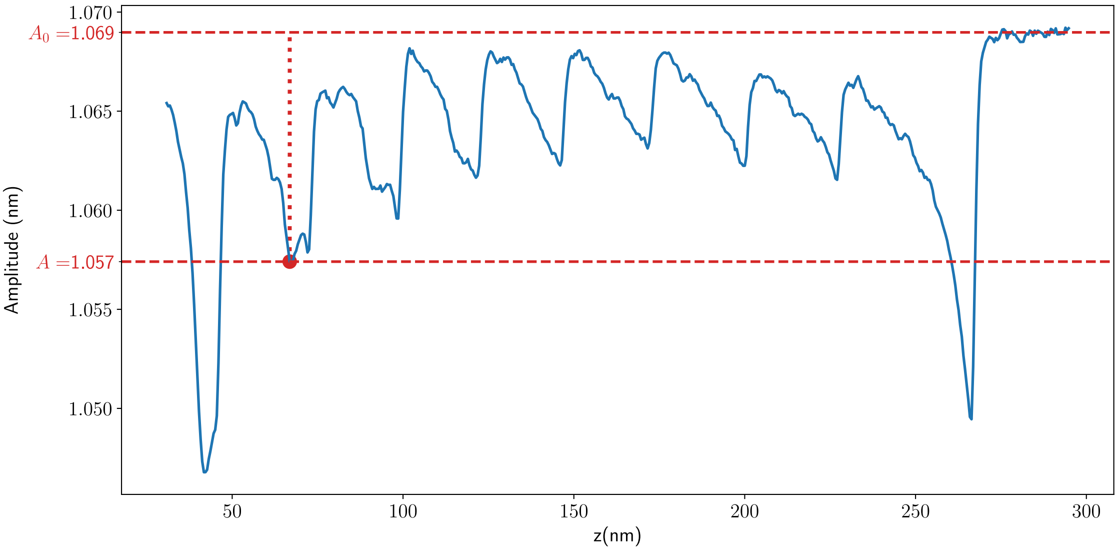

Figure 3.10: Figure showing variation of tip amplitude as the cantilever is retracted away from the surface with the protein attached it. The cantilever stiffness for this experiment is 0.8N/m (800pN/nm) and the sensitivity is 300nm/mV

octamer unfolds. The flat part of the blue curve beyond 270 nm signifies the tip amplitude after the protein has detached. We know, at off-resonance, when nothing is attached to the cantilever the tip and the base have the same amplitude. Therefore, this flat region in the amplitude curve is the drive amplitude A_0 and all the other points in the curve signify the drop in amplitude of the tip from its free value. From the figure, one can see that the drop in amplitude at the point marked in red is around 12 pm and it represents the bending in the cantilever. If one only measures this drop, the signal to noise ratio would be extremely low. Hence, necessitating the use of interferometer based displacement detection scheme.

In the next chapter we will be going through the measurements and the modelling required to extract the viscoelasticity of the folded protein alone.

BIBLIOGRAPHY

[1] D Rugar, HJ Mamin, R Erlandsson, JE Stern, and BD Terris. Force microscope using a fiber-optic displacement sensor. *Review of Scientific Instruments*, 59(11):2337–2340, 1988.

[2] Peter M Hoffmann, Steve Jeffery, John B Pethica, H Özgür Özer, and Ahmet Oral. Energy dissipation in atomic force microscopy and atomic loss processes. *Physical Review Letters*, 87(26):265502, 2001.

[3] Shah H Khan, George Matei, Shivprasad Patil, and Peter M Hoffmann. Dynamic solidification in nanoconfined water films. *Physical review letters*, 105(10):106101, 2010.

[4] Shivprasad Patil, George Matei, Ahmet Oral, and Peter M Hoffmann. Solid or liquid? solidification of a nanoconfined liquid under nonequilibrium conditions. *Langmuir*, 22(15):6485–6488, 2006.

[5] Shivprasad Patil, George Matei, Hang Dong, Peter M Hoffmann, Mustafa Karaköse, and Ahmet Oral. A highly sensitive atomic force microscope for linear measurements of molecular forces in liquids. *Review of Scientific Instruments*, 76(10):103705, 2005.

[6] Venkatesh Subba-Rao, Chandran Sudakar, Jason Esmacher, Mircea Pantea, Ratna Naik, and Peter M Hoffmann. Improving a high-resolution fiber-optic interferometer through deposition of a tio 2 reflective coating by simple dip-coating. *Review of Scientific Instruments*, 80(11):115104, 2009.

CHAPTER

FOUR

MEASUREMENT

4.1 I27 as a Suitable Candidate for Measurement of Viscoelasticity

Before we go into the measurement details, a discussion on the protein used to perform experiments is warranted. The protein used in our experiments is a domain in the giant muscle protein titin. The protein titin is itself a part of the fibres belonging to the striated muscles like cardiac and skeletal. The striated muscles comprise of fibres that are bundled together with the help of connective tissue.

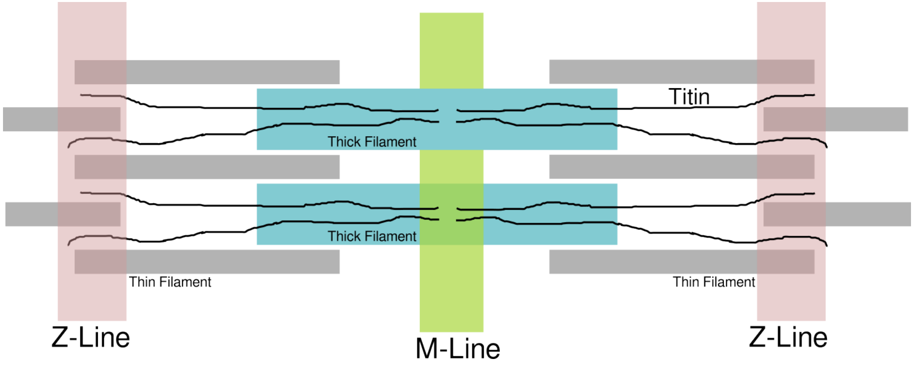
Titin
Thick Filament
Thick Filament
Thin Filament
Thin Filament
Z-Line
M-Line
Z-Line

Figure 4.1: Schematic of the sacromere, depicting titin tethered to the thick filament (myosin) and the Z-Line.

Each fibre contains multiple fibril known as myofibrils. These in turn consist of two types of filaments, thick and thin [1]. The thick filaments is composed of myosin protein, that forms cross bridges with the thin filament due to its globular head as shown in figure 4.1. The thin filament comprises of actin bundles. The active part of the muscle contraction comes from the myosin sliding on the actin region [2]. The mysosin part of the fibril, is connected to the Z region with the help of titin. The giant tandem modular protein is reponsible for the passive elasticity of the straited muscle fibres [3, 4]. However, recent experiment has shown that the work done by titin domains while refolding could assist in the contractile motion of the sacromere [5]. Ig27 is a domain in this giant protein, which makes it suitable for performing experiments that probe its mechanical properties.

Furthermore, Ig27 unfolds in an interesting manner when subjected to a force along its N-C direction. It has an all beta sheet structure as shown in the inset of figure 4.1. When a force on the protein is below approximately 95 pN. The protein stays in its native state with the beta sheet network intact. As the force on the protein is increased, the network between A and B strand gets disrupted. The A strand is released, effectively increasing the contour length of the unfolded protein by 0.66 nm [6]. This state of the protein is called the intermediate state.

Ig27 has been a standard for force spectroscopy experiments for some time now. The mechanism of this two state unfolding has been the subject of numerous studies[7–12]. Two inferences from past studies worth mentioning beforehand are the native state to intermediate state transition is independent of temperature [12] and the force required to transition from native to intermediate state is not dependent on the loading rate [11]. These properties of the domain can be compared with our results to achieve a multifaceted understanding of the dynamics of the protein.

4.2 Total Stiffness and Friction

In this section we will be going through the features observed in the experiment in a qualitative manner. The total stiffness and friction coefficient of the entity under the tip can be calculated using the following relations.

$$\bar{k} = k_c\Big(\frac{A_0 \cos\theta}{|A|} - 1\Big) \tag{4.1}$$

$$\bar{\gamma} = k_c \frac{A_0}{|A|\omega} \sin\theta \tag{4.2}$$

Using the $|A|$ and θ values recorded during the experiment. The $\bar{k}$ and $\bar{\gamma}$ obtained are of the entire protein construct. The stiffness quantified here is the combined stiffness of the entire polyprotein along the unfolded chain. At relatively large amplitudes (A_0 $\sim$1 nm), and high stretch (above $\sim$ 95 pN), a portion of the tip amplitude ($\sim$ 0.1 nm) is contributed by the folded domains.

Figure 4.3 shows measurement of stiffness (continuous blue line) and friction coefficient (continuous red line) of the polyprotein (I-27)$_8$ as the separation z between the substrate and the cantilever base is increased in a quasi-static manner. It is observed that for the first four unfolding domains, after the initial increase at lower extensions, the stiffness abruptly goes down or plateaus and rises again (the shaded region in figure 4.3). This is not seen in the last four domains. The total measured dissipation $\bar{\gamma}$ also decreases with each consecutive unfolding peak.

The Marko-Siggia approximation describes the force extension behaviour of unfolded domains in conventional experiments [13]. It provides a force-extension relationship, which can be fitted to experimental force curves to obtain relevant parameters such as persistence length p and contour length L_c. The derivative of force with respect to extension provides a relationship between local stiffness k_{wlc} and end end-to-end molecular extension z [13].

At lower extensions in each unfolding profile of first four domains, where stiffness of chain is much smaller compared to folded domains, wlc model of entropic elasticity given by equation 4.1 fits well (green continuous line). In the shaded region, however, the measured stiffness (continuous blue line) is lower than entropic stiffness. Corresponding to this region, phase also shows lag and there is measurable dissipation of energy (continuous red line).

We argue that in the shaded region of figure 4.3, measured stiffness contains contribution from the folded domains. Note that when the response deviates from wlc description, a folded domain is likely to be in either the native or the intermediate state and hence the number of domains in either state is not known. However, as z is increased, loading the folded domains further, all of them fall into the intermediate state, each adding 0.66 nm of contour length to the chain. At this point, as seen in figure 4.3, the stiffness starts to rise again before the next domain is unfolded. In this region, shaded in dark, we use our analysis method to obtain the stiffness and friction coefficient of the folded domains which are in the intermediate state. These observations are explained in figure 4.4 with the help of a schematic.

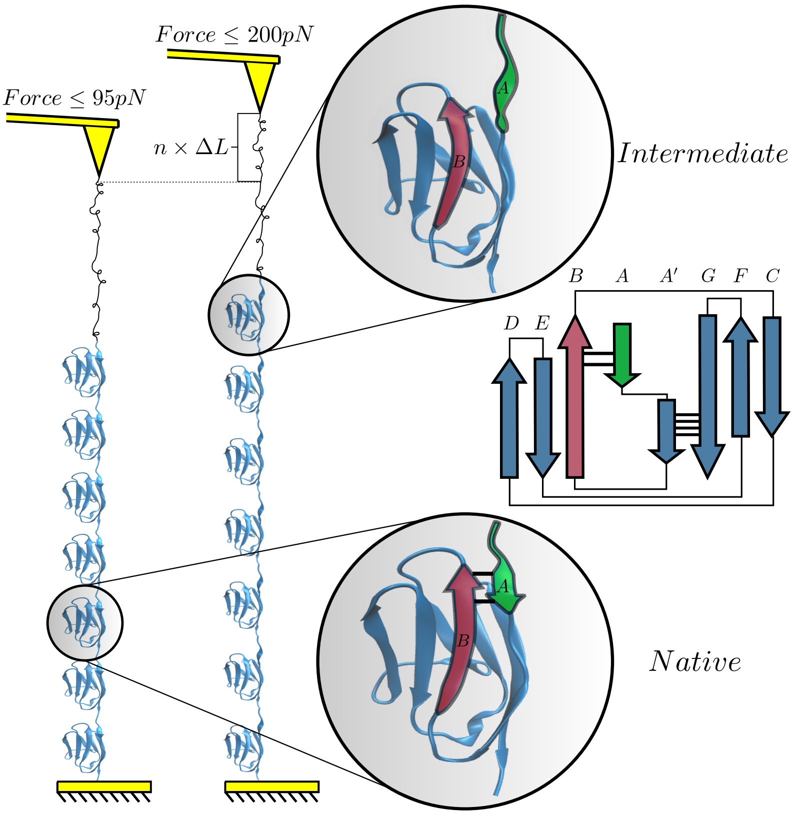

Figure 4.2: The octomer of I-27 under force. The cartoon shows a situation, wherein one domain is unfolded and the remaining seven are in the folded state. When the folded domains are pulled by increasing z, the force is applied to domains through wlc chain of first unfolded domain. When the force exceeds ≈ 95 pN (shaded region in figure 4.2), the domains in the native state (left) are pushed into mechanical intermediate(right). As shown in the β-sheet schematic, the hydrogen bond network between B-A and A'-G is responsible for the mechanical stability of the native state, of which the network between A and B is broken for the intermediate, elongating the protein by $n \times \Delta L$, where $\Delta L = 0.66$ nm.

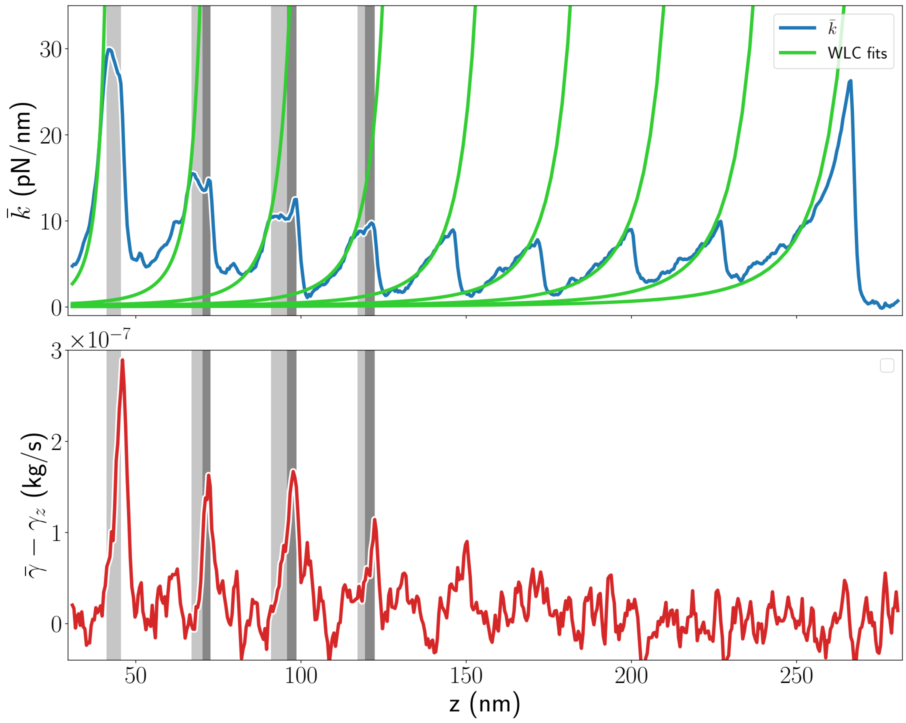

Figure 4.3: The measured combined stiffness (blue continuous) and friction coefficient (red continuous) of unfolded chain and the folded domains of Ig27 octamer as the domains sequentially unfold. The amplitude and phase of the tip displacement is used for the calculation. The data shows a sawtooth pattern of unfolding events similar to constant velocity pulling experiments. The green continuous line is a fit to the wlc model. The mean difference in contour length between two consecutive peaks is 29 ± 0.8 nm. A persistence length of 0.4 nm is used. The first four events deviate from wlc in the shaded region where folded domains are comparable in stiffness to the unfolded chain and contribute to the measurement. The dissipation is seen in the corresponding region due to the internal friction in folded domains. The data in the dark shaded region is used for further analysis to obtain the stiffness and internal friction coefficient of the folded state. Cantilever stiffness is 0.6 N/m, The cantilever base is excited with frequency 2.1 kHz and amplitude 1 nm. The plot is representative of more than 50 traces recorded at different frequencies and amplitudes.

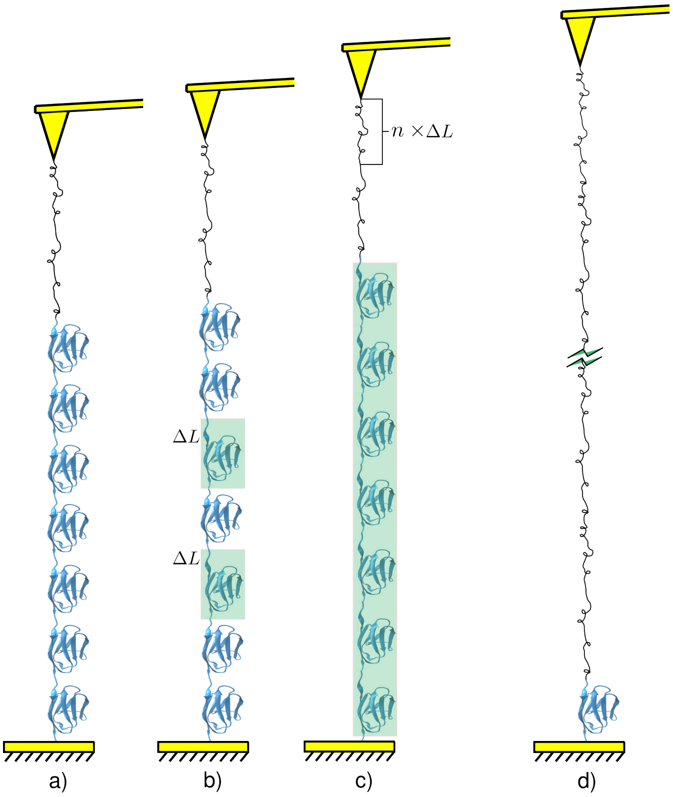

Figure 4.4: a) Cartoon showing seven domains in the native state and one unfolded domain. When all the folded proteins are in the native state, the total stiffness measured fits the WLC model. The folded domains are in series with the unfolded domains, the element with the lower stiffness contributes to the total measured stiffness. b) Under forces exceeding 95pN, the protein goes into the intermediate state and the wlc model stops fitting the total stiffness data and we start measuring dissipation as well. From this we conclude that some of the folded domains have entered the intermediate, but exact number is not known. This region is depicted by the light grey shaded region in figure 4.2 . c) After the initial decrease in stiffness, the total measured stiffness starts to rise again, here all the domains have entered the intermediate state. d) After 4 unfolding events the contour length of the unfolded chain becomes larger, making it more compliant than a short chain at the same force (explanation in the next section). Due to which its stiffness becomes much lower than the intermediate state as well and the total stiffness measurement has contribution coming only from the unfolded chain. This is supported by the WLC fits to the last four unfolding domains

4.3 Compliance of an Unfolded Protein

Before delving into the theoretical modelling of the protein cantilever system, it is important to emphasise on the mechanical properties of the unfolded chain.

The force-extension behavior of a polymer chain is described by Marko-Siggia approximation of Worm-Like-Chain (wlc) model[13]. According to the model, which has been shown to work for experimental data obtained using AFM and optical tweezers, the force versus extension is given by

$$F = \frac{k_B T}{p}\Big(\frac{1}{4(1 - z/L_c)^2} - \frac{z}{L_c} - \frac{1}{4}\Big) \tag{4.3}$$

The derivative F of this with extension z is stiffness k_{wlc}

$$k_{wlc} = \frac{dF}{dz} = \frac{k_B T}{pL_c}\Big(\frac{1}{2(1 - z/L_c)^3} + 1\Big) \tag{4.4}$$

Fig. 4.5 shows plots of these two equations for a fixed persistence length $p = 0.4$ nm and different contour lengths L_c. The L_c depends on number of folded domains n. As domains are sequentially unfolded in AFM experiments, each unfolded domain adds 29 nm to the total contour length. The plots clearly indicate that the stiffness of the chain rises sharply compared to the force for larger contour lengths. This means that the chain is more complaint under a given force for larger contour lengths. When there are 8 folded domains, the stiffness is 37 pN/nm for 160 pN, the force at which the domain unfolds. It is comparable to the domain stiffness. This progressively decreases to 12 pN/nm when there are only 4 domains which are folded. It means that next domain unfolds before the chain becomes stiff enough, to contribute to the total stiffness measurement. For last four domains, the contribution to the total stiffness by folded domains is immeasurably low and the wlc model fits to the entire stretching of the molecule till next domain unfolds. It is noteworthy that the dissipation is also close to zero in this region.

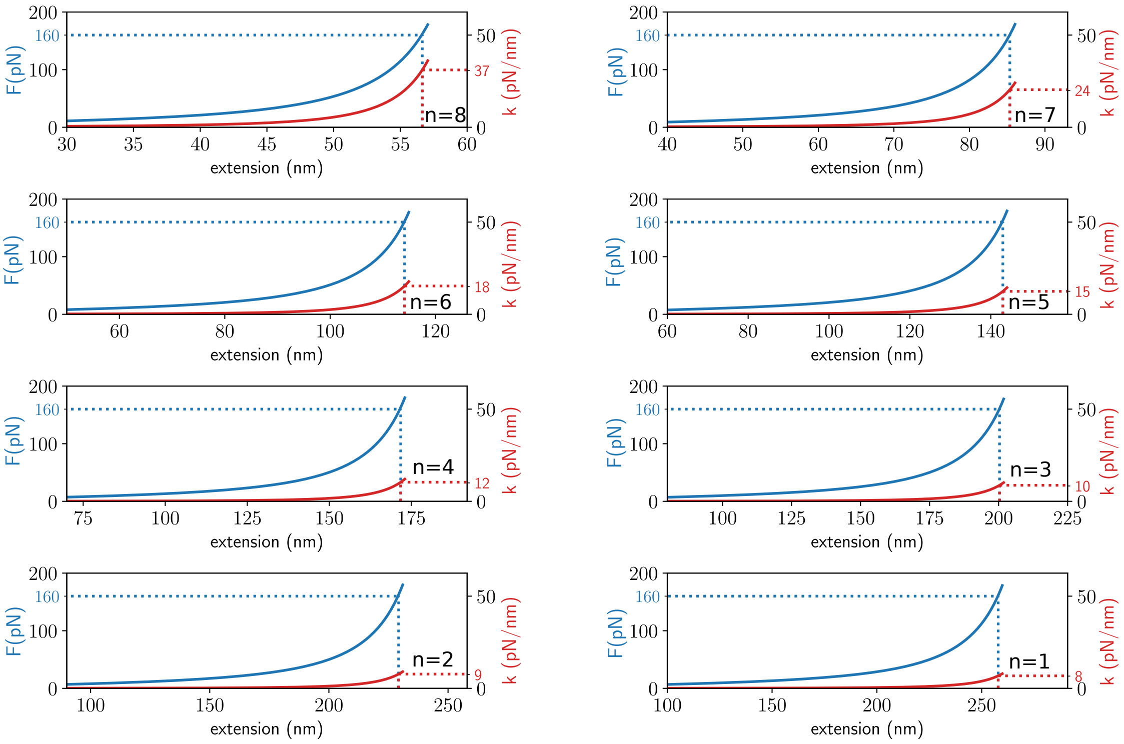

Figure 4.5: Force and stiffness variation for each contour length. With each unfolding event, the unfolded chain becomes more complaint for the same force (∼ 160) pN, thereby dominating the total measured stiffness. The protein is unfolded before the chain has a comparable stiffness to the folded domains so that they start to contribute to the total stiffness measurement. Thus, last four domains unfold without contributing to the stiffness measurement and wlc fits to the entire stretching of the chain.

4.4 Model

The stiffness and friction coefficient of the material can then be quantified using equations 4.1 and 4.2. The task at hand is to get a relation for the total stiffness and friction co-efficient in terms of the individual constituents, ie, the folded and unfolded domains. For this purpose we start with a model which describes our system, and then validate it with our experimental data. Figure 4.6 shows the model being utilised for the analysis.

For a particular mean tip-sample separation z, the force on all elements such as the unfolded chain, the folded domains and the linker connecting the domains is same.

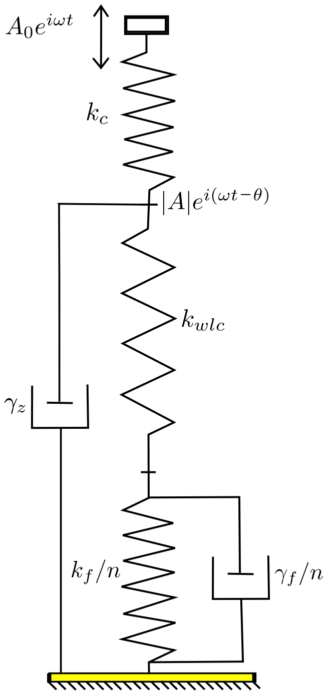

Figure 4.6: A spring-dashpot model for the protein-cantilever system. A_o and A are the base and tip amplitude respectively and θ is the phase lag between them. ω is the drive frequency. k_{wlc} and γ_z are the unfolded chain stiffness and surface damping respectively. k_f and γ_f are the stiffness and friction coefficient of the folded domain, where k_f/n and γ_f/n means n of them are in series.

$$k_c(A_0 - A) = \left[\left(\frac{n}{k_f + i\gamma_f\omega} + \frac{1}{k_{wlc}}\right)^{-1} + i\gamma_z\omega\right]A \tag{4.5}$$

Where n is number of folded domains.

Rearranging equation 4.5

$$k_c\left(\frac{A_0}{A} - 1\right) = \left(\frac{1}{k_f + i\gamma_f\omega} + \frac{1}{k_{wlc}}\right)^{-1} + i\gamma_z\omega$$

$$k_c\Big(\frac{A_0}{|A|}e^{-i\theta} - 1\Big) = \Big(\frac{1}{k_{wlc}} + \frac{n}{k_f + i\gamma_f\omega}\Big)^{-1} + i\gamma_z\omega$$

$$k_c\Big(\frac{A_0}{|A|}\cos\theta - 1\Big) + ik_c\frac{A_0}{|A|}\sin\theta = \Big(\frac{1}{k_{wlc}} + \frac{n}{k_f + i\gamma_f\omega}\Big)^{-1} + i\gamma_z\omega$$

Using equations 4.1 and 4.2

$$\bar{k} + i\bar{\gamma}\omega = \Big(\frac{1}{k_{wlc}} + \frac{n}{k_f + i\gamma_f\omega}\Big)^{-1} + i\gamma_z\omega \tag{4.6}$$

$$= \Big(\alpha - i\beta\omega)^{-1} + i\gamma_z\omega \tag{4.7}$$

$$\text{where} \quad \alpha = \frac{1}{k_{wlc}} + \frac{nk_f}{k_f^2 + \omega^2\gamma_f^2} \quad \text{and} \quad \beta = \frac{n\gamma_f}{k_f^2 + \omega^2\gamma_f^2}$$

$$\bar{k} + i\bar{\gamma}\omega = \frac{\alpha}{\alpha^2 + \omega^2\beta^2} + i\omega\Big(\frac{\beta}{\alpha^2 + \omega^2\beta^2} + \gamma_z\Big) \tag{4.8}$$

The real and imaginary parts of equation can be separated to obtain measured stiffness and friction coefficient in terms of the model parameters.

$$\bar{k} = \frac{\alpha}{\alpha^2 + \omega^2\beta^2} \tag{4.9}$$

$$\bar{\gamma} = \frac{\beta}{\alpha^2 + \omega^2\beta^2} + \gamma_z \tag{4.10}$$

We will now be validating our model, with the help of experimental results we have obtained

Case 1:

When no protein is attached to the cantilever the α and β terms in the equation 4.9 and equation 4.10 are 0. This implies that the measured stiffness, in this case, should be zero and the only damping measured should be that provided by the surface. This is seen when the cantilever is pulled off without a molecule attached to it(See figure 4.7 (a)).

$$\bar{k} = 0 \qquad\qquad \bar{\gamma} = \gamma_z$$

Case 2:

When an octamer is picked up by the tip and all its 8 domains are pulled at, the number of folded domains n = 8. As domains are unfolded sequentially, "n" reduces by 1 at each unfolding event. However, if the stiffness of folded native states is much higher than the chain stiffness ($k_{wlc} << k_f$), the second term in α is negligible. Similarly, β also is negligibly small.

$$\bar{k} = k_{wlc} \qquad\qquad \bar{\gamma} = \gamma_z$$

This is also supported by the experiments where the stiffness fits well to WLC model of elasticity as seen in Figure 4.2. This corresponds to the condition when all domains are in native state Figure 4.4(a). The friction that is measured is coming only from the surface, this supported by the experimental data shown in figure 4.7(a). Where the measured damping has a background which also present when no protein is attached.

Case 3:

It is known that in the case of I27, when it is pulled with a force above ∼ 90-100 pN, the domain makes a transition to intermediate which is softer as is evident from the data in Fig. 4.3.

When n domains are in intermediate, measured stiffness and friction coefficient are given by equation 4.9 and equation 4.10 with the respective values of α and β.

$$\gamma = \bar{\gamma} - \gamma_z = \frac{\dfrac{n\gamma_f}{k_f^2 + \omega^2\gamma_f^2}}{\left(\dfrac{1}{k_{wlc}} + \dfrac{nk_f}{k_f^2 + \omega^2\gamma_f^2}\right)^2 + \left(\dfrac{n\gamma_f}{k_f^2 + \omega^2\gamma_f^2}\right)^2} \tag{4.11}$$

$$\bar{k} = \frac{\dfrac{1}{k_{wlc}} + n\dfrac{k_f}{k_f^2 + \omega^2\gamma_f^2}}{\left(\dfrac{1}{k_{wlc}} + n\dfrac{k_f}{k_f^2 + \omega^2\gamma_f^2}\right)^2 + \left(\dfrac{n\gamma_f}{k_f^2 + \omega^2\gamma_f^2}\right)^2} \tag{4.12}$$

Where $\gamma = \bar{\gamma} - \gamma_z$ is damping provided by the protein alone. It is obtained by subtracting out the background due to surface damping by fitting a polynomial.(See figure 4.7(a)).

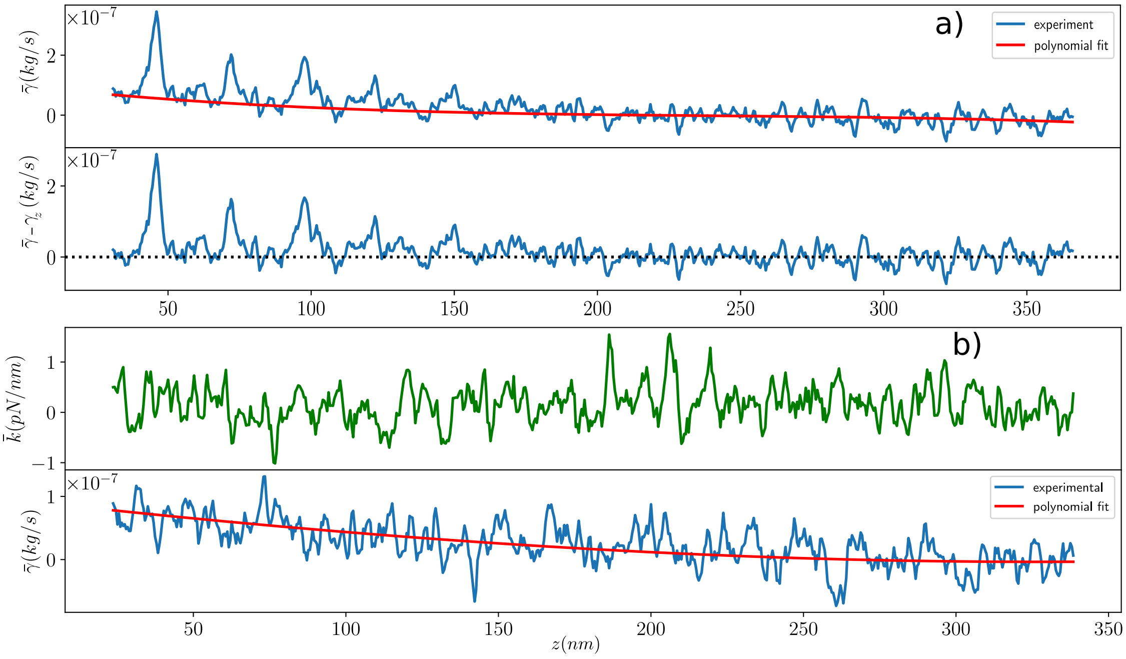

Figure 4.7: a) The measured total friction coefficient (blue) along with a polynomial fit (red) for the damping due to the surface effects. The lower panel in a) represents friction coefficient of the protein alone, $\bar{\gamma} - \gamma_z$ b) shows that measured stiffness is zero when the protein is not attached, however the damping due to the surface is still measured (blue).

Case 4:

With each unfolding event, the unfolded chain's contour length increases by 29 nm. The larger contour length makes the chain more complaint. The unfolding force is reached before the chain is extended to have a stiffness which is comparable to the folded intermediates. In this region usually after four unfolding events, the folded intermediate's stiffness again becomes much larger compared to the unfolded chain $k_{wlc} << k_f$. The surface damping at such large separations can also be neglected as is seen in the data. This reduces equation 4.11 and 4.12 to

$$\bar{k} = k_{wlc} \qquad\qquad \bar{\gamma} = \gamma_z = 0$$

Since our model and its special cases describe features observed in our experiments, we use equation 4.5 to get stiffness and friction coefficient of folded intermediates.

$$\Big(\frac{1}{\bar{k} + i(\bar{\gamma} - \gamma_z)\omega} - \frac{1}{k_{wlc}}\Big)^{-1} = \frac{k_f}{n} + i\frac{\gamma_f \omega}{n} \tag{4.13}$$

Simplifying this equation leads to the expression for stiffness and friction coefficient of the folded domains in terms of the experimentally measured quantities.

$$k_f = \frac{n\Big(\frac{\bar{k}}{\bar{k}^2 + \omega^2\gamma^2} - \frac{1}{k_{wlc}}\Big)}{\Big(\frac{\bar{k}}{\bar{k}^2 + \omega^2\gamma^2} - \frac{1}{k_{wlc}}\Big)^2 + \Big(\frac{\gamma\omega}{\bar{k}^2 + \omega^2\gamma^2}\Big)^2} \tag{4.14}$$

$$\gamma_f = \frac{n\Big(\frac{\gamma\omega}{\bar{k}^2 + \omega^2\gamma^2}\Big)}{\Big(\frac{\bar{k}}{\bar{k}^2 + \omega^2\gamma^2} - \frac{1}{k_{wlc}}\Big)^2 + \Big(\frac{\gamma\omega}{\bar{k}^2 + \omega^2\gamma^2}\Big)^2} \tag{4.15}$$

Where all the quantities on the right hand side are known experimentally. k_{wlc} is obtained by fitting wlc to the stiffness-extension data. In the next section, we describe our methodology to obtain k_{wlc} from our experimental data. Using equations 4.14 and 4.15, the stiffness and friction coefficient of the folded intermediates are obtained when all the folded domains n are in the intermediate state. In experiments, this is marked by the dark shaded region in figure 4.2, where the measured stiffness starts to rise again.

4.5 DATA ANALYSIS

4.5.1 ANALYSIS TO OBTAIN k_{wlc}

Fitting the wlc model: In the initial part of rising stiffness (region in figure 4.2, not shaded) for each unfolding event, all the folded domains are in the native state, where ($k_f >> k_{wlc}$). This leads to equation 4.9 reducing to $\bar{k} = k_{wlc}$, as discussed in the previous section. The contribution to measured stiffness in this region is entirely from the unfolded chain, as is evident from the wlc model fits. The differential form of the wlc model [13] which relates k_{wlc} to its end to end distance is fitted to the measured stiffness. The contour length L_c is the free parameter and the persistence length p is taken as 0.4 nm [10, 14].

$$\frac{dF}{dz} = \frac{k_B T}{p L_c}\Big(\frac{1}{2(1 - z/L_c)^3} + 1\Big) \tag{4.16}$$

It is observed that the wlc fits to the experimental data up to a certain value of the extension z, as seen in figure 4.3.

Reconstructing force profiles from stiffness data: In order to estimate the contribution from the unfolded chain, k_{wlc}, to the total measured stiffness (shaded region in figure 4.3), we need to evaluate force in this region. This is obtained by integrating the stiffness-extension data. This integration is done in two parts. First, this integration is done over the fitted wlc curve. Second, the numerical integration is carried out on the experimental data in the region where the wlc deviates from the measured stiffness-extension profile (shaded in blue). After obtaining the force profile in the shaded blue region, one can use the following to estimate k_{wlc}. The relationship is shown to work in the region of high stretch [15].

$$k_{wlc}(F) = \frac{4}{L_c}\sqrt{\frac{p}{k_B T}}F^{\frac{3}{2}} \tag{4.17}$$

4.5.2 OBTAINING k_f & γ_f

In equation 4.17, the contour length L_c needs to be evaluated for the analysis of the shaded region. Note that in this region, some of the folded domains are in the native state and some are in the intermediate. The intermediate is formed by breaking hydrogen bonds between A and B β-strands. Once broken, the β-strand A is released adding 0.66 nm to the contour length. As a result, it is difficult to obtain the exact value of L_c in the shaded region of a given unfolding event. Secondly, the number

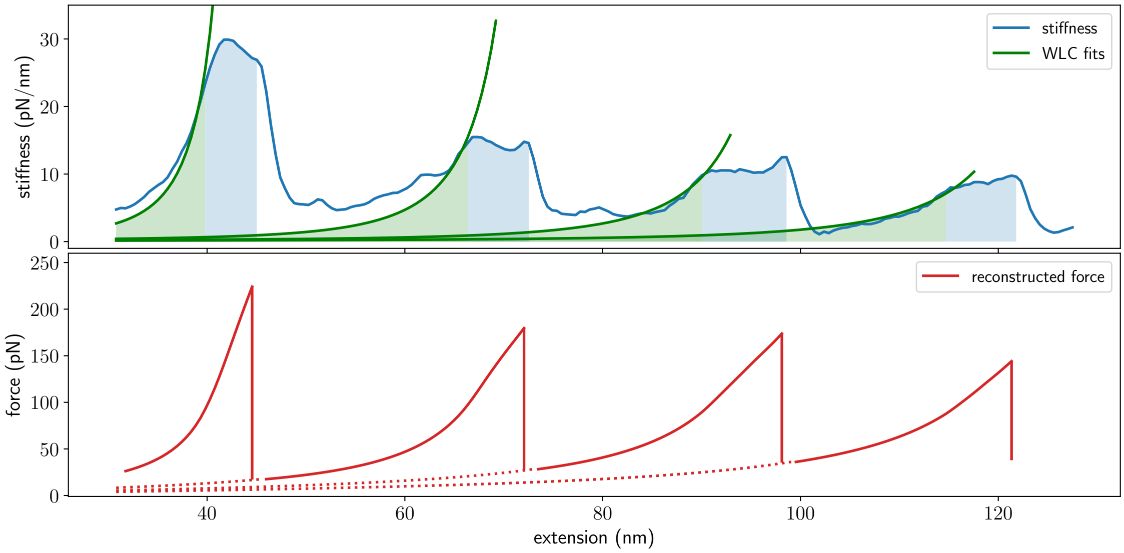

Figure 4.8: Numerical integration of the stiffness-extension profiles to obtain force-extension profiles. Continuous green curve- wlc fits, Continuous blue curve- experimental data, continuous red curve - force obtained after integration. The green shaded region represents integration done over fitted WLC model. The blue shaded region represents integration over experimental data where it deviates from WLC behavior.

of domains in the intermediate n, are needed in equation 13 and 14 to obtain the stiffness of folded intermediate. One of the noteworthy features of our data is that towards the end of the shaded region the measured stiffness starts to rise again. We argue that at this point, all the folded domains are in the intermediate. This allows us to use n in equation 4.14 and 4.15 and L_c in equation 4.16 becomes $L_c + n0.66$. With this, the k_{wlc} at each force $F(z)$ is determined and equation 13 and 14 are then used to estimate the stiffness and friction coefficient of folded intermediate. Note that we are able to measure the stiffness of the folded intermediate using this methodology, the stiffness of the native folded state is immeasurably high.

The analysis scheme to obtain k_f and γ_f is repeated over many data sets. The grey shaded region is used for the said data analysis. The values obtained at different forces are then plotted together in figure 4.10(c) and (d).

4.6 Features in the Friction Profiles

It is observed that the total friction coefficient peak height decreases as more and more domains unfold. This feature also needs explanation. It should be noted that the measured damping coefficient is not only of the domain that is unfolding. It is a combined response of all the domains and depends on many other quantities. The $\bar{\gamma}$ given by equation 10, depends not only on friction coefficient of individual domain γ_f, but also on stiffness of the wlc chain k_{wlc}, the number of folded domains n, and stiffness of the individual domain k_f. Of these, we argue that the γ_f and k_f remains fixed. Taking them as constants, we plot equation 4.11 in figure 4.9 to obtain the total damping coefficient $\bar{\gamma}$ as a function tip-substrate separation till 160 pN is reached and reducing n by 1 after each unfolding event and increasing the L_c by 29 nm. The plot clearly shows that the peak $\bar{\gamma}$ is decreasing with increasing unfolding events. Moreover, we plot the $\bar{\gamma}$ till the unfolding force is reached for the individual unfolding events and the unfolding force for individual domains are made to differ from one another due to the process being stochastic. This results in non-monotonous decrease in the total $\bar{\gamma}$ for each peak as seen in figure 4.9(b). The plots explain the observed decrease in the total friction coefficient as the domains sequentially unfold.

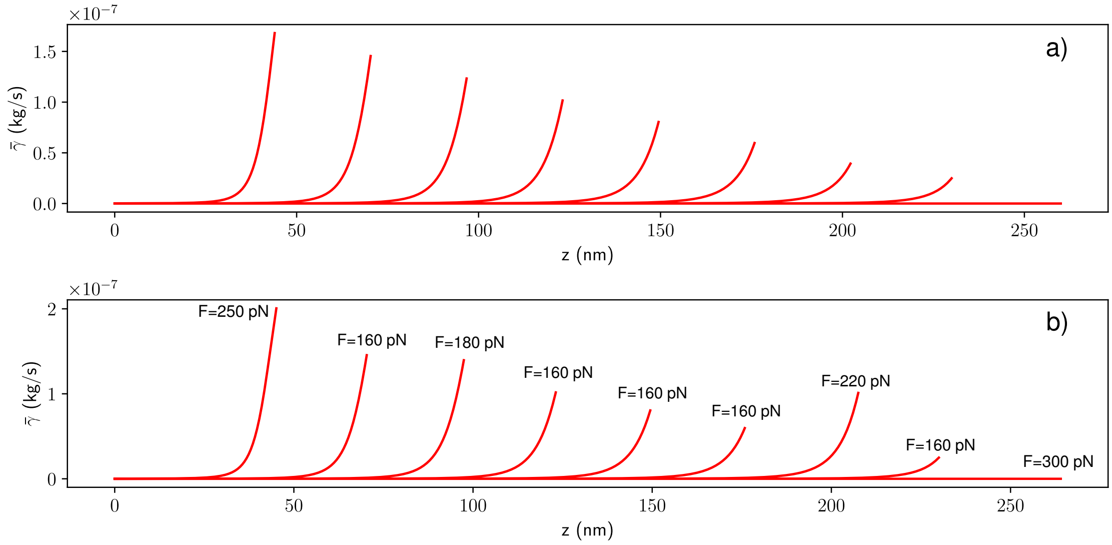

Figure 4.9: a)The plot of total friction coefficient $\bar{\gamma}$ calculated at different tip-substrate separation z using equation 10. Here the γ_z is taken to be zero. The contour length is increased by 29 nm after each event and n is reduced by one. k_f and γ_f are taken as 100 pN/nm and 2×10^{-6} kg/s. The variation in friction coefficient with respect to z is plotted for each event until 160 pN is reached. This is the average force at which domain unfolds. b) Each domain unfolds at slightly different force as the unfolding events are stochastic. We take similar values for all other parameters as in (a), however $\bar{\gamma}$ is now calculated and plotted for each event until unfolding force values are reached for that event. In both plots, it is seen that the peak in the total friction coefficient decreases as domains unfold one by one. The height of the peak also depends on the unfolding force for that event.

4.7 Viscoelasticity of a single folded domain

The numerical integration of stiffness-extension data, presented in figure 4.3, provides force-extension curve as shown figure 4.10(a). We use only first four domains from figure 2 from this analysis. Such force-extension profiles inform forces at which folded domains start to contribute to stiffness measurement. This is shown by dotted vertical lines intersecting the red curve depicting the force profile. The force at this intersection is threshold force after which, folded domain's stiffness contributes to the measurement. This occurs at 95± 16 pN. The protein unfolds completely at 161 ± 25 pN. Figure 4.9(b) shows bar plots obtained by this procedure for all our experimental data. Using dark shaded region in figure 2 for our analysis, we computed stiffness (k_f) and friction coefficient (γ_f) of the individual folded domains at different forces shown in figure 4.10(c) and (d).

Figure 4.9 indicates that folded protein's response starts to contribute to stiffness measurement when force on it exceeds $\sim$ 95 pN. This matches well with force required to make the transition from native to mechanical intermediate [6, 11, 12]. It suggests that our measurement of viscoelasticity is that of the folded intermediate, which is soft. The domains remain in the native state below $\approx$ 95 pN. In this region, which is not shaded in gray in figure 4.3, the data fits wlc behavior. It indicates that in this region folded domains in the native state are too stiff to make any discernible effect on tip amplitude. It is fully elastic having immeasurably high stiffness compared to the unfolded chain. Under the loading force F, the mechanical intermediate's stiffness increases slightly with force, whereas the friction coefficient does not show any appreciable change.

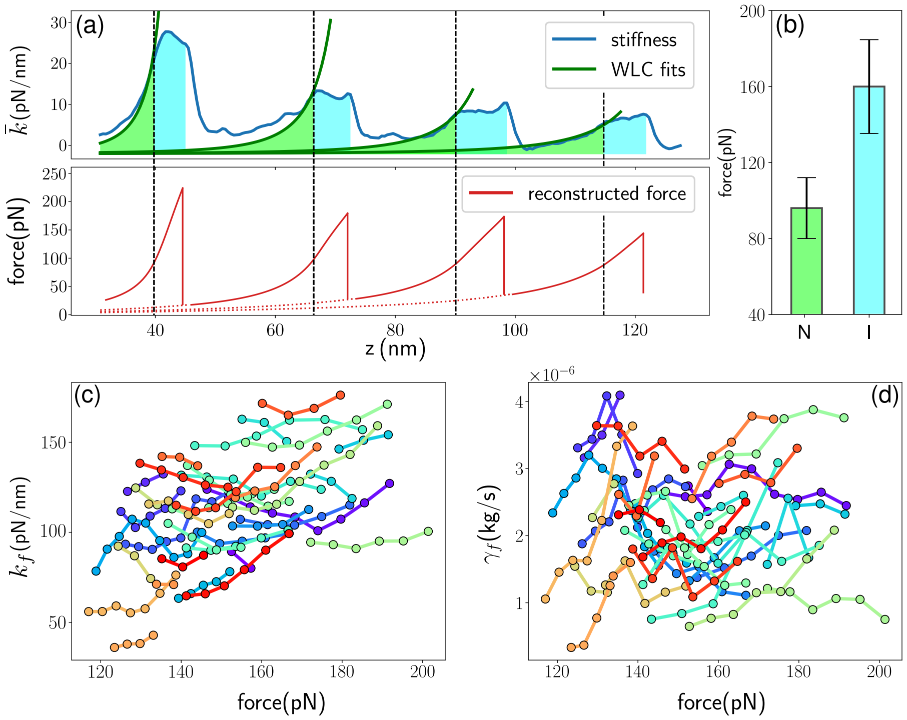

Figure 4.10: a)The integration of stiffness-extension (continuous blue line) provides force-extension plot (continuous red line). The vertical dotted line indicates deviation of stiffness-extension from the wlc model fit (continuous green lines). Its intersection with force-extension gives force at which, stiffness has a contribution from folded domains. b) Bar plots of force where transition occurs and the force required to unfold a domain completely (N: Native and I: Intermediate). The deviation kicks-in when force exceeds 95 ± 16 pN. The force required to unfold the domain completely is 161 ± 25 pN. These values match with force needed to push domains of $(\text{I-27})_8$ into the intermediate and then unfold it completely[6]. The mean force required to unfold a domain completely, is $\sim$ 200 pN in static pulling experiments. It is $\sim$ 160 pN in our experiments due to the energy provided to it through oscillations. c) stiffness k_f and friction coefficient γ_f of a single folded domain at different forces F. The plots provide viscoelastic characterization of single folded intermediate. The data points in the same colour are from the analysis of same unfolding peak. The data is pulled together from many different profiles similar to the one shown in figure 4.2

4.8 Discussion

It has not been possible to measure viscoelastic response of single folded protein using AFM, a technique at the forefront of pulling single proteins. The conventional deflection detection scheme, used to measure cantilever response, records cantilever bending as opposed to displacement in our experiments. It is important to operate off-resonance in order to avoid the stiffness change in the molecule affecting the phase, which produces measurement artefacts. The bending signal measured with deflection detection scheme is immeasurably low in off-resonance operation.

It is possible to estimate Young's modulus G and the viscosity η from the measurement of stiffness and friction coefficient using dimensional analysis argument. $G = k \times L/A$, Where L is length, A is the cross sectional area of the object and k is its stiffness. Since we do not know the orientation of protein, taking it to be a cube of side 4 nm, results in an estimate of $G \sim 0.2$ GPa. Note that the native state has an even higher value of G. G_{glass} is ~ 50 GPa and G_{steel} is ~ 200 GPa. For the estimate of η, we take an object of $\sqrt{bd}$ moving in a medium of viscosity η. d is extension in the folded domain. $\gamma = 6\pi\eta\sqrt{bd}$; $\eta \sim 150$ Pa.s. This is in the same order with earlier estimates by group of Hansma from tip relaxation on Lysozyme[16], however a factor of $\sim 10^5$ times higher than the ones estimated from folding-refolding experiments [17], which Wang and Zocchi attributed to shear thinning, $\eta \sim 1/\omega^2$ [18]. It is likely that, using the folding rate dependence on solvent viscosity, one measures internal friction of the transition state, rather than that of the folded structures, as in this work.

Considering the folded intermediate as a viscoelastic element, its relaxation time is $\tau = \gamma_f/k_f \approx 10$ μs. The dissipation of energy by intermediate at μs timescales suggests that the oscillatory perturbation provided to reaction co-ordinate couples with a slowly relaxing mode. The all-atom simulations have shown that structural relaxation processes involving the protein backbone are in the microsecond time scale[19]. The high stiffness and lack of dissipation of the native state suggest that, in this case, modes coupled to the reaction coordinate relax much faster. This drastic change in dynamics by merely breaking the hydrogen bond network between strands A and B, keeping the structure otherwise intact, is an intriguing new aspect of protein dynamics.

It has been shown in pulling experiments that transition from native to mechanical intermediate of I-27 does not depend on temperature or pulling speed, whereas the unfolding force of the intermediate shows this dependence clearly[11, 12]. Based on this, it has been argued that energy landscape of the intermediate is rugged whereas the native state of I-27 works as a force buffer to protect it from large physiological forces[11] . Our measurements are consistent with these findings. We do not see any dissipation in the folded native state and stiffness drops from an immeasurably high value to $\sim$ 100 pN/nm as the protein transitions from native to mechanical intermediate accompanied by dissipation, indicating ruggedness.

Borrowed from the theory describing amorphous glassy systems[20], the energy landscape description used in the study of protein's folding-refolding dynamics is empirically successful, at least for small proteins. However, this community debates the question - to what extent the projection of multi-dimensional landscape onto a single reaction co-ordinate is accurate[21]. The success of one dimensional picture relies on the separation of fluctuation time-scales of the chosen co-ordinate with the rest[21].We have provided the first direct observation of internal friction in a folded state through stress-strain analysis. Our measurement scheme provides a direct test of such coupling between the end-to-end distance co-ordinate and other dimensions in the reduced, multidimensional protein landscape. The internal friction measured here is a result of energy loss in driving the folded state through many of its substates and it may provide useful insights into the inter-conversion rates[22]. The observed dissipation in our experiments is not possible unless the end-to-end distance reaction coordinate, which is modulated by the tip at $\sim$ 2 KHz is coupled to slowly relaxing backbone dynamics[19]. The forced oscillations of end-to-end distance at $\sim ms$ timescale results in dissipation through such coupling.

The protein of choice in our experiments is not only a paradigm in pulling experiments, but also provides us a native elastic state and a viscoelastic mechanical intermediate in one experiment. We show here that only the network of hydrogen bonds between β strands A and B decide the fate of mechanics governing IgG domains. The domain behaves like a Hookean solid, having no dissipation with the network intact, whereas it has viscous elements, if the network is broken. Understanding effects of such local changes on global properties of folded macromolecules are crucial for unraveling the mechanism of allostery[23, 24].

While our stiffness measurements match well with previous efforts[25, 26], the friction coefficient of single protein's folded state are not yet measured. We discuss new possibilities opened with this ability. Internal friction implies a rough energy landscape and slow dynamics due to frustration. Our direct measurement of dissipation also reveals that intermediate state is frustrated. It allows estimate of effective diffusion coefficient through Stoke-Einstein relationship $D = K_B T/\gamma$, where γ is the friction coefficient. From our measurement of γ for the intermediate, the diffusion coefficient is $D = (1.94 \pm 0.05)\times\ 10^3\ \mathrm{nm}^2/\mathrm{s}$. It is possible to estimate ruggedness (ϵ) by using Zwanzig relationship and measuring D at two different temperatures[27]. Secondly, using our experimental scheme , where the folded state is driven out of equilibrium, the rupture-forces distribution along with energy dissipation to maintain the non-equilibrium state can be used to extract information about the dynamics of slow processes[22], which are poorly understood at present.

In conclusion, we simultaneously and directly measure stiffness and internal friction of single folded protein domain for the first time. In particular, we find that beyond a threshold force, the IgG domain of titin moves from an elastic solid-like native state to a viscoelastic mechanical intermediate, which dissipates energy, providing the first direct evidence of internal friction. The capability demonstrated in our experiment provides hope of relating mechanics to chemical details at the level of single bonds by coupling this type of measurement to suitable single-molecule optical spectroscopy, such as Förster Resonance Energy Transfer.

BIBLIOGRAPHY

[1] Henk L Granzier, Gerald H Pollack, et al. *Elastic filaments of the cell*, volume 481. Springer Science & Business Media, 2000.

[2] Andrew F Huxley and Ro M Simmons. Proposed mechanism of force generation in striated muscle. *Nature*, 233(5321):533–538, 1971.

[3] Wolfgang A Linke and Julio M Fernandez. Cardiac titin: molecular basis of elasticity and cellular contribution to elastic and viscous stiffness components in myocardium. In *Mechanics of Elastic Biomolecules*, pages 483–497. Springer, 2003.

[4] Henk Granzier and Siegfried Labeit. Cardiac titin: an adjustable multi-functional spring. *The Journal of physiology*, 541(2):335–342, 2002.

[5] Jaime Andrés Rivas-Pardo, Edward C Eckels, Ionel Popa, Pallav Kosuri, Wolfgang A Linke, and Julio M Fernández. Work done by titin protein folding assists muscle contraction. *Cell reports*, 14(6):1339–1347, 2016.

[6] Piotr E Marszalek, Hui Lu, Hongbin Li, Mariano Carrion-Vazquez, Andres F Oberhauser, Klaus Schulten, and Julio M Fernandez. Mechanical unfolding intermediates in titin modules. *Nature*, 402(6757):100–103, 1999.

[7] Susan B Fowler, Robert B Best, Jose L Toca Herrera, Trevor J Rutherford, Annette Steward, Emanuele Paci, Martin Karplus, and Jane Clarke. Mechanical unfolding of a titin ig domain: structure of unfolding intermediate revealed by combining afm, molecular dynamics simulations, nmr and protein engineering. *Journal of molecular biology*, 322(4):841–849, 2002.

[8] Robert B Best, Susan B Fowler, Jose L Toca Herrera, Annette Steward, Emanuele Paci, and Jane Clarke. Mechanical unfolding of a titin ig domain: structure of transition state revealed by combining atomic force microscopy,

protein engineering and molecular dynamics simulations. *Journal of molecular biology*, 330(4):867–877, 2003.

[9] Philip M Williams, Susan B Fowler, Robert B Best, José Luis Toca-Herrera, Kathryn A Scott, Annette Steward, and Jane Clarke. Hidden complexity in the mechanical properties of titin. *Nature*, 422(6930):446–449, 2003.

[10] Matthias Rief, Mathias Gautel, Filipp Oesterhelt, Julio M Fernandez, and Hermann E Gaub. Reversible unfolding of individual titin immunoglobulin domains by afm. *science*, 276(5315):1109–1112, 1997.

[11] João M Nunes, Ulf Hensen, Lin Ge, Manuela Lipinsky, Jonne Helenius, Helmut Grubmüller, and Daniel J Muller. A “force buffer” protecting immunoglobulin titin. *Angewandte Chemie International Edition*, 49(20):3528–3531, 2010.

[12] Yukinori Taniguchi, David J Brockwell, and Masaru Kawakami. The effect of temperature on mechanical resistance of the native and intermediate states of i27. *Biophysical journal*, 95(11):5296–5305, 2008.

[13] John F Marko and Eric D Siggia. Stretching dna. *Macromolecules*, 28(26):8759–8770, 1995.

[14] Masaru Kawakami, Katherine Byrne, David J Brockwell, Sheena E Radford, and D Alastair Smith. Viscoelastic study of the mechanical unfolding of a protein by afm. *Biophysical journal*, 91(2):L16–L18, 2006.

[15] Bhavin S Khatri, Katherine Byrne, Masaru Kawakami, David J Brockwell, D Alastair Smith, Sheena E Radford, and Tom CB McLeish. Internal friction of single polypeptide chains at high stretch. *Faraday discussions*, 139:35–51, 2008.

[16] Manfred Radmacher, Monika Fritz, Jason P Cleveland, Deron A Walters, and Paul K Hansma. Imaging adhesion forces and elasticity of lysozyme adsorbed on mica with the atomic force microscope. *Langmuir*, 10(10):3809–3814, 1994.

[17] Troy Cellmer, Eric R Henry, James Hofrichter, and William A Eaton. Measuring internal friction of an ultrafast-folding protein. *Proceedings of the National Academy of Sciences*, 105(47):18320–18325, 2008.

[18] Yong Wang and Giovanni Zocchi. The folded protein as a viscoelastic solid. *EPL (Europhysics Letters)*, 96(1):18003, 2011.

[19] David E Shaw, Paul Maragakis, Kresten Lindorff-Larsen, Stefano Piana, Ron O Dror, Michael P Eastwood, Joseph A Bank, John M Jumper, John K Salmon, Yibing Shan, et al. Atomic-level characterization of the structural dynamics of proteins. *Science*, 330(6002):341–346, 2010.

[20] Hans Frauenfelder, Stephen G Sligar, and Peter G Wolynes. The energy landscapes and motions of proteins. *Science*, 254(5038):1598–1603, 1991.

[21] Krishna Neupane, Ajay P Manuel, and Michael T Woodside. Protein folding trajectories can be described quantitatively by one-dimensional diffusion over measured energy landscapes. *Nature Physics*, 12(7):700–703, 2016.

[22] Jordan M Horowitz, Kevin Zhou, and Jeremy L England. Minimum energetic cost to maintain a target nonequilibrium state. *Physical Review E*, 95(4):042102, 2017.

[23] H Howard K Schachman. Still looking for ivory tower. *Annual Review of Biochemistry*, 69:1 –69, 2000.

[24] Gregorio Weber. Ligand binding and internal equilibiums in proteins. *Biochemistry*, 11(5):864–878, 1972.

[25] Mingdong Dong, Sudhir Husale, and Ozgur Sahin. Determination of protein structural flexibility by microsecond force spectroscopy. *Nature nanotechnology*, 4(8):514–517, 2009.

[26] Giuseppe Zaccai. How soft is a protein? a protein dynamics force constant measured by neutron scattering. *Science*, 288(5471):1604–1607, 2000.

[27] Robert Zwanzig. Diffusion in a rough potential. *Proceedings of the National Academy of Sciences*, 85(7):2029–2030, 1988.

CHAPTER

FIVE

SIMULATIONS

5.1 Introduction

In the previous chapters, the entire analysis and modelling assumed linear response of the system. The linear response theory assumes that for low driving amplitudes the response of the system can be approximated by its equilibrium response function. For a protein that is modelled as a kelvin-voigt element, the maximum information one can extract from this is the stiffness and the friction co-efficient. Furthermore, the response function of the system becomes independent of the driving amplitude when assuming linear viscoelasticity. Therefore, changes in properties of the system due to increasing amplitude cannot be explained in the framework of linear response theory.

In this chapter we will be briefly discussing the framework we are currently developing to interpret the experimental results in terms of the intrinsic rates and energy landscape parameters. The model is inspired form the recent work by Degunther et. al. [1], where they have they have identified the phase sift in periodically driven non equilibrium systems and also come up with its bound. The dynamics modelled as a continous time markov jump process, will help us gain insight into the microscopic origin of viscoelasticity observed in the experiments.

5.2 Two State Model

We start with the simplest of the underlying energy profiles, with a stable state and a metastable state having E_0 and E_1 energies located at x_0 and x_1 respectively as shown in figure 5.1. The two minimas are separated by a barrier of energy B located at the position x_b. The distance between the two minimas L is given by $x_1 - x_0$.

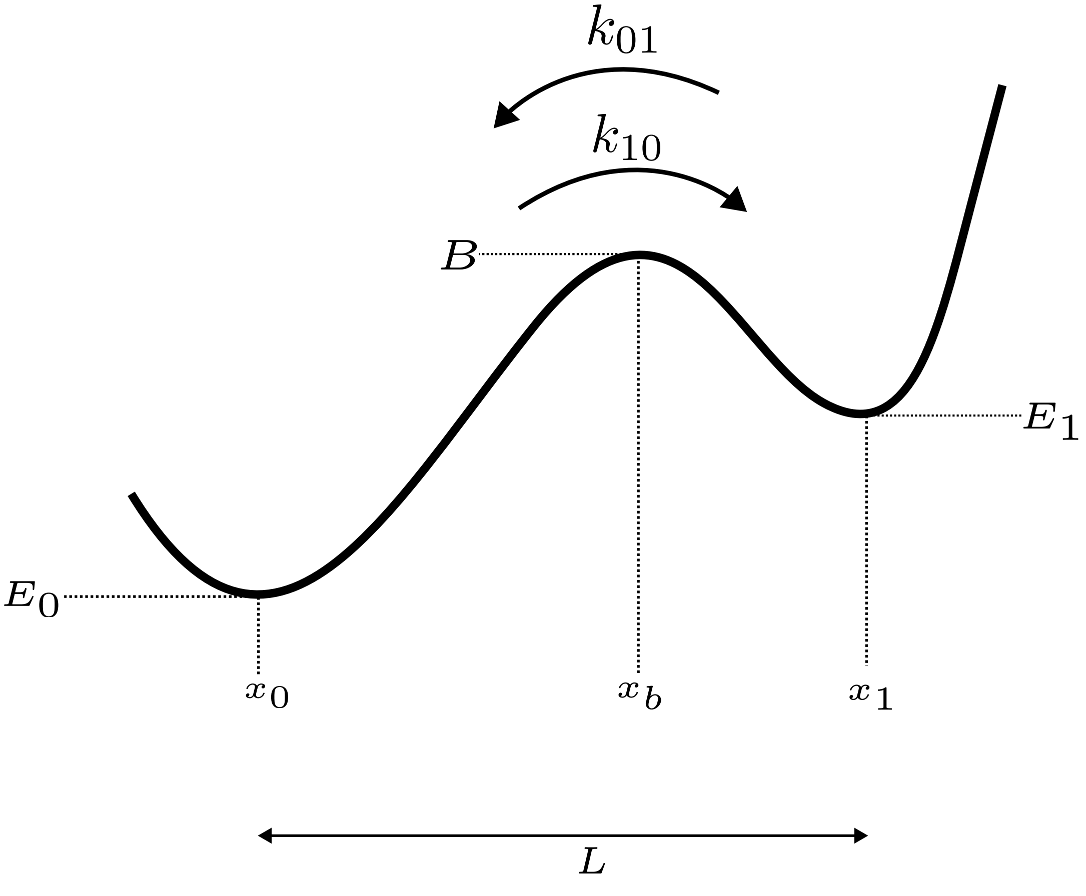

Figure 5.1: Schematic showing the energy profile

We now introduce a parameter α that is the ratio of the distance between the stable state and the barrier to the the distance between the two minimas.

$$\alpha = \frac{x_b - x_0}{x_1 - x_0} \tag{5.1}$$

$$= \frac{x_b - x_0}{L} \tag{5.2}$$

The distances can be expressed in terms of the parameter α as

$$x_b - x_0 = \alpha L \tag{5.3}$$

$$x_1 - x_b = (1-\alpha)L \tag{5.4}$$

This parameter can take values in the range $(0, 1)$ and depicts the where the barrier lies in the potential on the x-axis. For instance, $\alpha = 0.5$ indicates the barrier lies at the midpoint of the distance between the two minimas.

The drive or the control parameter that takes the system out of equilibrium is the location of the base of the cantilever. As mentioned earlier there are two parts it. Firstly, the quasistatic pulling part, that increases the separation between the base of the cantilever and the substrate given by λ_z. Secondly the oscillatory part that drives the base of the cantilever in an oscillatory manner, given by $\lambda_0 \sin \omega t$. The drive can then be wriiten as

$$\lambda(t) = \lambda_z + \lambda_0 \sin \omega t \tag{5.5}$$

The rates between the two states without the control parameter are given by

$$k_{10}(t) = k_0 \exp -\beta(B - E_0) \tag{5.6}$$

$$k_{01}(t) = k_0 \exp -\beta(B - E_1) \tag{5.7}$$

where k_{10} and k_{01} represent the rate going from the state 0 to state 1 and state 1 to state 0 respectively. The timescale of the jumps between the states is set by the prefactor k_0.

The control parameter when acting on the protein changes its energy landscape, due to it being time dependent the instantaneous rates can be written as

$$k_{10}(t) = k_0 \exp -\beta((B - \Delta B(t)) - (E_0 - \Delta E_0(t)) \tag{5.8}$$

$$k_{01}(t) = k_0 \exp -\beta((B - \Delta B(t)) - (E_1 - \Delta E_1(t)) \tag{5.9}$$

The oscillatory nature of the drive results in modulation of the energy of the minimas and the barriers. The protein is tethered to the cantilever with the help of a linker, with the linker being a non-linear spring. The force on the protein can be calculated by integrating the combined stiffness of the cantilever and linker with respect to the position of the base. This force multiplied by the location of the state gives us the change in its energy, which are expressed as

$$\Delta B(t) = x_b \int_0^{\lambda_z+\lambda\sin\omega t} k_{eff}(u)du \tag{5.10}$$

$$\Delta E_1(t) = x_1 \int_0^{\lambda_z+\lambda\sin\omega t} k_{eff}(u)du \tag{5.11}$$

$$\Delta E_0(t) = x_0 \int_0^{\lambda_z+\lambda\sin\omega t} k_{eff}(u)du \tag{5.12}$$

where k_{eff} is the combined stiffness of the cantilever and the tether.

The individual rates can be broken down in the following way.

$$k_{10}(t) = \Big[k_0 \exp -\beta(B - E_0)\Big] \exp \beta(\Delta B(t) - \Delta E_0(t)) \tag{5.13}$$

$$k_{01}(t) = \Big[k_0 \exp -\beta(B - E_1)\Big] \exp \beta(\Delta B(t) - \Delta E_1(t)) \tag{5.14}$$

The terms in the square brackets represents the rates in absence of the control parameter, ie, their equilibrium value.

Using equations 10, 11 and 12 to substitute the values of the changes in energy, the rate equations can be written as

$$k_{10}(t) = \Big[k_0 \exp -\beta(B - E_0)\Big] \exp \beta(\alpha L \int_0^{\lambda_z+\lambda\sin\omega t} k_{eff}(u)du) \tag{5.15}$$

$$k_{01}(t) = \Big[k_0 \exp -\beta(B - E_1)\Big] \exp \beta(-(1-\alpha) L \int_0^{\lambda_z+\lambda\sin\omega t} k_{eff}(u)du) \tag{5.16}$$

Finally, instantaneous values of the time dependent rates can be expressed as

$$k_{10}(t) = k_{10}^0 \exp \beta(\alpha L \int_0^{\lambda_z+\lambda\sin\omega t} k_{eff}(u)du) \tag{5.17}$$

$$k_{01}(t) = k_{01}^0 \exp \beta(-(1-\alpha) L \int_0^{\lambda_z+\lambda\sin\omega t} k_{eff}(u)du) \tag{5.18}$$

Where k_{01} and k_{10} are the equilibrium rates and are given by

$$k_{10} = k_0 \exp -\beta(B - E_0) \tag{5.19}$$

$$k_{01} = k_0 \exp -\beta(B - E_1) \tag{5.20}$$

Furthermore, the instantaneous rates follow local detailed balance

$$\frac{k_{10}(t)}{k_{01}(t)} = \exp -\beta(E_1(t) - E_0(t)) \tag{5.21}$$

The equation 5.17 and 5.18 give us the time-dependent rates. To proceed further, one way is to find the find the probability evolution of the system using the master equation . However, solution to the master equation with time dependent rates is hardly possible even with simple rate equation. In our case the forcing is highly nonlinear, due to which the probability evolution of the states cannot be found analytically.

There are four parameters in the model, α depicting asymmetry in the potential along x axis, the distance between the two states L and the equilibrium rates k^0_{01} and k^0_{10}. One could simulate the system with a Dynamic Monte-Carlo algorithm with the experimental parameters and see how the changes in the underlying energy landscape parameters change the resultant trajectories.

5.2.1 Dynamic Monte-Carlo Simulation

The Dynamic Monte-Carlo scheme is based on the method developed by Prados et. al. [2] for simulating master equations with time dependent rates. The steps followed to simulate the system are the following

Algorithm

1. The n number of proteins are initialised by choosing a state according to their equilibrium distribution. The equilibrium distribution of each protein is given by

$$P_i = \frac{k_{ij}}{k_{ij} + k_{ji}} \tag{5.22}$$

in our case there are just two states 0 and 1.

2. n random numbers are generated in the range (0,1). The n random numbers are used to calculate the transition time for the n proteins to make a transition from their occupied state. The transition time used to calculate for each protein can be

obtained by numerically solving the following integral equation for τ.

$$-ln(x) = \int_{t_0}^{t_0+\tau} k_{ii}(t)dt \tag{5.23}$$

where x is the random number, t_0 is the simulation time starting from zero for the first iteration, τ is the transition time, k_{ii} is the rate of going out from the occupied state for the protein.

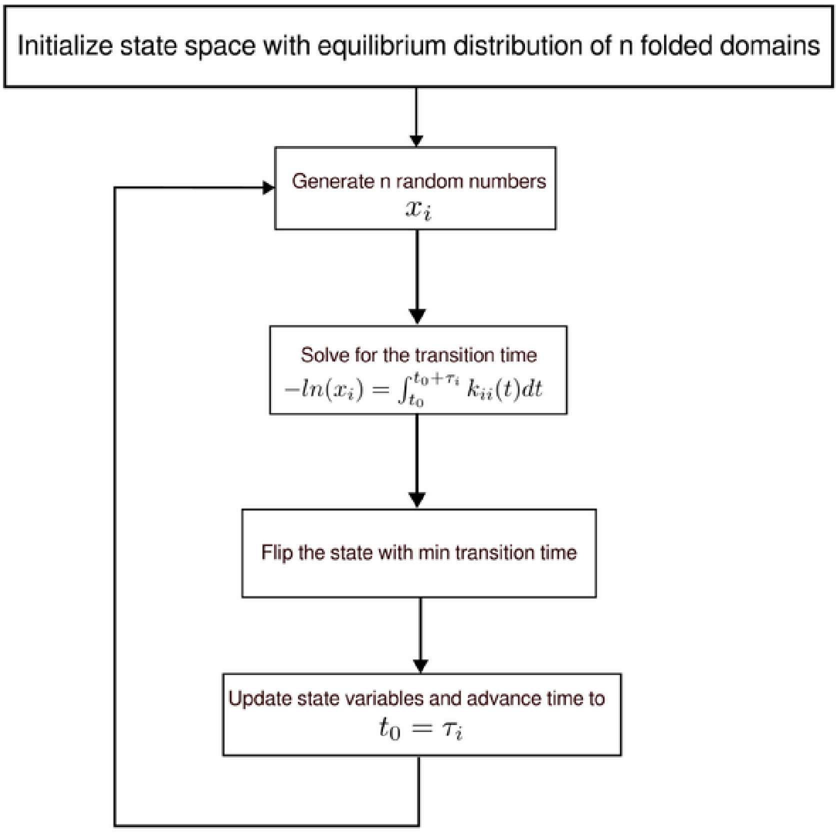
Initialize state space with equilibrium distribution of n folded domains
Generate n random numbers x_i
Solve for the transition time $-ln(x_i) = \int_{t_0}^{t_0+\tau_i} k_{ii}(t)dt$
Flip the state with min transition time
Update state variables and advance time to $t_0 = \tau_i$

Figure 5.2: Flowchart for the simulation algorithm

The instantaneous value for the numerical calculation is obtained from equation 5.17 or 5.18 depending on the state a protein occupies. The parameters k^0_{01}, k^0_{10}, L and α are initialised beforehand. Other parameters like k_{eff} are calculated from the cantilever stiffness and the experimentally obtained contour lengths.

3. The transition time τ obtained for each of the n proteins is compared and the one with the least transition time value is made to flip its state.

4. The state variables are updated and the simulation time t_0 is advanced by adding the transition time of the state flipped to its previous value.

5. The process is started over again from step 2 and continued until the simulation time t_0 reaches the desired value.

5.2.2 Preliminary Trajectories

Figure 5.3 shows trajectories generated with experimental parameters. The simulations are performed with parameters from the experiments. The drive frequency $\omega = 2000\ kHz$, amplitude $\lambda_0 = 1\ nm$, contour length for the linkers $L_c = 65\ nm$ and cantilever stiffness $k_c = 800\ pN/nm$. The energy landscape parameters taken are as $k_{10}^0 = k_{01}^0 = 500\ s^{-1}$, $L = 0.2\ nm$ and $\alpha = 0.25$ or $\alpha = 0.75$ for the two separate cases. For the simulation shown in the figure the system is pulled upto a length of $\lambda_z = 35\ nm$. The simulations are run for a period of 30 ms.

The bar plot shows the fraction of time the end to end distance of the polyprotein spends at a particular value. To make conclusive remarks on the trajectory, such simulations have to be repeated hundred of times to get proper statistics. In these trajectories for the driven cases the fraction of time spent at a particular length changes from its value when it is not driven. The type of behaviour seen here, is also dependent on the parameter α in the potential. With repeated simulations, one can obtain the evolution of the end to end distance probability distribution of the polyprotein. With this distribution, it opens up possibilities of quantifying the phase lag in the response with respect to the drive drive signal and also how far it is from equilibrium due to the drive. The complexity in the analysis is due to the fact that the rate variation of each state is dependent on the linker elasticity which changes every time a domain makes a transition.

Further analysis and simulations are to be performed for different number of folded domains n, rates k_{01}^0 and k_{01}^0, and the pulled distance λ_z.

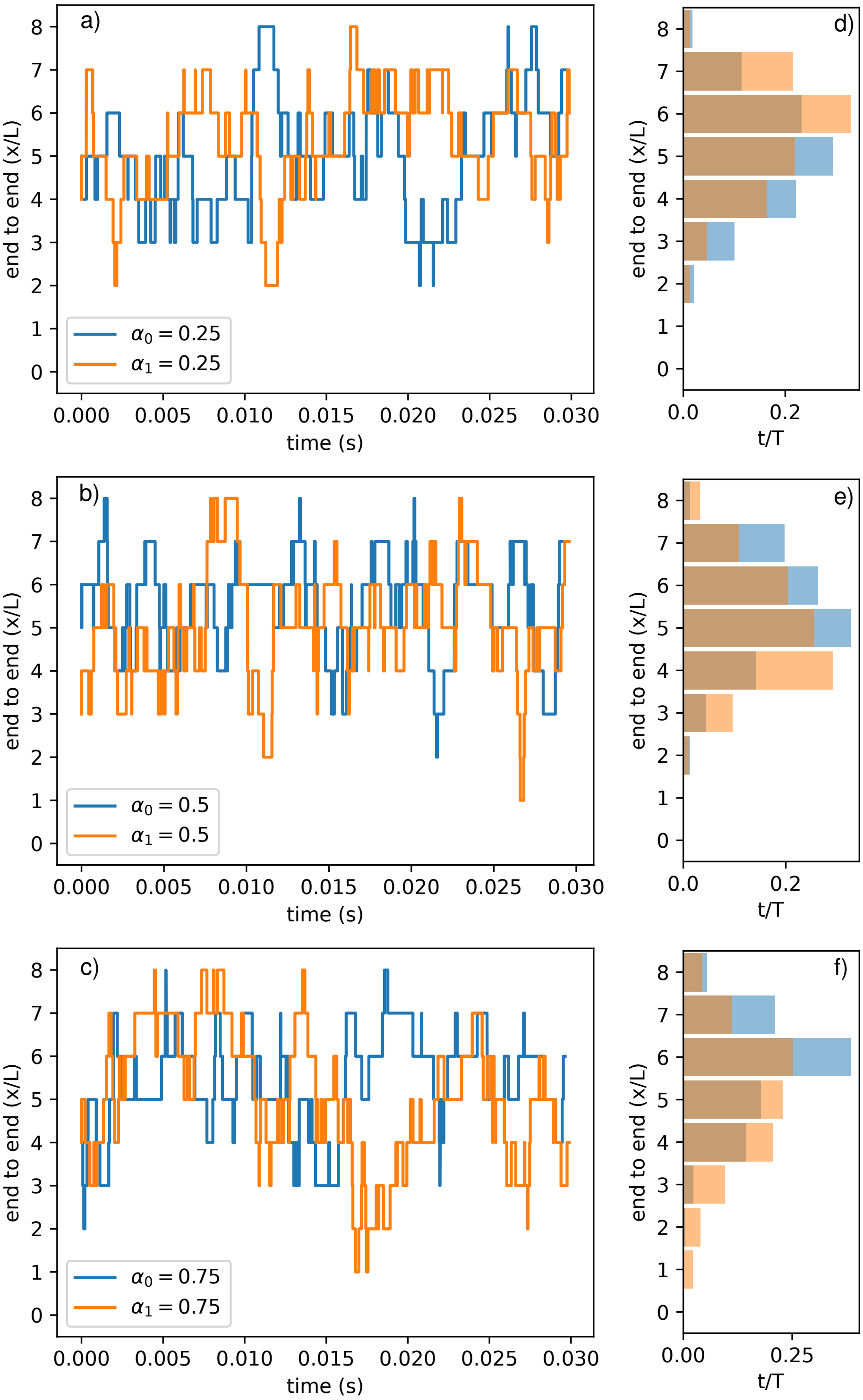

Figure 5.3: a),b) and c) depict the trajectories obtain for parameters discussed in the text. $_0$ and α_1 represent the asymmetry parameter and subscript represent the 0 and 1 nm driving amplitude respectively. d) e) and f) are the bar plot showing fraction of time the end to end distance of the polyprotein spends at a particular length during the simulation.

Bibliography

[1] Julius Degünther, Timur Koyuk, and Udo Seifert. Phase shift in periodically driven non-equilibrium systems: its identification and a bound. *Journal of Statistical Mechanics: Theory and Experiment*, 2022(3):033207, 2022.

[2] A Prados, JJ Brey, and B Sánchez-Rey. A dynamical monte carlo algorithm for master equations with time-dependent transition rates. *Journal of statistical physics*, 89(3):709–734, 1997.

CHAPTER

SIX

CONCLUSION & FUTURE DIRECTIONS

The debate around measuring friction coefficient of single polymer chains using AFM is almost about 2 decades old. After realizing the potential of AFM technique to measure the force required to rupture single bonds and unfold single domains of proteins, it was also put to use to measure the internal friction of single molecules [1–4]. These experiments in the early years reported friction coefficients of unfolded chain to be of the order $\sim 10^{-6} kg/s$. It yielded diffusion coefficient, which were five orders of magnitude smaller than those obtained with optical techniques, such as FRET. Berkovich et al. [5] provided an explanation for this discrepancy by arguing that the cantilever or the probe to which, the molecule is tethered, relaxes much slower than the molecule itself. Hence, the diffusion coefficient is largely determined by the probe relaxation, which in turn depends on its size. Stiff cantilevers (with higher Q) relax much faster, however they can not be used in static force clamp measurements similar to the one performed by Berkovich et al. due to their reduced sensitivity to force. The interferometer based AFM has revealed that the friction coefficient of unfolded chain is immeasurably low[6] and that of folded domains can now be measured in a quantitative manner[7].

The successful measurement of viscoelasticity of single molecules has implications for many topics in biophysics. We discuss few of them in this section. Some proteins are known to exhibit functional heterogeneity[8, 9]. This means that there are host of conformations capable of delivering distinct functions. One of the least understood aspects of this functional heterogeniety is the inter-conversion rates between these states[10]. The dynamics of interconversion, particularly, the time scale is crucial for understanding protein function. Using interferometer-based dynamic AFM, one is able to measure phase lags and thereby energy lost in each cycle, as the protein is periodically driven over its many states. It is possible to do these measurements over a range of frequencies. This opens up the possibility of extracting slow interconversion rates between sub-states.

Another direct impact of successful characterization of viscoelastic properties of single proteins is on deciphering the function of mechanosensitive proteins, such as immunoglobulins of titin, talins, spectrins and cadherins. Often, the tension in the folded state is responsible for transmission of force. For instance, inside the inner ear, opening of ion channel to produce action potential as a response to sound waves, involves modulation of tension in a cadherin complex called tip-link[11]. Mapping of viscoelasticity parameters of protein domains modelled as soft solids will provide insight into which site specific mutations are responsible for diseases. In this sense, dynamic AFM serves as a tool to identify the actual alteration in mechanical properties, such as its elasticity and viscosity, due to mutation.

Molecular bonds, such as those between ligand and receptors, are of the most intriguing kind. Sometimes they exhibit counter-intuitive properties such as becoming stronger under force. Catch bonds play a central role in most biological adhesive interactions that has to survive tensile force on it[12]. Dynamic AFM offers a crucial advantage of mapping the bond's viscoelastic response and comparing it with slip bonds. Direct and simultaneous mapping of viscous and elastic component may provide insight into unraveling physics of catch-bonds.

The ability to pick up and manipulate single molecules and measure the rupturing force distributions under varying loading rates is utilized in providing experimental confirmations of many theoretical ideas in non-equilibrium statistical physics. For instance, a time-dependent periodic driving of fluctuating non equilibrium system produces a phase lag between the response and drive [13, 14]. The dynamic AFM has now been successful for the first time in providing direct and artefact-free measurements of such a phase lag. Further, by controlling the speed of forcing this lag can be reduced or enhanced. The phase lag observed in case of I-27 immunoglobulins of titin, thus not only gives internal friction coefficient using the the framework of linear response theory, but also can be used to verify some claims in theoretical work carried out so far in this field.

BIBLIOGRAPHY

[1] Masaru Kawakami, Katherine Byrne, David J Brockwell, Sheena E Radford, and D Alastair Smith. Viscoelastic study of the mechanical unfolding of a protein by afm. *Biophysical journal*, 91(2):L16–L18, 2006.

[2] Harald Janovjak, Daniel J Müller, and Andrew DL Humphris. Molecular force modulation spectroscopy revealing the dynamic response of single bacteriorhodopsins. *Biophysical journal*, 88(2):1423–1431, 2005.

[3] Bhavin S Khatri, Katherine Byrne, Masaru Kawakami, David J Brockwell, D Alastair Smith, Sheena E Radford, and Tom CB McLeish. Internal friction of single polypeptide chains at high stretch. *Faraday discussions*, 139:35–51, 2008.

[4] Yukinori Taniguchi, Bhavin S Khatri, David J Brockwell, Emanuele Paci, and Masaru Kawakami. Dynamics of the coiled-coil unfolding transition of myosin rod probed by dissipation force spectrum. *Biophysical journal*, 99(1):257–262, 2010.

[5] Ronen Berkovich, Rodolfo I Hermans, Ionel Popa, Guillaume Stirnemann, Sergi Garcia-Manyes, Bruce J Berne, and Julio M Fernandez. Rate limit of protein elastic response is tether dependent. *Proceedings of the National Academy of Sciences*, 109(36):14416–14421, 2012.

[6] Shatruhan Singh Rajput, Surya Pratap S Deopa, Jyoti Yadav, Vikhyaat Ahlawat, Saurabh Talele, and Shivprasad Patil. The nano-scale viscoelasticity using atomic force microscopy in liquid environment. *Nanotechnology*, 32(8):085103, 2020.

[7] Surya Pratap S Deopa, Shatruhan Singh Rajput, Aadarsh Kumar, and Shivprasad Patil. Direct and simultaneous measurement of the stiffness and internal friction of a single folded protein. *The Journal of Physical Chemistry Letters*, 13(40):9473–9479, 2022.

[8] H Peter Lu, Luying Xun, and X Sunney Xie. Single-molecule enzymatic dynamics. *Science*, 282(5395):1877–1882, 1998.

[9] Brian P English, Wei Min, Antoine M Van Oijen, Kang Taek Lee, Guobin Luo, Hongye Sun, Binny J Cherayil, SC Kou, and X Sunney Xie. Ever-fluctuating single enzyme molecules: Michaelis-menten equation revisited. *Nature chemical biology*, 2(2):87–94, 2006.

[10] Michael Hinczewski, Changbong Hyeon, and Devarajan Thirumalai. Directly measuring single-molecule heterogeneity using force spectroscopy. *Proceedings of the National Academy of Sciences*, 113(27):E3852–E3861, 2016.

[11] Surbhi Garg, Amin Sagar, Gayathri S Singaraju, Rahul Dani, Naimat K Bari, Athi N Naganathan, and Sabyasachi Rakshit. Weakening of interaction networks with aging in tip-link protein induces hearing loss. *Biochemical Journal*, 478(1):121–134, 2021.

[12] Sabyasachi Rakshit, Yunxiang Zhang, Kristine Manibog, Omer Shafraz, and Sanjeevi Sivasankar. Ideal, catch, and slip bonds in cadherin adhesion. *Proceedings of the National Academy of Sciences*, 109(46):18815–18820, 2012.

[13] Julius Degünther, Timur Koyuk, and Udo Seifert. Phase shift in periodically driven non-equilibrium systems: its identification and a bound. *Journal of Statistical Mechanics: Theory and Experiment*, 2022(3):033207, 2022.

[14] Suriyanarayanan Vaikuntanathan and Christopher Jarzynski. Dissipation and lag in irreversible processes. *EPL (Europhysics Letters)*, 87(6):60005, 2009.

LIST OF PUBLICATIONS

Deopa, S. P. S., & Patil, S. Dynamic atomic force microscope for viscoelasticity of single folded proteins. (in preparation)

Deopa, S. P. S., Rajput, S. S., Kumar, A., & Patil, S. (2022). Direct and Simultaneous Measurement of the Stiffness and Internal Friction of a Single Folded Protein. The Journal of Physical Chemistry Letters, 13(40), 9473-9479.

Ahlawat, V., **Deopa, S. P. S.**, & Patil, S. (2022). Quantitative Elasticity of Flexible Polymer Chains Using Interferometer-Based AFM. Nanomaterials, 12(3), 526.

Rajput, S. S., **Deopa, S. P. S.**, Ajith, V. J., Kamerkar, S. C., & Patil, S. (2021). Validity of point-mass model in off-resonance dynamic atomic force microscopy. Nanotechnology, 32(40), 405702.

Rajput, S. S., **Deopa, S. P. S.**, Yadav, J., Ahlawat, V., Talele, S., & Patil, S. (2020). The nano-scale viscoelasticity using atomic force microscopy in liquid environment. Nanotechnology, 32(8), 085103.